Functionalizing the Defects: Postsynthetic Ligand Exchange in the Metal Organic Framework UiO-66

Supporting Information

Functionalizing the Defects: Post Synthetic Ligand Exchange in Metal Organic Framework UiO-66

Greig C. Shearer,† Jenny G. Vitillo,‡ Silvia Bordiga,‡ Stian Svelle,† Unni Olsbye,† Karl Petter Lillerud*,†

† *inGAP Centre for Research Based Innovation, Department of Chemistry, University of Oslo, P.O. Box 1033, N-0315 Oslo, Norway*

‡ *Department of Chemistry NIS & ISTM Reference Centre, University of Torino, Via Quarello 15, 10135 Turin, Italy*

Table of Contents

1. Synthesis Details

Table of Contents

1.1. 50Benz

50Benz was synthesized by a slightly modified version of the method previously outlined by Cohen and coworkers.[1] Briefly, 1.68 g $ZrCl_4$ (7.21 mmol), 0.17 mL H_2O (9.44 mmol), 44.03 g Benzoic Acid (360.5 mmol) and 1.20 g 1,4-benzenedicarboxylic acid (H_2BDC, 7.22 mmol) were sequentially added to a 1 L Erlenmeyer flask containing 413 mL of N,N'-dimethyl formamide (DMF, 5330 mmol). In order to ensure the complete dissolution of reagents, mild heating (ca. 70 °C) and stirring was applied to the synthesis mixture for the duration of its preparation. Once all reagents had dissolved, the magnet was removed and a watch glass was placed on the mouth of the flask as a loose cover. The synthesis mixture was then placed in an oven (preheated to 120 °C) where it remained for 24 hours.

The resulting microcrystalline powder precipitate was separated from the synthesis solution (via centrifugation) and washed by shaking it overnight in 80 mL of fresh DMF. Three further separation/washing cycles were performed the next day, albeit for a shorter duration (*ca*. 2 hours per wash) before the washed product (total 4 x 80 mL DMF) was separated from the solvent by centrifugation, dried overnight in an oven set to 60 °C, and ground with a mortar and pestle.

Most of the resulting "As Synth" material was used as a precursor to 50Benz-HA (see the following subsection), while the majority of the remaining sample was subjected to a further "activation" procedure to remove DMF guest molecules from its pores. This was achieved by placing the sample in a porcelain crucible and heating it at 200 °C for 24 hours in a conventional oven, a treatment which does not affect the crystallinity of the sample (see **Figure S39** in the appendix). The activated sample is not completely empty as it adsorbs atmospheric water vapor when cooled to room temperature. All characterization results were obtained on this "activated" material, except for a few explicitly stated exceptions (e.g. EDX results, see **Section 4.2.5**).

1.2. 50Benz-HA

50Benz-HA was synthesized by a post synthetic method analogous to that employed to remove benzoic acid from NU-1000,[2] albeit at a much larger scale. Specifically, 1.85 g 50Benz (As Synth, not activated), 555 mL DMF, and 23.1 mL 8M HCl were sequentially added to a 1L Erlenmeyer flask such that the MOF : DMF : 8M HCl ratio in the mixture was 2 g : 600 mL : 25 mL. This ratio can be used to scale the procedure up or down accordingly. The mixture was thoroughly stirred before the mouth of the flask was loosely covered with a watch glass. The flask and its contents were then heated at 100 °C for 24 hours in a preheated oven. The resulting microcrystalline powder was separated from the mixture (via centrifugation) and washed by shaking overnight in 80 mL of fresh DMF. Three further separation/washing cycles were performed the next day, albeit for a shorter duration (*ca*. 2 hours per wash) before the washed product (total 4 x 80 mL DMF) was separated from the solvent by centrifugation, dried overnight in an oven set to 60 °C, and ground with a mortar and pestle.

A small amount of the resulting "As Synth" material was set aside for characterization, while the majority was subjected to a further "activation" procedure to remove DMF guest molecules from the pores. This was achieved by placing the sample in a porcelain crucible and heating it at 200 °C for 24 hours in a conventional oven, a treatment which does not affect the crystallinity of the sample (see **Figure S39** in the appendix). The activated sample is not completely empty as it adsorbs atmospheric water vapor when cooled to room temperature. All characterization results were obtained on this "activated" material, except for a few explicitly stated exceptions (e.g. EDX results, see **Section 4.2.5**).

1.3. UiO-66-Ideal

UiO-66-Ideal was synthesized via an optimized version[3] of a procedure which was originally outlined by Serre and coworkers and later promoted by us.[4, 5]

The synthesis mixture was prepared by sequentially adding 3.781 g $ZrCl_4$ (16.22 mmol), 2.865 ml 35 % HCl (32.45 mmol), and 5.391 g H_2BDC (32.45 mmol) to a 250 ml conical flask containing 97.40 ml of N,N'-dimethyl formamide (1258 mmol). In order to ensure the complete dissolution of reagents, mild heating (*ca*. 70 °C) and stirring was applied to the synthesis mixture for the duration of its preparation.

Once all the reagents had dissolved, the stirring magnet was removed from the flask and the synthesis mixture was transferred to a 200 mL Teflon liner. The liner was then sealed in a stainless steel autoclave which was subsequently placed in an oven preheated to 220 °C. After 24 hours at this temperature, the autoclave was rapidly cooled over a period of about 30 minutes by dropping it into a bucket of cold tap water. The liner was then removed from the autoclave, and its solid contents were recovered from the solution by centrifugation.

The solid was then washed by shaking overnight in 80 mL of fresh DMF. Three further separation/washing cycles were performed the next day, albeit for a shorter duration (*ca*. 2 hours per wash) before the washed product (total 4 x 80 mL DMF) was separated from the solvent by centrifugation, dried overnight in an oven set to 60 °C, and ground with a mortar and pestle.

In order to remove volatile organics (e.g. DMF) from the resulting material, the entirety of the sample was transferred to a porcelain crucible and heated at 200 °C for 24 hours in a conventional oven. Non-volatile organics were then removed via calcination. This was achieved by use of a 2 step heating program on a multi-step muffle furnace. In the first step, a 5 °C min^{-1} ramp was used to heat the sample from room temperature to 200 °C, where it was held for 10 minutes. The second step involved a 0.5 °C min^{-1} ramp to 270 °C, where it was held for 70 hours before being allowed to cool to room temperature naturally. The calcined sample is not completely empty as it adsorbs some atmospheric water vapor during cooling.

It should be noted that several temperatures were trialed for the calcination method. Although the material would always retain its crystallinity, the sample would often become discolored (yellow/light brown) when a temperature above 270 °C was employed. The origin of this discoloration is unknown.

1.4. Small Scale L-Serine PSE Reactions

In each experiment, 84 mg of UiO-66 (either 50Benz (activated), 50Benz-HA (activated), or UiO-66-Ideal (calcined), depending on the specific experiment) was placed in a 15 mL polypropylene centrifuge tube. A 1 mL portion of the relevant aqueous L-Serine solution (0.0, 0.5, 1.0, 1.5, 2.0, 2.5, or 3.0 M) was then added to the tube. Prior to their addition, all solutions were adjusted to pH = 7 with 1.0 M HCl and NaOH as required. The tubes were then capped and their contents thoroughly mixed via shaking and ultrasonic agitation. Finally, the reaction mixtures were heated at 85 °C for 16 hours in a preheated oven. One reaction (between 50Benz-HA and the 3.0M L-Serine solution) was performed in exactly the same way, albeit at room temperature.

After reaction, the mixtures were separated by centrifugation and:

1) The solution was decanted.
2) The solid products were washed with distilled H_2O (5 x 10 mL), acetone (5 x 10 mL), and dichloromethane (6 x 10 mL, the last of which overnight). Each wash involved shaking and ultrasonic agitation.
3) The samples were dried in a desiccator at room temperature and ground with a mortar and pestle.

In one experiment (on 50Benz-HA), two cycles of PSE (each with 3.0 M L-Serine) were performed. In said experiment, a second 1 mL portion of aqueous L-Serine solution was added to the centrifuge tube after performing the first reaction and step 1) outlined above. The tube was then capped and its contents were thoroughly mixed via shaking and ultrasonic agitation. After mixing, the reaction mixture was returned to the oven where it was again heated at 85 °C for 16 hours. Finally, the product was obtained by performing steps 1) through 3) outlined above.

Important notes: The washing and drying procedure was found to be critical in preventing the loss of crystallinity or the formation of organic impurities in the product, specifically when the reaction involved 50Benz-HA:

When the PSE product was dried directly after water washing, the crystallinity of the resulting material was found to be significantly diminished. This problem was avoided when water was exchanged with another solvent (here acetone) prior to drying.

The very same phenomenon has been previously observed and discussed in work by Farha and co-workers, who concluded that capillary forces are the reason some Zr_6 MOFs collapse when dried directly after being subjected to treatment in water.[6] Due to its high surface tension, these forces are particularly strong in water. Exchanging water for a solvent of lower surface tension (e.g. acetone) significantly reduces capillary forces, allowing the MOF to be safely dried.

This behavior has never been previously observed for UiO-66, which is usually completely stable to such water treatment. This it likely because its smaller pores do not allow as many water molecules to accumulate, lessening the capillary forces that the material experiences upon drying. However, 50Benz-HA is much more porous than is typical for a UiO-66 sample, explaining its sensitivity to capillary force driven collapse. Interestingly, the sample was also found to decompose when exposed to air for long periods of time (on the order of months). This was easily avoided by storing the material in a desiccator, suggesting that water sensitivity is to blame for this structural degradation.

As mentioned above, acetone exchange prevented the material from collapsing during drying. However, dried acetone exchanged samples were found to be contaminated with a significant amount of unidentified organic impurities (as evidenced by dissolution/^{1}H NMR spectroscopy). This problem was alleviated by performing a second solvent exchange with dichloromethane. Moreover, the low boiling point of dichloromethane (39.6 °C) allowed the samples to be emptied at lower temperatures, a point which came in useful for sorption measurements (see **Table S1** in **Section 2.7**).

1.5. Large Scale L-Serine PSE Reactions

1.5.1. Synthesis of 0M-, 1.5M-, and 3M-Ser

In all three syntheses, 420 mg of (activated) 50Benz-HA was placed in a 30 mL polypropylene centrifuge tube. The three syntheses differed by the concentration of the aqueous L-Serine solution which was added to the tube. Specifically, the synthesis of 0M-, 1.5M-, and 3M-Ser respectively involved the addition of a 5mL portion of a 0.0, 1.5, and 3.0 M aqueous L-Serine solution (all pre-adjusted to pH = 7 with 1 M HCl and NaOH as required). The tubes were then capped and their contents thoroughly mixed via shaking and ultrasonic agitation. Finally, the reaction mixtures were heated at 85 °C for 16 hours in a preheated oven.

After reaction, the mixtures were separated by centrifugation and:

1) The solution was decanted.
2) The solid products were washed with distilled H_2O (5 x 20 mL), acetone (5 x 20 mL), and dichloromethane (6 x 20 mL, the last of which overnight). Each wash involved shaking and ultrasonic agitation.
3) The samples were dried in a desiccator and room temperature and ground with a mortar and pestle.

Important notes: The washing and drying procedure was found to be critical in preventing the loss of crystallinity or the formation of organic impurities in the product, specifically when the reaction involved 50Benz-HA:

When the PSE product was dried directly after water washing, the crystallinity of the resulting material was found to be significantly diminished. This problem was avoided when water was exchanged with another solvent (here acetone) prior to drying.

The very same phenomenon has been previously observed and discussed in work by Farha and co-workers, who concluded that capillary forces are the reason some Zr_6 MOFs collapse when dried directly after being subjected to treatment in water.[6] Due to its high surface tension, these forces are particularly strong in water. Exchanging water for a solvent of lower surface tension (e.g. acetone) significantly reduces capillary forces, allowing the MOF to be safely dried.

This behavior has never been previously observed for UiO-66, which is usually completely stable to such water treatment. This it likely because its smaller pores do not allow as many water molecules to accumulate, lessening the capillary forces that the material experiences upon drying. However, 50Benz-HA is much more porous than is typical for a UiO-66 sample, explaining its sensitivity to capillary force driven collapse. Interestingly, the sample was also found to decompose when exposed to air for long periods of time (on the order of months). This was easily avoided by storing the material in a desiccator, suggesting that water sensitivity is to blame for this structural degradation.

As mentioned above, acetone exchange prevented the material from collapsing during drying. However, dried acetone exchanged samples were found to be contaminated with a significant amount of unidentified organic impurities (as evidenced by dissolution/^{1}H NMR spectroscopy). This problem was alleviated by performing a second solvent exchange with dichloromethane. Moreover, the low boiling point of dichloromethane (39.6 °C) allowed the samples to be emptied at lower temperatures, a point which came in useful for sorption measurements (see **Table S1** in **Section 2.7**).

1.5.2. Synthesis of 3M-Ser-x2

Up until (but not including) step 2) outlined in the previous subsection, the synthesis of 3M-Ser-x2 was identical to that of 3M-Ser. However, in this case, a 5 mL portion of the 3.0 M L-Serine (pH = 7) solution was added to the tube after the completion of step 1). The tube was then capped and its contents were thoroughly mixed via shaking and ultrasonic agitation. The reaction mixture was then returned to the oven where it was again heated at 85 °C for 16 hours. The final product was then obtained by application of steps 1) through 3).

Important notes: The washing and drying procedure was found to be critical in preventing the loss of crystallinity or the formation of organic impurities in the product, specifically when the reaction involved 50Benz-HA:

When the PSE product was dried directly after water washing, the crystallinity of the resulting material was found to be significantly diminished. This problem was avoided when water was exchanged with another solvent (here acetone) prior to drying.

The very same phenomenon has been previously observed and discussed in work by Farha and co-workers, who concluded that capillary forces are the reason some Zr_6 MOFs collapse when dried directly after being subjected to treatment in water.[6] Due to its high surface tension, these forces are particularly strong in water. Exchanging water for a solvent of lower surface tension (e.g. acetone) significantly reduces capillary forces, allowing the MOF to be safely dried.

This behavior has never been previously observed for UiO-66, which is usually completely stable to such water treatment. This it likely because its smaller pores do not allow as many water molecules to accumulate, lessening the capillary forces that the material experiences upon drying. However, 50Benz-HA is much more porous than is typical for a UiO-66 sample, explaining its sensitivity to capillary force driven collapse. Interestingly, the sample was also found to decompose when exposed to air for long periods of time (on the order of months). This was easily avoided by storing the material in a desiccator, suggesting that water sensitivity is to blame for this structural degradation.

As mentioned above, acetone exchange prevented the material from collapsing during drying. However, dried acetone exchanged samples were found to be contaminated with a significant amount of unidentified organic impurities (as evidenced by dissolution/^{1}H NMR spectroscopy). This problem was alleviated by performing a second solvent exchange with dichloromethane. Moreover, the low boiling point of dichloromethane (39.6 °C) allowed the samples to be emptied at lower temperatures, a point which came in useful for sorption measurements (see **Table S1** in **Section 2.7**).

2. Experimental Methods

Table of Contents

2.1. Powder X-Ray Diffraction (PXRD)

Samples were prepared by dispersing 30 mg of sample on a flat, glass plate PXRD sample holder with a diameter of 2.5 cm. A stretched piece of plastic film was then used to spread, flatten and hold the sample in position for measurement. The plastic film is evident in the PXRD patterns, appearing as two broad peaks covering 2θ ranges of *ca*. 20-22° and 23-24°.

The PXRD patterns were collected on a Bruker D8 Discovery diffractometer equipped with a focusing Ge-monochromator, using Cu-K_α radiation (λ = 1.5418 Å) and a Bruker LYNXEYE detector. Patterns were collected in reflectance Bragg-Brentano geometry over a 2θ range of 2-50°.

2.2. Dissolution / ^{1}H NMR Spectroscopy

Samples were prepared by weighing 20 mg of the MOF sample of interest into an NMR tube and adding 600 uL of 1M NaOH (in D_2O). The NMR tube was then capped and the contents were mixed by inverting the tube 2-3 times. The MOF was then left to digest over a period of 24 hours before measurement (see next paragraph for details). This hydroxide based procedure dissolves only the organic portion of the MOF (linker, modulator, solvent etc.), while the inorganic content is converted into ZrO_2 which sinks to the bottom of the NMR tube and does not influence the spectra.

Liquid ^{1}H NMR spectra were obtained with a Bruker Avance DPX-300 NMR Spectrometer (300 MHz). The relaxation delay (d1) was set to 20 seconds to improve the reliability of integration. This allowed us to accurately determine the molar ratios between the organic components. The number of scans was 64.

2.3. TGA-DSC

TGA-DSC measurements were made with a Stanton Redcroft TGA-DSC. MOF samples (*ca*. 30 mg) were added to platinum crucibles before measurement. Each TGA-DSC run was made by heating the samples to 900 °C at a rate of 5 °C min^{-1} under a simultaneous feed of N_2 (20 mL/min) and O_2 (5 mL/min).

2.4. Attenuated Total Reflection Infrared (ATR-IR) Spectroscopy

ATR-IR spectroscopy was performed with a Bruker Vertex70 FTIR spectrometer equipped a Bruker OPTIK Platinum ATR accessory with a diamond internal reflection element. The MOF samples were introduced to the instrument as loose powders and their ATR-IR spectra (detected with an MCT detector) were obtained at 2 cm^{-1} resolution over a wavenumber range of 4000-600 cm^{-1}. The number of scans was 256. The spectral intensity was corrected for the change in the effective thickness value as a function of the incident wavelength.

2.5. Scanning Electron Microscopy (SEM)

Scanning Electron Microscope (SEM) Images were taken on a Hitachi SU8230 Field Emission Scanning Electron Microscope (FE-SEM). The acceleration voltage was set to 2.5 kV. In order to reduce sample charging, a 1.5 kV deceleration voltage was applied, resulting in a "landing voltage" of 2.5 – 1.5 = 1 kV.

2.6. Elemental Analysis (via EDX)

Elemental analysis was performed on a Hitachi SU8230 Field Emission Scanning Electron Microscope (FE-SEM) equipped with an Energy Dispersive X-ray Spectrometer. Samples were prepared by spreading them on carbon tape. Spectra were acquired with the "precise" setting at a working distance of 15 mm and a magnification of 1000x. The accelerating voltage was set to 7 kV so that both zirconium (L_α = 2.042) and chlorine (K_α = 2.621 keV) could be reliably quantified.

2.7. Nitrogen Sorption Measurements at 77 K

Nitrogen sorption measurements at 77 K were performed with a BelSorp mini II instrument. In each measurement, approximately 50 mg of MOF sample was weighed into a 9.001 cm^3 glass cell, in which the guest molecules were removed by "activation" (i.e. simultaneous vacuum and heat treatment, see **Table S1** below for specific conditions). The sample cells were then immersed in a dewar of liquid nitrogen, where they remained for the duration of the adsorption measurement.

BET surface areas were extracted from the nitrogen adsorption isotherms via the method described in **Section 3.2**.

Table S1. Activation conditions used in this work. Vacuum was applied throughout each procedure. All samples completely survived their respective treatments, as shown by PXRD measurements made after nitrogen sorption (see **Figure S39** and **Figure S40** in the appendix).

Sample	Activation Procedure
50Benz *	1 hour at 80 °C, 2 hours at 200°C
50Benz-HA *	1 hour at 80 °C, 2 hours at 200°C
0M-Ser †	1 hour at RT, 3 hours at 100 °C
1.5M-Ser †	1 hour at RT, 3 hours at 100 °C
3M-Ser †	1 hour at RT, 3 hours at 100 °C
3M-Ser-x2 †	1 hour at RT, 3 hours at 100 °C

* DMF was already removed via an external activation at 200 °C (see synthesis details). The second activation above removes the water molecules which were subsequently adsorbed from the atmosphere.

† These samples were filled with dichloromethane (used during the washing procedure, see **Section 1.5**) and could thus be activated under milder conditions (B.P. of DCM = 39.6 °C), as proven by dissolution/^{1}H NMR measurements (see **Figure S41** to **Figure S44** in the appendix).

2.8. Simulated Nitrogen Adsorption Isotherms

Adsorption isotherms were simulated with the "adsorption isotherm" task within the "Sorption Tools" menu in Accelrys Materials Studio version 8.1. The simulations were performed at 77 K, using a geometry optimized N_2 molecule as the adsorptive and a single, geometry optimized unit cell of the model structure of interest as the adsorbent. We adopted the Metropolis method and the COMPASS force field. The isotherms were simulated over a pressure range of 0.01-100 kPa, in which 50 fugacity steps were distributed logarithmically in order to increase the number of data points in the steep initial portion of the isotherm. The "Fine" quality setting (involving 100,000 equilibration steps and 1,000,000 production steps) was used for all simulations. Charges were force field assigned, while electrostatic forces were calculated with the Ewald method. The "atom based" method was adopted for the calculation of Van der Waals forces. No constraints were assigned. Due to the statistical nature of the calculations, one will always observe (very) small differences between the results when simulations are repeated.

In order to compare the simulated isotherms with those experimentally obtained, the y-scale units of the raw simulated isotherms were converted from "$\boldsymbol{N_2\ Molecules\ Per\ Unit\ Cell}$" to "$\boldsymbol{V_a\ \left(cm^3(STP)g^{-1}\right)}$", the volume of standard state nitrogen adsorbed per gram of material:

$$\boldsymbol{V_a\ \left(cm^3(STP)g^{-1}\right)} = \frac{\boldsymbol{N_2\ Molecules\ Per\ Unit\ Cell}}{\boldsymbol{M_{Unit\ Cell}}} * \frac{\boldsymbol{RT}}{\boldsymbol{N_aP}} \qquad (1)$$

Where:

$\boldsymbol{M_{Unit\ Cell}}$ is the molar mass ($g \cdot mol^{-1}$) of the contents of the unit cell from which the isotherm was simulated,

$\boldsymbol{R}$ is the gas constant (= 8314.46 $cm^3 \cdot kPa \cdot K^{-1} \cdot mol^{-1}$),

$\boldsymbol{T}$ is the standard temperature (= 273.15 K),

$\boldsymbol{N_a}$ is Avogadro's number (= $6.022 \times 10^{23}\ mol^{-1}$).

$\boldsymbol{P}$ is the standard pressure (= 100 kPa).

Likewise, the x-scale units of the raw simulated isotherms were converted from "$\boldsymbol{Total\ Fugacity\ (kPa)}$" to "$\boldsymbol{(p/p_0)}$", the relative pressure:

$$\boldsymbol{(p/p_0)} = \frac{\boldsymbol{Total\ Fugacity\ (kPa)}}{\boldsymbol{Atmospheric\ Pressure\ (= 101.325\ kPa)}} \qquad (2)$$

After making the above conversions, BET surface areas were extracted from the simulated nitrogen adsorption isotherms via the method described in **Section 3.2**.

2.9. CO_2 Sorption Measurements

CO_2 Sorption isotherms were obtained with a volumetric instrument (a Micromeritics ASAP 2020 sorption analyzer) over a pressure range of 0 to 1100 mbar and at two different temperatures (25 °C (298.15 K) and 40 °C (313.15 K)). Temperature control was achieved by using an external isothermal bath (Julabo F25-EH). Guest molecules were desorbed from the MOF pores before measurement (see **Table S1** for pretreatment conditions).

2.10. Nitrogen Sorption Measurements at 40 °C (313.15 K)

High temperature (40 °C, 313.15 K) N_2 Sorption isotherms were obtained with a volumetric instrument (a Micromeritics ASAP 2020 sorption analyzer) over a pressure range of 0 to 1100 mbar. Temperature control was achieved by using an external isothermal bath (Julabo F25-EH). Guest molecules were desorbed from the MOF pores before measurement (see **Table S1** for pretreatment conditions).

2.11. Isotherm Fitting

The pure component N_2 (40 °C only) and CO_2 adsorption isotherms were fitted to the Langmuir model over their entire pressure range (0 - 1100 mbar):

$$\boldsymbol{N = N_{Sat} \cdot \left(\frac{kp}{1 + kp}\right)} \quad (3)$$

Where:

$\boldsymbol{p}$ is the pressure (mbar) of gas (CO_2 or N_2, as applicable) at equilibrium with the adsorbed phase.

$\boldsymbol{N}$ is the quantity of gas adsorbed (in mmol per gram of adsorbent, mmol·g^{-1}) at pressure $\boldsymbol{p}$.

$\boldsymbol{N_{Sat}}$ is the quantity of gas adsorbed (in mmol per gram of adsorbent, mmol·g^{-1}) at saturation.

$\boldsymbol{k}$ is the adsorption affinity (mbar^{-1}).

The values of the parameters ($\boldsymbol{N_{Sat}}$ and $\boldsymbol{k}$) obtained from the Langmuir fits of our isotherms can be found in **Table S12** and **Table S13**. Plots of the adsorption isotherms with their corresponding fits can be found in **Figure S37** and **Figure S38**.

3. Detailed Analysis Methods

Table of Contents

3.1. Calculating the "Relative Intensity of the Broad Peak", $Rel(I)_{B.P.}$

In accordance with our previous study,[3] $Rel(I)_{B.P.}$ values were calculated by fitting four key reflections in the UiO-66 PXRD patterns, extracting their intensities, and entering the values into **Equation (4)** (see below). A single background term was also included in the fits, which were performed with Topas Academic version 4.2. The "broad peak" (see **Figure S1** below) was fit to either the Split Pearson VII (SPVII) or Split Pseudo-Voigt (SPV) function (depending on which model gave the lowest error), while the three most intense UiO-66 reflections (the (111), (200), and (600) reflections, see **Figure S1** below) were fit to the Pseudo-Voigt function. $Rel(I)_{B.P.}$ values were then calculated by dividing the intensity of the broad peak by the average of the 3 UiO-66 peak intensities:

$$Rel(I)_{B.P.} = \frac{I(Broad\ Peak)}{((I(111) + I(200) + I(600))/3)} \quad (4)$$

The 4 fitted peaks are emphasized in **Figure S1**, in which the PXRD pattern obtained on 50Benz-HA is displayed:

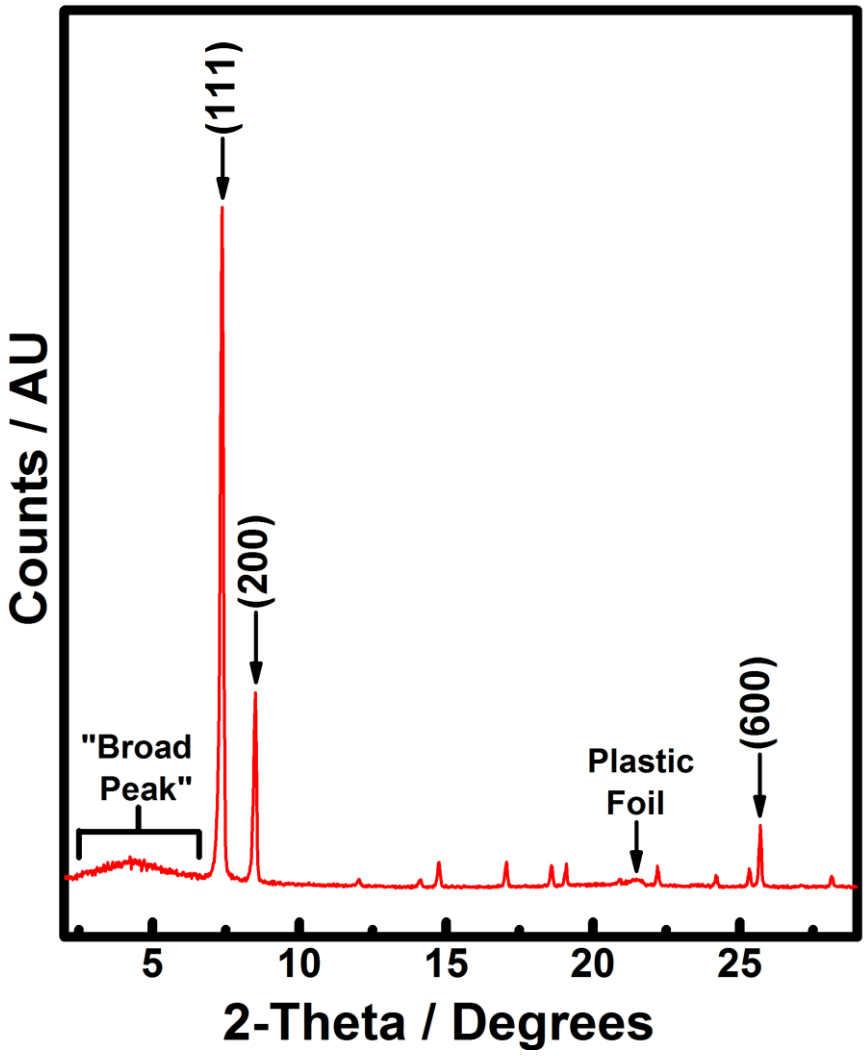

Figure S1. PXRD pattern obtained on 50Benz-HA.

3.2. Calculating the BET surface Area

BET surface areas were calculated by applying the linearized BET equation to our (77 K) nitrogen adsorption isotherms, both those simulated from model structures and those experimentally measured:

$$\frac{P/P_0}{V_a(1-P/P_0)} = \frac{C-1}{V_m C}(P/P_0) + \frac{1}{V_m C} \quad (5)$$

Where:

P and P_0 are the equilibrium and saturation pressure of the adsorbate, respectively.

V_a is the amount of gas adsorbed. In our case, the units are in $cm^3(STP)g^{-1}$.

V_m is the amount of gas required to form a monolayer on the adsorbent. Units are as above.

C is the BET constant (dimensionless).

The first step of the method is to enter the adsorption data into a plot of $\frac{P/P_0}{V_a(1-P/P_0)}$ vs. P/P_0. A linear region of the resulting plot is then identified and fitted. However, many such linear ranges can exist, and different ranges can sometimes yield significantly different BET surface areas.[7-10] It is thus of utmost importance to choose the "correct" range. To this end, we apply the BET consistency criteria, which were originally outlined by Rouquerol et al. and have now been endorsed in various studies:[7-10]

1) The pressure should be limited to the range in which $V_a(1-P/P_0)$ increases continuously as a function of the relative pressure P/P_0.
2) The relative pressure (P/P_0) at which the monolayer is formed (calculated from the fit as $\frac{1}{\sqrt{C+1}}$) must be within the chosen relative pressure (P/P_0) range.
3) The C value obtained from the fit must be positive.

Upon finding a P/P_0 range that satisfies all 3 criteria, we further fine-tuned the range to obtain the best linear fit (i.e. maximum R^2 value) in which the 3 criteria were still fulfilled. The volume of the monolayer (V_m) and the BET constant (C) were then extracted from the slope $\left(\frac{C-1}{V_m C}\right)$ and intercept $\left(\frac{1}{V_m C}\right)$ of the fit.

Finally, the BET surface area was calculated with the following equation:

$$BET\ S.A. = \frac{N_a P V_m}{RT} \cdot \sigma_0 \quad (6)$$

Where:

N_a is Avagadro's number (= 6.022 $x10^{23}$ mol^{-1}), P is atmospheric pressure (= 101.325 kPa), R is the gas constant (= 8314.46 $cm^3 \cdot kPa \cdot K^{-1} \cdot mol^{-1}$), T is the standard temperature (= 273.15 K), and σ_0 is the cross sectional area of the adsorbate (= 1.62 $x10^{-19}$ m^2 for N_2).

3.2.1. Example BET Analysis: 50Benz-HA

The determination of the BET surface of 50Benz-HA is demonstrated as an example in **Figure S2** below:

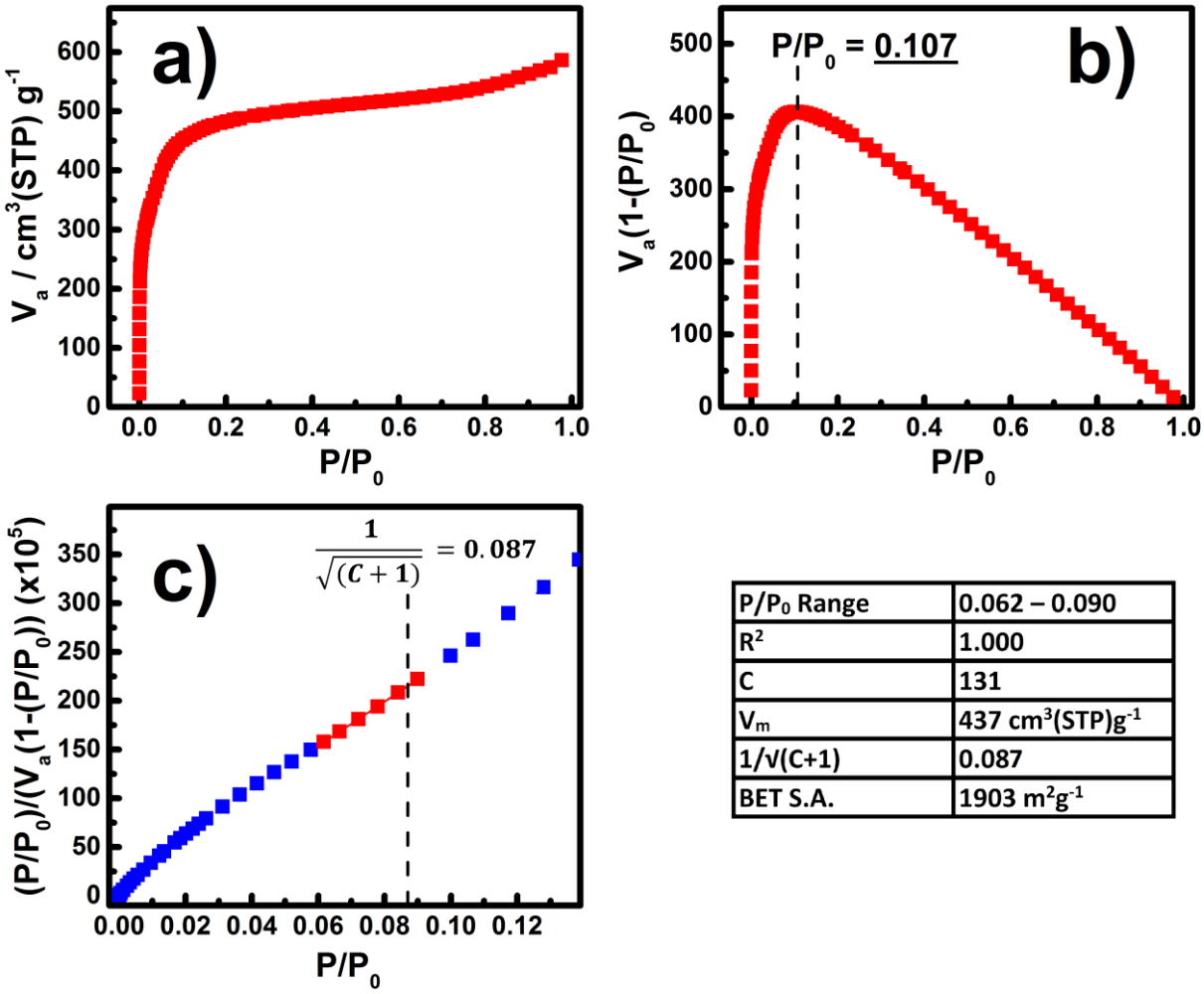

P/P$_0$ Range	0.062 – 0.090
R^2	1.000
C	131
V_m	437 cm^3(STP)g^{-1}
1/√(C+1)	0.087
BET S.A.	1903 m^{2}g^{-1}

Figure S2. BET analysis of 50Benz-HA.

The nitrogen adsorption isotherm obtained on 50Benz-HA is displayed in part a) of the figure. The data presented in the rest of the figure is derived from this isotherm.

Part b) of the figure concerns the 1st consistency criterion. One can see that $\boldsymbol{V_a(1 - P/P_0)}$ increases continuously as a function of $\boldsymbol{P/P_0}$ until $\boldsymbol{P/P_0}$ = **0.107**, a value highlighted by the vertical dashed line on the figure. In accordance with the 1st consistency criterion, the entire $\boldsymbol{P/P_0}$ range used for the BET analysis must be ≤ **0.107**.

Displayed in part c) of the figure is the BET plot in which the linear range was chosen. In order to maximize the correlation (R^2 = 1.000), only the points shown in red were included in the fit. In accordance with the 2nd consistency criterion, the value for $\frac{1}{\sqrt{C+1}}$ (= 0.087, as highlighted by the vertical dashed line) is within the chosen pressure range ($\boldsymbol{P/P_0}$ = 0.062 - 0.090).

Finally, the table in the figure provides all the information relevant to the BET analysis. In accordance with the 3rd consistency criterion, the value of the BET constant, $\boldsymbol{C}$, is positive (= 131).

3.3. Calculating Molar Ratios via Dissolution / ^{1}H NMR

Table of Contents

3.3.1. Introduction

Dissolution/^{1}H NMR involves the dissolution (a.k.a. "digestion" or "disassembly") of the organic portion of a MOF (linker, modulator, solvent etc.) in a deuterated digestion medium, followed by measurement with liquid ^{1}H NMR spectroscopy. This allows one to:

1) Identify the organic components in the MOF. Most of the time, the organic components that you detect are those intentionally added to the MOF synthesis. However, there are occasional surprises, as exemplified by the detection of a very large amount of formate ligands in 50Benz-HA, despite the fact that absolutely no formic acid was used in its synthesis.

2) Detect impurities. During our initial PSE trials for this work, we detected a significant amount of organic impurities in L-Serine functionalized samples when we dried them directly after solvent exchange with acetone (see **Section 1.5**). Fortunately, a second solvent exchange with dichloromethane was found to alleviate this problem.

3) Determine the molar ratios between the organic components. Such analysis exploits the fact that ^{1}H NMR spectroscopy is a quantitative technique, and is achieved by integrating the signals in the spectra and performing simple calculations. This type of analysis is particularly important to this study.

In this section, we demonstrate how the molar ratios of interest to this work were calculated. To specify, the three molar ratios were:

1) The benzoate : BDC^{2-} molar ratio $\left(\frac{\mathbf{Benz.}}{\mathbf{BDC}}\mathbf{m}_{\boldsymbol{R}}\right)$.
2) The formate : BDC^{2-} molar ratio $\left(\frac{\mathbf{Form.}}{\mathbf{BDC}}\mathbf{m}_{\boldsymbol{R}}\right)$.
3) The L-Serine : BDC^{2-} molar ratio $\left(\frac{\mathbf{Ser.}}{\mathbf{BDC}}\mathbf{m}_{\boldsymbol{R}}\right)$.

We start by deriving a general equation which can be used to calculate the molar ratio between two molecules from ^{1}H NMR data. Next, we show how the various signals were integrated. This is important to this work because two of the most critical ^{1}H NMR signals overlapped with one another, making it impossible to ***directly*** obtain integrals on the individual signals. However, we go on to show how that this problem can be solved by integrating groups of signals and performing simple arithmetic. Finally, we derive equations for the three molar ratios of interest to this work (see above) and end with a worked example.

Those who wish to skip the details and derivations are advised to jump straight to the worked example, which can be found in **Section 3.3.5**.

3.3.2. General Equation for Calculating the Molar Ratio between Two Molecules

As mentioned in the previous subsection, integrating dissolution/^{1}H NMR spectra affords one the ability to calculate the molar ratios between the organic components in a MOF (linker, modulator, solvent, etc.). However, when ^{1}H NMR spectra are integrated, we only obtain the relative number of ***equivalent active nuclei*** that give rise to the signals, not the relative number of molecules to which they can be attributed.

To emphasize this point, imagine the dissolution/^{1}H NMR spectrum obtained on a hypothetical MOF sample in which there is an equimolar mixture of BDC, acetate, and formate. Despite the fact that the 3 molecules are present in equal quantities, the intensity of their respective NMR signals would not be in a ratio of 1:1:1. Instead, integrating their signals would reveal an intensity ratio of 4:3:1 (BDC: acetate: formate). This is due to the variation in the number of equivalent non-labile protons in their molecular structures: BDC has 4 equivalent non-labile protons on its benzene ring, acetate features a methyl group in which all 3 protons are equivalent, while formate possesses just one non-labile proton.

Determining the molar ratio between different molecules therefore requires a normalization whereby each integral is divided by the number of equivalent nuclei from which the signal originates. A general equation for the molar ratio between 2 molecules (**Molecule1** and **Molecule2**) therefore takes the form:

$$\frac{\mathbf{Molecule1}}{\mathbf{Molecule2}}\mathbf{m_R} = \left(\frac{\mathbf{Molecule1\ Int.}}{\mathbf{N_{HMolecule1}}}\right) / \left(\frac{\mathbf{Molecule2\ Int.}}{\mathbf{N_{HMolecule2}}}\right) \qquad (7)$$

Or, in our preferred form where the two terms are multiplied rather than divided:

$$\frac{\mathbf{Molecule1}}{\mathbf{Molecule2}}\mathbf{m_R} = \left(\frac{\mathbf{Molecule\ 1\ Int.}}{\mathbf{N_{HMolecule1}}}\right) \cdot \left(\frac{\mathbf{N_{HMolecule2}}}{\mathbf{Molecule\ 2\ Int.}}\right) \qquad (8)$$

Where,

$\frac{\mathbf{Molecule1}}{\mathbf{Molecule2}}\mathbf{m_R}$ is the molar ratio between **Molecule1** and **Molecule2**.

Molecule1 Int. and **Molecule2 Int.** are the numerical values of the integrals obtained on the **Molecule1** and **Molecule2** ^{1}H NMR signals.

$\mathbf{N_{HMolecule1}}$ and $\mathbf{N_{HMolecule1}}$ are the number of ***equivalent protons*** contributing to the respective ^{1}H NMR signals of **Molecule1** and **Molecule2** ***per molecule***.

Before deriving more specific equations for $\frac{\mathbf{Benz.}}{\mathbf{BDC}}\mathbf{m_R}$, $\frac{\mathbf{Form.}}{\mathbf{BDC}}\mathbf{m_R}$, and $\frac{\mathbf{Ser.}}{\mathbf{BDC}}\mathbf{m_R}$, it is important to demonstrate how the numerical values for the BDC^{2-}, benzoate, formate, and L-Serine ^{1}H NMR integrals were obtained. This is described in detail in the following subsection. Those who wish to skip the details and derivations and simply want to see how the $\frac{\mathbf{Benz.}}{\mathbf{BDC}}\mathbf{m_R}$, $\frac{\mathbf{Form.}}{\mathbf{BDC}}\mathbf{m_R}$, and $\frac{\mathbf{Ser.}}{\mathbf{BDC}}\mathbf{m_R}$ values were calculated in practice are advised to skip to the worked example presented in **Section 3.3.5**.

3.3.3. Integrating the Spectra

3.3.3.1. Benzoate and BDC^{2-} Signals

Ordinarily, integrating ^{1}H NMR spectra to determine molar ratios between organic species is a trivial task when the assignment of the signals is known. However, things get trickier when the NMR signals of different molecules overlap with one another, as is the case with benzoate and BDC^{2-} in the digestion medium used in this work (1M NaOH in D_2O). This is exemplified in **Figure S3** below, where the spectra acquired on benzoate and BDC^{2-} are compared with that obtained on 50Benz after digestion in 1M NaOH in D_2O:

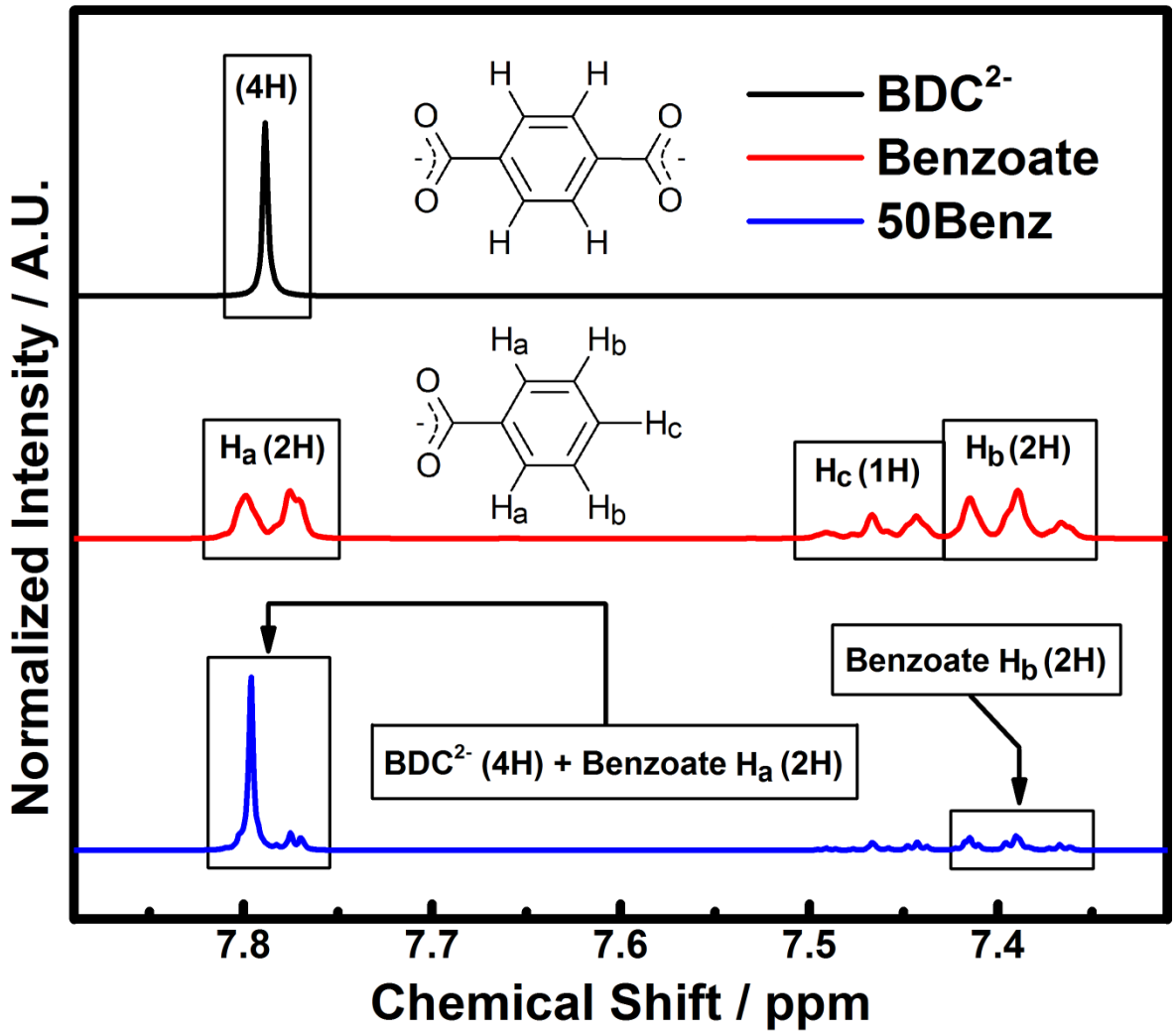

Figure S3. Comparison and assignment of the ^{1}H NMR spectra obtained on BDC^{2-}, benzoate, and 50Benz. The BDC^{2-} and benzoate spectra were obtained after dissolving small amounts of H_2BDC and benzoic acid in 600 µL of 1M NaOH in D_2O, respectively. The 50Benz spectrum (blue curve) was obtained after allowing 20 mg of 50Benz to digest in 600 uL 1M NaOH in D_2O for 24 hours (see **Section 2.2**).

Upon observation of the figure, one can see that the benzoate spectrum (red curve) is actually quite complex, despite the relative simplicity of the molecule. Its structure features 3 chemically distinct protons (labelled H_a, H_b, and H_c) which have been assigned to their corresponding ^{1}H NMR signals on the figure. As can be seen, the benzoate H_a signal partially overlaps with the sole ^{1}H NMR signal of BDC^{2-} (black curve). This makes it impossible to ***directly*** obtain an accurate integral for the BDC^{2-}

signal when both BDC^{2-} and benzoate are present in the spectrum, as is the case in all dissolution/^{1}H NMR spectra obtained in this work (e.g. 50Benz, blue curve in the figure above).

However, it is possible to obtain an accurate integral for the BDC^{2-} signal by integrating groups of signals and performing simple arithmetic. Essentially, we exploit the fact that benzoate's ^{1}H NMR spectrum features more than one signal. Of its 3 signals, two (denoted H_a and H_b on the figure) integrate for 2H, and thus the integral obtained on H_b (**Benz. H_b Int.**) is exactly equal to that obtained on H_a (**Benz. H_a Int.**):

$$\textbf{Benz. H}_\textbf{a}\ \textbf{Int.} = \textbf{Benz. H}_\textbf{b}\ \textbf{Int.} \tag{9}$$

With this equation in mind, obtaining an accurate integral on the BDC^{2-} signal was achieved by employing the following 4 step procedure:

1) Integrating the entire spectral region in which the overlapping BDC^{2-} and benzoate H_a signals are found. This region, dubbed the "(BDC + Benz. H_a) signal", is emphasized in the leftmost box on the blue curve in **Figure S3**. The numerical value of its integral (named "(**BDC + Benz. H_a**) **Int.**)" is equal to the number which would have been obtained if it were possible to accurately integrate the BDC^{2-} and benzoate H_a signals separately and sum their values:

$$(\textbf{BDC} + \textbf{Benz. H}_\textbf{a})\ \textbf{Int.} = \textbf{BDC Int.} + \textbf{Benz. H}_\textbf{a}\ \textbf{Int.} \tag{10}$$

2) Normalizing the value of the (BDC + Benz. H_a) integral. Although any arbitrary numerical value would suffice, we set it to **6.00** as standard practice. This value was chosen because 2 equivalent protons contribute to the benzoate H_a signal and 4 equivalent protons contribute to the BDC^{2-} signal, and 2 + 4 = **6.00**.

   Important: This normalization must be (and was) performed before reading off the numerical values of ***all*** other integrals, including those of formate and L-Serine (if present).

3) Integrating the benzoate H_b signal (see the rightmost box on the blue and red curves in **Figure S3**). This integral is named "**Benz. H_b Int.**".

4) Subtracting the numerical value of the benzoate H_b integral from that obtained on the (BDC + Benz. H_a) signal. This yields an accurate value for the BDC^{2-} integral (**BDC Int.**), as can be seen by substituting **Equation (9)** into **Equation (10)** and solving for **BDC Int.**:

$$(\textbf{BDC} + \textbf{Benz. H}_\textbf{a})\ \textbf{Int.} = \textbf{BDC Int.} + \textbf{Benz. H}_\textbf{a}\ \textbf{Int.} \tag{10}$$

Substituting **Benz. H_b Int.** for **Benz. H_a Int.** (see **Equation (9)**) gives us:

$$(\textbf{BDC} + \textbf{Benz. H}_\textbf{a})\ \textbf{Int.} = \textbf{BDC Int.} + \textbf{Benz. H}_\textbf{b}\ \textbf{Int.} \tag{11}$$

Solving for **BDC Int.**:

$$\textbf{BDC Int.} = (\textbf{BDC} + \textbf{Benz. H}_\textbf{a})\ \textbf{Int.} - \textbf{Benz. H}_\textbf{b}\ \textbf{Int.} \tag{12}$$

3.3.3.2. Formate and L-Serine Signals

The ^{1}H NMR spectra obtained on formate and L-Serine (doubly deprotonated due to the basic 1M NaOH in D_2O solvent) are displayed in **Figure S4**:

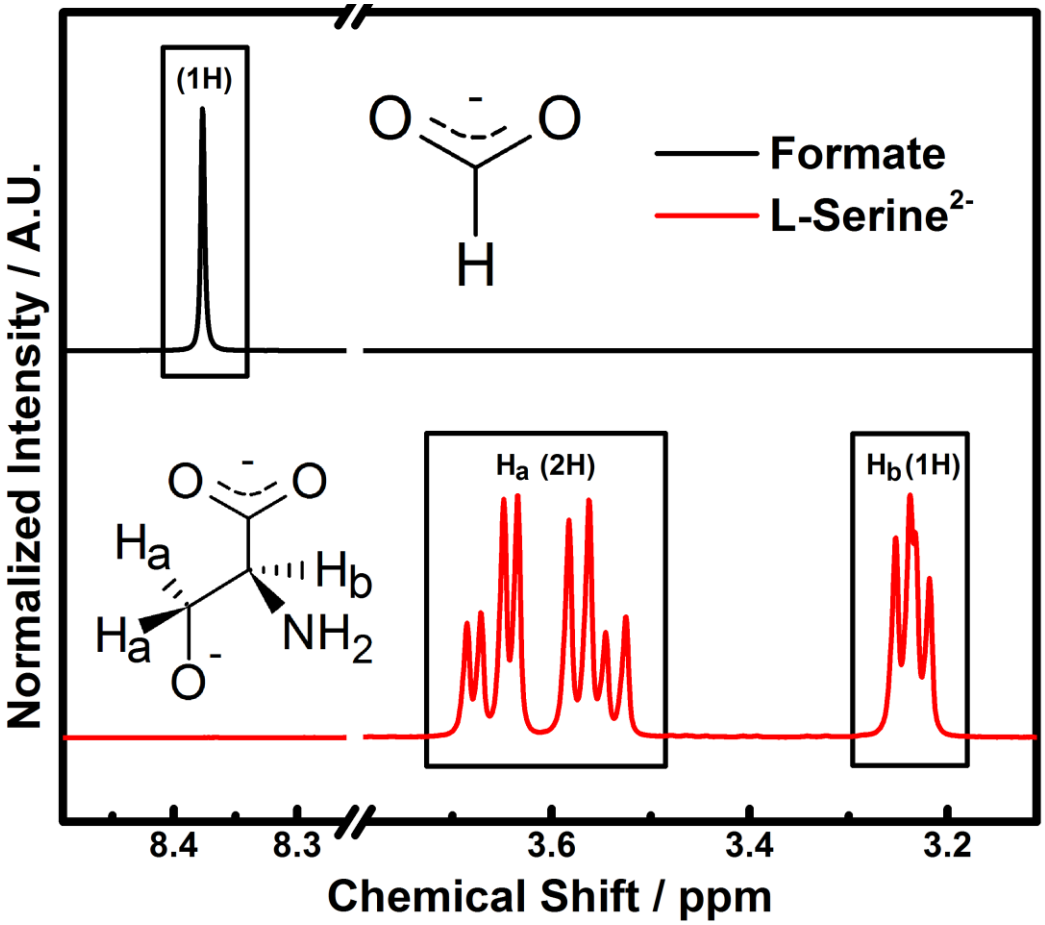

Figure S4. ^{1}H NMR spectra obtained on formate (black curve) and L-Serine (red curve). The spectra were obtained after dissolving small amounts of formic acid and L-Serine in 600 µL 1M NaOH in D_2O.

As one can see from the figure, formate's ^{1}H NMR spectrum (black curve) comprises just a solitary singlet. This is not surprising since there is only one non-labile proton in its chemical structure. Integrating the formate signal in dissolution/^{1}H NMR spectra is therefore straightforward.

The ^{1}H NMR spectrum obtained on L-Serine (red curve in the above figure) is more complex. This is a result of the chirality of the molecule and the fact that its chemical structure features 3 non-labile protons. Two of these protons (both labelled H_a on the structure in the figure) are chemically equivalent, generating the signal denoted "H_a (2H)" on the figure. It is this signal which was integrated and used to calculate $\frac{\mathbf{Ser.}}{\mathbf{BDC}}\mathbf{m}_{\boldsymbol{R}}$ (the L-Serine : BDC molar ratio) in the L-Serine functionalized UiO-66 samples (see **Section 3.3.4** for equation and **Section 4.5.1** for results).

Reminder: In order to obtain molar ratios from our dissolution/^{1}H NMR spectra, it was essential to integrate and normalize the "(BDC + Benz. H_a)" signal (see previous subsection) before reading off the numerical values of ***all*** other integrals, including those of formate and L-Serine (if present).

3.3.4. Deriving Equations for $\frac{\mathbf{Benz.}}{\mathbf{BDC}}\mathbf{m}_R$, $\frac{\mathbf{Form.}}{\mathbf{BDC}}\mathbf{m}_R$, and $\frac{\mathbf{Ser.}}{\mathbf{BDC}}\mathbf{m}_R$

Equation (8), the general equation originally presented in **Section 3.3.2**, can be modified to obtain expressions for the molar ratios between benzoate and BDC $\left(\frac{\mathbf{Benz.}}{\mathbf{BDC}}\mathbf{m}_R\right)$, formate and BDC $\left(\frac{\mathbf{Form.}}{\mathbf{BDC}}\mathbf{m}_R\right)$, and L-Serine and BDC $\left(\frac{\mathbf{Ser.}}{\mathbf{BDC}}\mathbf{m}_R\right)$. To do so, we simply need to replace all instances of "**Molecule1**" and "**Molecule2**" with the relevant molecular identities.

Since "**BDC**" is the denominator in all three desired molar ratios ($\frac{\mathbf{Benz.}}{\mathbf{BDC}}\mathbf{m}_R$, $\frac{\mathbf{Form.}}{\mathbf{BDC}}\mathbf{m}_R$, and $\frac{\mathbf{Ser.}}{\mathbf{BDC}}\mathbf{m}_R$), we can begin by substituting "**BDC**" for all instances of "**Molecule2**" (the denominator in the general molar ratio, $\frac{\mathbf{Molecule1}}{\mathbf{Molecule2}}\mathbf{m_R}$) in **Equation (8)**:

$$\frac{\mathbf{Molecule1}}{\mathbf{Molecule2}}\mathbf{m_R} = \left(\frac{\mathbf{Molecule\ 1\ Int.}}{\mathbf{N_{HMolecule1}}}\right)\cdot\left(\frac{\mathbf{N_{HMolecule2}}}{\mathbf{Molecule\ 2\ Int.}}\right) \qquad (8)$$

Substituting all instances of "**Molecule2**" with "**BDC**" gives us:

$$\frac{\mathbf{Molecule1}}{\mathbf{BDC}}\mathbf{m_R} = \left(\frac{\mathbf{Molecule\ 1\ Int.}}{\mathbf{N_{HMolecule1}}}\right)\cdot\left(\frac{\mathbf{N_{HBDC}}}{\mathbf{BDC\ Int.}}\right) \qquad (13)$$

Where:

$\mathbf{N_{HBDC}}$ is the number of ***equivalent ^{1}H nuclei*** contributing to the ^{1}H NMR signal of BDC ***per molecule***. As all 4 of the non-labile protons in BDC are equivalent, $\mathbf{N_{HBDC}} = \mathbf{4}$.

BDC Int. is the numerical value of the ^{1}H NMR Integral obtained on the BDC signal, as calculated by **Equation (12)** (see **Section 3.3.3.1** for derivation):

$$\mathbf{BDC\ Int.} = (\mathbf{BDC} + \mathbf{Benz.\,H_a})\ \mathbf{Int.} - \mathbf{Benz.\,H_b\ Int.} \qquad (12)$$

Where:

$(\mathbf{BDC} + \mathbf{Benz.\,H_a})\ \mathbf{Int.}$ is the numerical value of the ^{1}H NMR Integral obtained on the "(BDC + Benzoate H_a) signal" (see **Section 3.3.3.1**).

$\mathbf{Benz.\,H_b\ Int.}$ is the numerical value of the ^{1}H NMR Integral obtained on the "benzoate H_b signal" (see **Section 3.3.3.1**).

Substituting **Equation (12)** and $\mathbf{N_{HBDC} = 4}$ into **Equation (13)** gives us:

$$\frac{\mathbf{Molecule1}}{\mathbf{BDC}}\mathbf{m_R} = \left(\frac{\mathbf{Molecule1\ Int.}}{\mathbf{N_{HMolecule1}}}\right) \cdot \left(\frac{\mathbf{4}}{\left(\mathbf{(BDC + Benz.\ H_a)\ Int. - Benz.\ H_b\ Int.}\right)}\right) \quad (14)$$

The equations for $\frac{\mathbf{Benz.}}{\mathbf{BDC}}\mathbf{m_R}$, $\frac{\mathbf{Form.}}{\mathbf{BDC}}\mathbf{m_R}$, and $\frac{\mathbf{Ser.}}{\mathbf{BDC}}\mathbf{m_R}$ are obtained by modifying this general equation.

First, the equation for $\frac{\mathbf{Benz.}}{\mathbf{BDC}}\mathbf{m_R}$ is derived by substituting "**Benz.**" (the numerator in the benzoate/BDC molar ratio, $\frac{\mathbf{Benz.}}{\mathbf{BDC}}\mathbf{m_R}$) for all instances of "**Molecule1**" (the numerator in the molecule1/BDC molar ratio, $\frac{\mathbf{Molecule1}}{\mathbf{BDC}}\mathbf{m_R}$) in **Equation (14)**:

$$\frac{\mathbf{Molecule1}}{\mathbf{BDC}}\mathbf{m_R} = \left(\frac{\mathbf{Molecule1\ Int.}}{\mathbf{N_{HMolecule1}}}\right) \cdot \left(\frac{\mathbf{4}}{\left(\mathbf{(BDC + Benz.\ H_a)\ Int. - Benz.\ H_b\ Int.}\right)}\right) \quad (14)$$

Substituting all instances of "**Molecule1**" with "**Benz.**" gives us:

$$\frac{\mathbf{Benz.}}{\mathbf{BDC}}\mathbf{m_R} = \left(\frac{\mathbf{Benz.\ Int.}}{\mathbf{N_{HBenz.}}}\right) \cdot \left(\frac{\mathbf{4}}{\left(\mathbf{(BDC + Benz.\ H_a)\ Int. - Benz.\ H_b\ Int.}\right)}\right) \quad (15)$$

Where:

Benz. Int. is the numerical value of the ^{1}H NMR Integral obtained on the benzoate signal, specifically the H_b signal (see **Section 3.3.3.1**). This integral will therefore be exclusively named "**Benz. H_b Int.**" hereafter.

$\mathbf{N_{HBenz.}}$ is the number of ***equivalent ^{1}H nuclei*** contributing to the integrated benzoate signal ***per molecule***. Two non-labile protons contribute to the benzoate H_b signal (see **Section 3.3.3.1**), so $\mathbf{N_{HBenz} = 2}$.

Substituting $\mathbf{Benz.\ Int. = Benz.\ H_b\ Int.}$ and $\mathbf{N_{HBenz} = 2}$ into **Equation (15)** gives us the final equation for $\frac{\mathbf{Benz.}}{\mathbf{BDC}}\mathbf{m_R}$:

$$\frac{\mathbf{Benz.}}{\mathbf{BDC}}\mathbf{m_R} = \left(\frac{\mathbf{Benz.\ H_b\ Int.}}{\mathbf{2}}\right) \cdot \left(\frac{\mathbf{4}}{\left(\mathbf{(BDC + Benz.\ H_a)\ Int. - Benz.\ H_b\ Int.}\right)}\right) \quad (16)$$

Likewise, the expression for $\frac{\mathbf{Form.}}{\mathbf{BDC}}\mathbf{m}_{\boldsymbol{R}}$ is derived by substituting "**Form.**" for all instances of "**Molecule1**" in **Equation (14)**:

$$\frac{\mathbf{Molecule1}}{\mathbf{BDC}}\mathbf{m_R} = \left(\frac{\mathbf{Molecule1\ Int.}}{\mathbf{N_{HMolecule1}}}\right) \cdot \left(\frac{\mathbf{4}}{\left((\mathbf{BDC + Benz.\ H_a})\ \mathbf{Int.} - \mathbf{Benz.\ H_b\ Int.}\right)}\right) \qquad (14)$$

Substituting all instances of "**Molecule1**" with "**Form.**" gives us:

$$\frac{\mathbf{Form.}}{\mathbf{BDC}}\mathbf{m_R} = \left(\frac{\mathbf{Form.\ Int.}}{\mathbf{N_{HForm.}}}\right) \cdot \left(\frac{\mathbf{4}}{\left((\mathbf{BDC + Benz.\ H_a})\ \mathbf{Int.} - \mathbf{Benz.\ H_b\ Int.}\right)}\right) \qquad (17)$$

Where:

Form. Int. is the numerical value of the ^{1}H NMR Integral obtained on the formate signal (see **Section 3.3.3.2**)

$\mathbf{N_{HForm.}}$ is the number of ***equivalent ^{1}H nuclei*** contributing to the formate signal ***per molecule***. Only one non-labile proton contributes to the formate signal, so $\mathbf{N_{HForm.} = 1}$.

Substituting $\mathbf{N_{HForm.} = 1}$ into **Equation (17)** gives us the final equation for $\frac{\mathbf{Form.}}{\mathbf{BDC}}\mathbf{m}_{\boldsymbol{R}}$:

$$\frac{\mathbf{Form.}}{\mathbf{BDC}}\mathbf{m_R} = \left(\frac{\mathbf{Form.\ Int.}}{\mathbf{1}}\right) \cdot \left(\frac{\mathbf{4}}{\left((\mathbf{BDC + Benz.\ H_a})\ \mathbf{Int.} - \mathbf{Benz.\ H_b\ Int.}\right)}\right) \qquad (18)$$

Finally, the expression for $\frac{\mathbf{Ser.}}{\mathbf{BDC}}\mathbf{m_R}$ is derived by substituting "**Ser.**" for all instances of "**Molecule1**" in **Equation (14)**:

$$\frac{\mathbf{Molecule1}}{\mathbf{BDC}}\mathbf{m_R} = \left(\frac{\mathbf{Molecule1\ Int.}}{\mathbf{N_{HMolecule1}}}\right) \cdot \left(\frac{\mathbf{4}}{\left((\mathbf{BDC + Benz.\ H_a})\ \mathbf{Int.} - \mathbf{Benz.\ H_b\ Int.}\right)}\right) \qquad (14)$$

Substituting all instances of "**Molecule1**" with "**Ser.**" gives us:

$$\frac{\mathbf{Ser.}}{\mathbf{BDC}}\mathbf{m_R} = \left(\frac{\mathbf{Ser.\ Int.}}{\mathbf{N_{HSer.}}}\right) \cdot \left(\frac{\mathbf{4}}{\left((\mathbf{BDC + Benz.\ H_a})\ \mathbf{Int.} - \mathbf{Benz.\ H_b\ Int.}\right)}\right) \qquad (19)$$

Where:

Ser. Int. is the numerical value of the ^{1}H NMR Integral obtained on the L-Serine signal, specifically the H_a signal (see **Section 3.3.3.2**). This integral will therefore be exclusively named "**Ser. H_a Int.**" hereafter.

$\mathbf{N_{HSer.}}$ is the number of ***equivalent ^1H nuclei*** contributing to the integrated L-Serine signal ***per molecule***. Two non-labile protons contribute to the L-Serine H_a signal, so $\mathbf{N_{HSer.}} = \mathbf{2}$.

Substituting $\mathbf{Ser.\ Int.} = \mathbf{Ser.\ H_a\ Int.}$ and $\mathbf{N_{HSer.}} = \mathbf{2}$ into **Equation (19)** gives us the final equation for $\frac{\mathbf{Ser.}}{\mathbf{BDC}}\mathbf{m_R}$:

$$\frac{\mathbf{Ser.}}{\mathbf{BDC}}\mathbf{m_R} = \left(\frac{\mathbf{Ser.\ H_a\ Int.}}{\mathbf{2}}\right) \cdot \left(\frac{\mathbf{4}}{\left((\mathbf{BDC + Benz.\ H_a})\ \mathbf{Int.} - \mathbf{Benz.\ H_b\ Int.}\right)}\right) \qquad (20)$$

3.3.5. Worked Example: Determining the Molar Ratios in 1.5M-Ser

The sample named 1.5M-Ser (see **Section 1.5.1**) contains all the ligands of interest to this study (BDC^{2-}, benzoate, formate, and L-Serine) and thus its dissolution/^{1}H NMR spectrum is ideal for exemplifying how the desired molar ratios ($\frac{\mathbf{Benz.}}{\mathbf{BDC}}\mathbf{m_R}$, $\frac{\mathbf{Form.}}{\mathbf{BDC}}\mathbf{m_R}$, and $\frac{\mathbf{Ser.}}{\mathbf{BDC}}\mathbf{m_R}$) were calculated. To this end, let us consider its dissolution/^{1}H NMR spectrum, shown in **Figure S5** below:

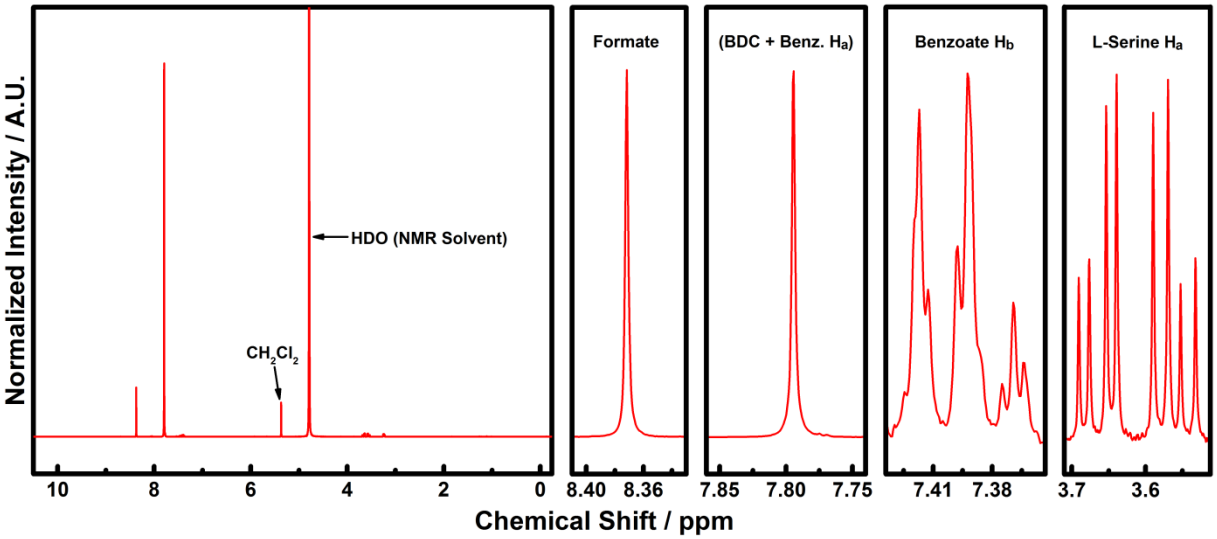

Figure S5. Dissolution/^{1}H NMR spectrum obtained on 1.5M-Ser. The full spectrum is shown in the leftmost plot, while the other 4 plots magnify the signals which were integrated to obtain the desired molar ratios. See the labels at the top of the plots for their assignments. The y-scale range varies in each plot. The amount of benzoate in this sample is significantly less than in 50Benz, whose dissolution/^{1}H NMR spectrum was shown in **Figure S3**. As a result, the benzoate H_a signal is almost invisible at the y-scale range adopted in the "(BDC + Benz. H_a)" plot. However, the amount of benzoate in this sample is certainly not negligible, as can be seen from the clarity of the "Benzoate H_b" signal in its own plot. For the sake of accurate analysis, it is thus still important to integrate the (BDC + Benz. H_a) signal over its full ppm range (*ca.* 7.86-7.74).

The steps to obtaining the molar ratios ($\frac{\mathbf{Benz.}}{\mathbf{BDC}}\mathbf{m_R}$, $\frac{\mathbf{Form.}}{\mathbf{BDC}}\mathbf{m_R}$, and $\frac{\mathbf{Ser.}}{\mathbf{BDC}}\mathbf{m_R}$) from this and all other dissolution/^{1}H NMR spectra measured herein were as follows:

1) The "(BDC + Benz. H_a)" signal (see middle panel of the above figure and **Section 3.3.3.1** for details) was integrated and its value was normalized to 6.00. For the sake of accurate analysis, it is important to integrate the full ppm range engulfed by the BDC^{2-} and benzoate H_a signals, even when the benzoate H_a signal is dwarfed by that of BDC^{2-}, as is the case in the spectrum above (see figure caption for details).

2) The "Benzoate H_b", "Formate", and "L-Serine H_a" signals (each emphasized by their own panel in the above figure) were integrated, giving the numerical values of $\mathbf{Benz.\,H_b\,Int.}$, $\mathbf{Form.\,Int.}$, and $\mathbf{Ser.\,H_a\,Int.}$, respectively. The following values were obtained when integrating the spectrum above:

$$\mathbf{Benz.\,H_b\,Int.} = \underline{\mathbf{0.12}}$$

$$\mathbf{Form.\,Int.} = \underline{\mathbf{0.61}}$$

$$\mathbf{Ser.\,H_a\,Int.} = \underline{\mathbf{0.31}}$$

3) Finally, the molar ratios between benzoate and BDC $\left(\frac{\textbf{Benz.}}{\textbf{BDC}}\mathbf{m_R}\right)$, formate and BDC $\left(\frac{\textbf{Form.}}{\textbf{BDC}}\mathbf{m_R}\right)$, and L-Serine and BDC $\left(\frac{\textbf{Ser.}}{\textbf{BDC}}\mathbf{m_R}\right)$ were obtained by inserting the above integral values into **Equations (16)**, **(18)**, and **(20)** , respectively (see **Section 3.3.4** for derivations):

$$\frac{\textbf{Benz.}}{\textbf{BDC}}\mathbf{m_R} = \left(\frac{\textbf{Benz. H}_\textbf{b}\textbf{ Int.}}{\mathbf{2}}\right)\cdot\left(\frac{\mathbf{4}}{\left(\textbf{(BDC + Benz. H}_\textbf{a}\textbf{) Int.} - \textbf{Benz. H}_\textbf{b}\textbf{ Int.}\right)}\right) \qquad (16)$$

$$\frac{\textbf{Benz.}}{\textbf{BDC}}\mathbf{m_R} = \left(\frac{\mathbf{0.12}}{\mathbf{2}}\right)\cdot\left(\frac{\mathbf{4}}{\mathbf{(6.00 - 0.12)}}\right)$$

$$\frac{\textbf{Benz.}}{\textbf{BDC}}\mathbf{m_R} = \underline{\mathbf{0.04}}$$

$$\frac{\textbf{Form.}}{\textbf{BDC}}\mathbf{m_R} = \left(\frac{\textbf{Form. Int.}}{\mathbf{1}}\right)\cdot\left(\frac{\mathbf{4}}{\left(\textbf{(BDC + Benz. H}_\textbf{a}\textbf{) Int.} - \textbf{Benz. H}_\textbf{b}\textbf{ Int.}\right)}\right) \qquad (18)$$

$$\frac{\textbf{Form.}}{\textbf{BDC}}\mathbf{m_R} = \left(\frac{\mathbf{0.61}}{\mathbf{1}}\right)\cdot\left(\frac{\mathbf{4}}{\mathbf{(6.00 - 0.12)}}\right)$$

$$\frac{\textbf{Form.}}{\textbf{BDC}}\mathbf{m_R} = \underline{\mathbf{0.41}}$$

$$\frac{\textbf{Ser.}}{\textbf{BDC}}\mathbf{m_R} = \left(\frac{\textbf{Ser. H}_\textbf{a}\textbf{ Int.}}{\mathbf{2}}\right)\cdot\left(\frac{\mathbf{4}}{\left(\textbf{(BDC + Benz. H}_\textbf{a}\textbf{) Int.} - \textbf{Benz. H}_\textbf{b}\textbf{ Int.}\right)}\right) \qquad (20)$$

$$\frac{\textbf{Ser.}}{\textbf{BDC}}\mathbf{m_R} = \left(\frac{\mathbf{0.31}}{\mathbf{2}}\right)\cdot\left(\frac{\mathbf{4}}{\mathbf{(6.00 - 0.12)}}\right)$$

$$\frac{\textbf{Ser.}}{\textbf{BDC}}\mathbf{m_R} = \underline{\mathbf{0.11}}$$

Note: the integral values and molar ratios presented and calculated above are later summarized in **Table S9** (**Section 4.5.1**), along with those obtained/calculated on all the other samples (except 50Benz, whose integral values and molar ratios are presented in **Table S3** in **Section 4.2.1**).

3.4. Using a Combination of TGA and Dissolution / ^{1}H NMR to Quantify Linker Deficiencies and Estimate the Compositions of Defective UiO-66 Samples with Benzoate Ligands

Table of Contents

3.4.1. Introduction

In the supporting information of a previous study,[3] we provided a (TGA based) procedure for quantifying linker deficiencies in defective UiO-66 samples. In said samples, the defects were compensated by acetate, formate, difluoroacetate, or trifluoroacetate ligands, but none of them contained benzoate ligands. As it turns out, our previously published method cannot be applied to UiO-66 samples whose defects are (wholly or partially) compensated by benzoate. We have therefore devised a new, more general method which also allows us to quantify linker deficiencies in benzoate-containing UiO-66 samples.

In this section, we begin by reiterating the basic principles of quantitative TGA analysis on UiO-66, and quickly move on to describing our previously published method for calculating the number of linker deficiencies in defective samples. One should keep in mind that these basic principles are still of central importance to the new procedure. Next, we demonstrate why the old method is not suitable for analyzing UiO-66 samples with benzoate ligands, and go on to derive our new, more general method which circumvents the problem. Finally, we show that the method (which makes use of quantitative data from both TGA and dissolution/^{1}H NMR) can be extended towards obtaining reasonable estimates for the full composition of these materials and provide worked examples of such analysis. It should be noted that a similar method for estimating the composition of defective UiO-66 samples is outlined in the supporting information of our previous paper,[3] however it is again not suitable for analyzing benzoate containing samples.

As a final remark, we note that this section is rather extensive and contains many details and derivations. Readers who do not wish to read through said details but are nevertheless interested in the effectiveness of the method are advised to jump straight to the worked examples, which can be found in **Section 3.4.7**.

3.4.2. Quantitative Analysis of UiO-66 via TGA: Basic Principles

Quantitative analysis of TGA data obtained on UiO MOFs is made with an important assumption: that the residue in each TGA experiment is pure $\mathbf{ZrO_2}$. In order to best ensure that this is the case, our TGA experiments were run all the way up to 900 °C under a flow of an oxygen containing gas mixture (synthetic air), and with a relatively slow temperature ramp (5 °C/min). Such conditions should ensure the complete combustion of organics and the conversion of zirconium to the (IV) oxide.

With this in mind, consider the reaction for the complete combustion of ideal (defect-free) UiO-66 in the dehydroxylated form, $\mathbf{Zr_6O_6(BDC)_6}$:

$$\mathbf{Zr_6O_6(BDC)_6\ (s) + 45\ O_2\ (g)\ \rightarrow\ 6ZrO_2\ (s) + 48\ CO_2\ (g) + 12\ H_2O\ (g)}$$

The molar mass of $\mathbf{Zr_6O_6(BDC)_6}$ is **1628.03 g mol^{-1}**, a factor of **2.202** higher than the only solid residue - 6 moles of $\mathbf{ZrO_2}$ (= **739.34 g mol^{-1}**). Thus, if the end weight (i.e. the weight at 900 °C) of a TGA experiment on UiO-66 is normalized to **100 %**, then the TGA plateau of the empty, solvent free, and dehydroxylated MOF should ideally be found at 100 x 2.202 = **220.2 %** on the weight axis. However, it typically falls significantly short of this theoretical weight, meaning that the UiO-66 framework is lighter than that formulated by the ideal molecular formula. This observation was the first indication of linker deficiencies in UiO-66.[11] It is important to note that ***both*** missing linker and missing cluster defects introduce linker deficiencies to the UiO-66 framework, meaning that TGA cannot distinguish between the 2 types of defect, a point that we stressed in our previous paper.[3]

Returning to the method, one can also calculate the theoretical plateau of ideal hydroxylated UiO-66, $\mathbf{Zr_6O_4(OH)_4(BDC)_6}$, which has a molar mass of **1664.06 g mol^{-1}**. This is a factor of **2.251** higher than the mass of 6 moles of $\mathbf{ZrO_2}$ (= **739.34 g mol^{-1}**), and thus its TGA plateau is expected to be found at 100 x 2.251 = **225.1 %** on the weight axis when the end weight is normalized to **100 %**. More generally, the theoretical TGA plateau weight ($\boldsymbol{W_{Theo.Plat.}}$) of **any** Zr_6 MOF composition can be calculated with the following equation:

$$\boldsymbol{W_{Theo.Plat.}} = \left(\frac{\boldsymbol{M_{Comp.}}}{\boldsymbol{M_{6\ ZrO_2}}}\right) \cdot \boldsymbol{W_{End}} \qquad (21)$$

Where:

$\boldsymbol{M_{Comp.}}$ is the molar mass of the composition of interest.

$\boldsymbol{M_{6\ ZrO_2}}$ is the molar mass of 6 moles of zirconium (IV) oxide (= **739.34 g mol^{-1}**).

$\boldsymbol{W_{End}}$ is the end weight of the TGA run (= **100 %** if normalized as described above).

Note: when $\boldsymbol{W_{End}}$ is normalized to **100 %**, entering the molar masses ($\boldsymbol{M_{Comp.}}$) of ideal hydroxylated (**1664.06 g mol^{-1}**) and dehydroxylated (**1628.03 g mol^{-1}**) UiO-66 yields theoretical TGA plateau weights of **225.1** and **220.2 %**, respectively. These are the same values as mentioned above.

3.4.2.1. Example: UiO-66-Ideal

UiO-66-Ideal (a near defect-free UiO-66 sample, as demonstrated by extensive characterization in the supporting information in our previous paper)[3] is very useful when it comes to scrutinizing the two theoretical TGA plateaus proposed in the previous subsection. The synthesis method used to obtain UiO-66-Ideal is outlined in **Section 1.3**. The (normalized) TGA–DSC results obtained on the sample are shown in **Figure S6** below:

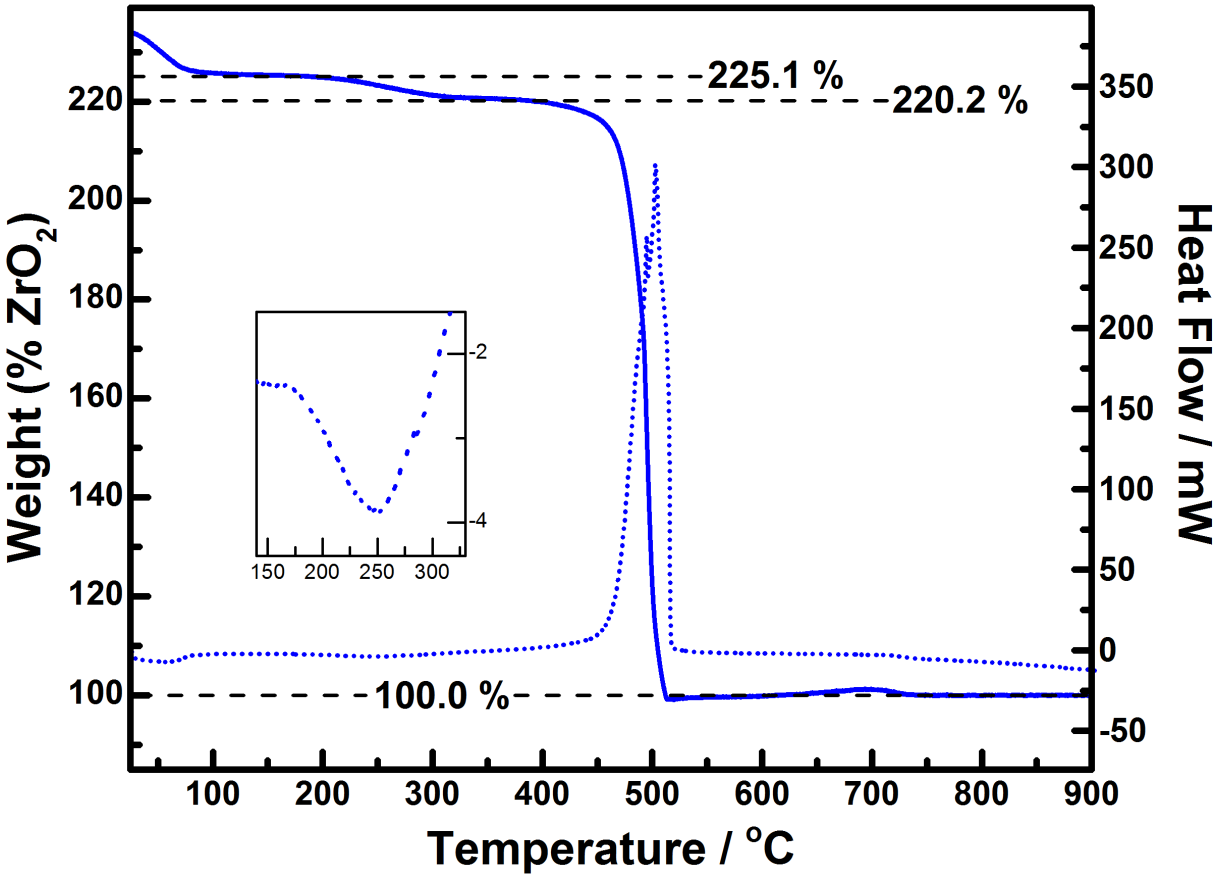

Figure S6. TGA-DSC results obtained on UiO-66-Ideal (see **Section 1.3** for synthesis method). Solid curve, left axis - TGA trace (normalized such that end weight = 100 %). Dotted curve, right axis – DSC trace. The two uppermost horizontal dashed lines pinpoint the theoretically expected TGA plateaus for ideal UiO-66 in the hydroxylated (= 225.1 %) and dehydroxylated (= 220.2 %) forms. See the previous subsection for details on how these values were calculated. The inset emphasizes the endothermic DSC peak which accompanies the dehydroxylation weight loss step.

As can be seen, the two experimentally observed TGA plateau weights closely match those predicted by theory, which are emphasized by the two uppermost horizontal dashed lines. This indicates that the composition of the sample is in accordance with the ideal molecular formula for UiO-66, both when hydroxylated and dehydroxylated. Furthermore, the temperature range of the dehydroxylation weight loss step (*ca*. 200-325 °C, accompanied by an endothermic peak in the DSC trace, see inset) is in accordance with dehydroxylation temperatures found in previous FTIR spectroscopic studies.[11-13]

This incredibly good match with theory further demonstrates the near defect-free nature of UiO-66-Ideal. More importantly, it shows that our quantitative analysis of TGA data is solid, especially when one takes into account the vast additional evidence for the near ideality of the sample.[3]

3.4.3. Quantitative Analysis of Defective UiO-66 Samples: Our Previously Published Method

In the supporting information of a previous study,[3] we detailed a procedure for quantifying linker deficiencies in defective UiO-66 samples via TGA. In said samples, the defects were compensated by acetate, formate, difluoroacetate, or trifluoroacetate ligands, but none with benzoate ligands. Their TGA traces were all qualitatively similar, and a representative example (obtained on 100Form, a UiO-66 sample whose defects are compensated by formate ligands)[3] is shown below in **Figure S7**:

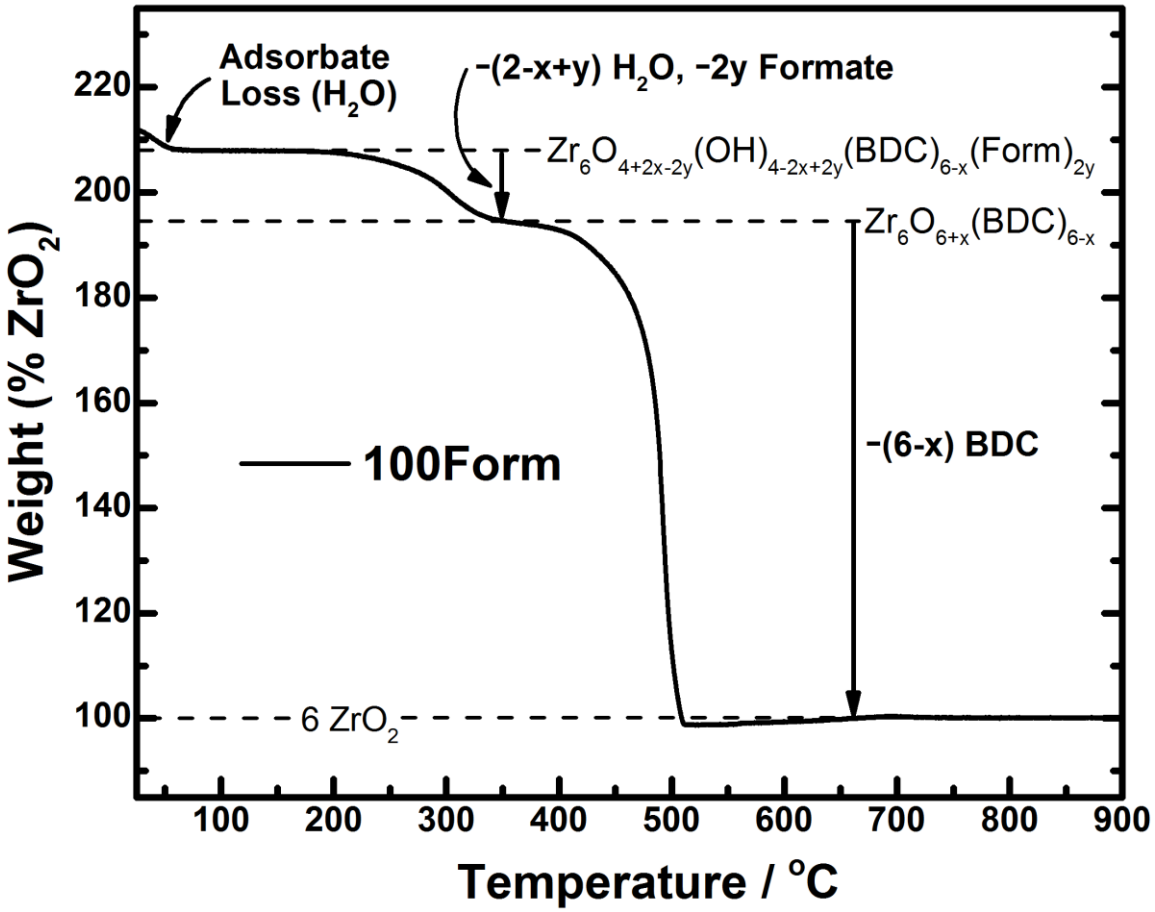

Figure S7. TGA trace (normalized such that end weight = 100 %) obtained on 100Form, a UiO-66 sample whose defects are compensated by formate (Form) ligands. The sample was synthesized and extensively characterized in a previous study.[3] The weight losses are assigned on the figure. For more information, see the accompanying discussion below.

As one can see in the figure, the TGA trace features three well resolved weight losses, assigned to the following processes:

1) The loss of adsorbed molecules (a.k.a. adsorbate volatilization). When H_2O is the only adsorbate (as is the case above and in the samples herein), then this step occurs over a temperature range of *ca*. 25-100 °C. Following this weight loss, the TGA trace reaches a plateau, spanning a temperature range of *ca*. 100-200 °C. For the duration of this plateau, the material is in the adsorbate-free ***hydroxylated*** form, complete with its defect-compensating ligands (in this case, formate). In the supporting information of our previous study,[3] we went a little further and proposed that the general composition of the material at this stage is $\mathbf{Zr_6O_{4+2x-2y}(OH)_{4-2x+2y}(BDC)_{6-x}(Mod)_{2y}}$, where **Mod** is a monocarboxylate defect compensating ligand (in this case formate, shortened to "Form" in the figure above).

2) The removal of the defect compensating ligands[3, 14, 15] (in this case, formate) ***and*** the dehydroxylation of the Zr_6 cornerstones[11-13, 16] (i.e. the loss of structural H_2O). These two weight loss events occur over a similar temperature range (*ca*. 200-350 °C) and are thus not well resolved from one another. Following these processes, the TGA trace reaches a second plateau where the material is in the ligand-free, ***dehydroxylated*** form, $\mathbf{Zr_6O_{6+x}(BDC)_{6-x}}$.

3) Framework decomposition.[3, 14, 15, 17] This is where the $(\mathbf{6-x})$ **BDC** linkers combust, leaving 6 molar equivalents of $\mathbf{ZrO_2}$ as the final product. From the (normalized) magnitude of this weight loss ($\boldsymbol{W_{Exp.Plat.} - W_{End}}$, see below), it is possible to calculate the number of linker deficiencies per Zr_6 formula unit, $\boldsymbol{x}$ (from the aforementioned general composition, $\mathbf{Zr_6O_{6+x}(BDC)_{6-x}}$) via the following equation (derived in the supporting information of our previous study)[3]:

$$\boldsymbol{x = 6 - \left(\frac{(W_{Exp.Plat.} - W_{End})}{Wt.PL_{Theo.}}\right)} \tag{22}$$

Where:

$\boldsymbol{W_{Exp.Plat.}}$ is the (normalized) weight of the sample at the 2nd TGA plateau (see above).

$\boldsymbol{W_{End}}$ is the end weight of the material (i.e. its weight at 900 °C in the TGA trace), which we normalize to 100 % as standard practice (see **Section 3.4.2**).

$\boldsymbol{Wt.PL_{Theo.}}$ is the theoretical (normalized) weight loss magnitude ***per BDC linker*** lost from the Zr_6 formula unit. This is calculated later in **Section 3.4.5.3**, where we show that $\boldsymbol{Wt.PL_{Theo.}}$ = **<u>20.03 %</u>** when $\boldsymbol{W_{End}}$ is normalized to 100 %.

From the above, one can see that $\boldsymbol{W_{Exp.Plat.}}$ is the only unknown required to calculate $\boldsymbol{x}$ when $\boldsymbol{W_{End}}$ is normalized to 100 %. Pinpointing the $\boldsymbol{W_{Exp.Plat.}}$ value is therefore the only part of the analysis which requires human input. An explanation of how the $\boldsymbol{W_{Exp.Plat.}}$ value is chosen can be found in the supporting information of our previous study,[3] as well as **Sections 3.4.5.2** and **3.4.7.2.1** herein. Foregoing this explanation for the sake of brevity, the $\boldsymbol{W_{Exp.Plat.}}$ value in the TGA trace shown in **Figure S7** (pinpointed by the second highest horizontal dashed line) is <u>194.6 %</u>, and thus the number of linker deficiencies per Zr_6 formula unit in the sample is:

$$\boldsymbol{x = 6 - \left(\frac{(194.6\,\% - 100\,\%)}{20.03\,\%}\right)}$$

$$\boldsymbol{x = \underline{1.28}}$$

To put this value into context, this means that the (average) composition of the sample at the 2nd TGA plateau is $\mathbf{Zr_6O_{(6+1.28)}(BDC)_{(6-1.28)}}$ = $\mathbf{Zr_6O_{7.28}(BDC)_{4.72}}$, meaning that there are only 4.72 x 2 = **<u>9.44</u>** BDC linkers coordinated to its average Zr_6 cluster, significantly less than the 12 linkers in defect free UiO-66. This demonstrates the high concentration of defects in the sample.

3.4.4. Explanation for why the Previously Published Method is Obsolete for Characterizing Defective UiO-66 Samples with Benzoate Ligands

To explain why our previously published method is obsolete for calculating the number of linker deficiencies in benzoate-containing UiO-66 samples, let us start by analyzing the TGA trace obtained on 50Benz, a sample which contains very large amount of benzoate ligands:

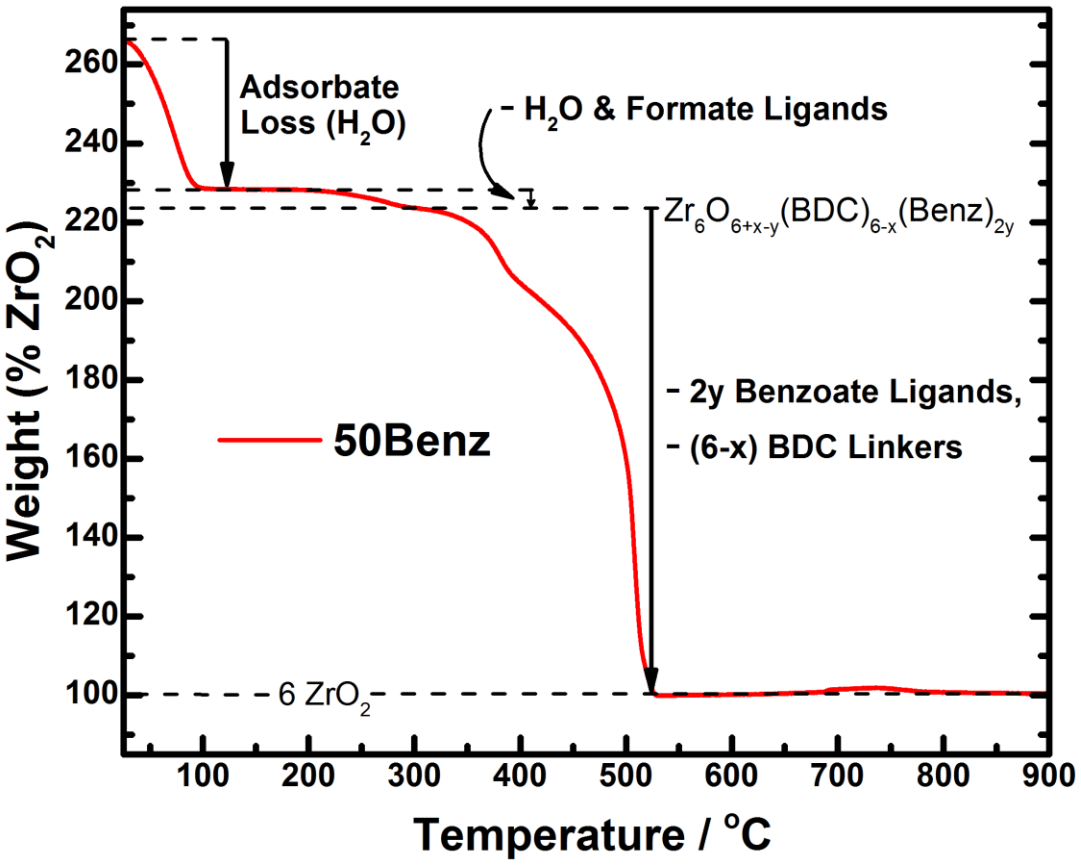

Figure S8. TGA trace (normalized such that end weight = 100 %) obtained on 50Benz, a defective UiO-66 sample with a very large amount of benzoate (Benz) ligands. The weight losses have been assigned on the figure. For more information, see the accompanying discussion below.

As one can see, the TGA trace features three ***well resolved*** weight losses, assigned to the following processes:

1) The loss of adsorbed molecules (a.k.a. adsorbate volatilization). When H_2O is the only adsorbate (as is the case in the samples herein), then this step occurs over a temperature range of *ca*. 25-100 °C. Following this weight loss, the TGA trace reaches a plateau, spanning a temperature range of *ca*. 100-200 °C. For the duration of this plateau, the material is in the adsorbate-free ***hydroxylated*** form, complete with its defect-compensating ligands. In the (non L-Serine functionalized) samples under investigation herein, the defects are compensated by a mixture of benzoate (**Benz**) and formate (**Form**) ligands, and thus we propose that the material is of composition $\mathbf{Zr_6O_{4+2x-2y-2z}(OH)_{4-2x+2y+2z}(BDC)_{6-x}(Benz)_{2y}(Form)_{2z}}$ at this stage. This general formula (which is too long to be legibly written on the above figure) was arrived at by the same method as that outlined in the supporting information of our previous paper,[3] and with the same restrictions on $\boldsymbol{x}$, $\boldsymbol{y}$, and $\boldsymbol{z}$.

2) The removal of ***thermally labile*** defect compensating ligands (e.g. formate,[3, 14] acetate,[4] difluoroacetate,[16] or trifluoroacetate[14, 15]) ***and*** the dehydroxylation of the Zr_6 cornerstones (i.e. the loss of structural H_2O). These two weight loss events usually occur over a similar temperature range (often 200-350 °C, with the exact range depending on the identity of the defect compensating ligand) and thus they are not well resolved from one another. In the samples under investigation herein, the formate ligands are lost at this stage, while the benzoate ligands (which we describe as ***thermally robust***) are not. Ultimately, this leaves our samples in the ***dehydroxylated*** form with defect compensating benzoate ligands, a state for which we propose a general composition of $\mathbf{Zr_6O_{6+x-y}(BDC)_{6-x}(Benz)_{2y}}$ (with the same $\boldsymbol{x}$ and $\boldsymbol{y}$ restrictions as those described in the supporting information of our previous study[3]).

3) The removal of benzoate ligands ***and*** the combustion of BDC linkers (framework decomposition[3, 14, 15, 17]), leaving 6 molar equivalents of ZrO_2 as the final product. The removal of benzoate ligands is a very gradual process which begins at *ca*. 290 °C but is still incomplete by the time the BDC linkers begin to combust at *ca*. 400 °C, meaning that the two weight loss events are not well resolved from one another. This makes it impossible to calculate the number of linker deficiencies per Zr_6 formula unit (i.e. the value of $\boldsymbol{x}$ in the aforementioned composition, $\mathbf{Zr_6O_{6+x-y}(BDC)_{6-x}(Benz)_{2y}}$) with our previously published method (see **Section 3.4.3**), which relies on the assumption that the final weight loss is ***solely due to*** the loss of $(\mathbf{6-x})$ BDC linkers. An alternative method of analysis is therefore required for analyzing defective UiO-66 samples with benzoate ligands.

To summarize the problem, consider **Figure S9** and its caption, in which the TGA results obtained on a defective UiO-66 sample with benzoate ligands (right plot) is compared with those obtained on a defective UiO-66 samples without benzoate ligands (left plot):

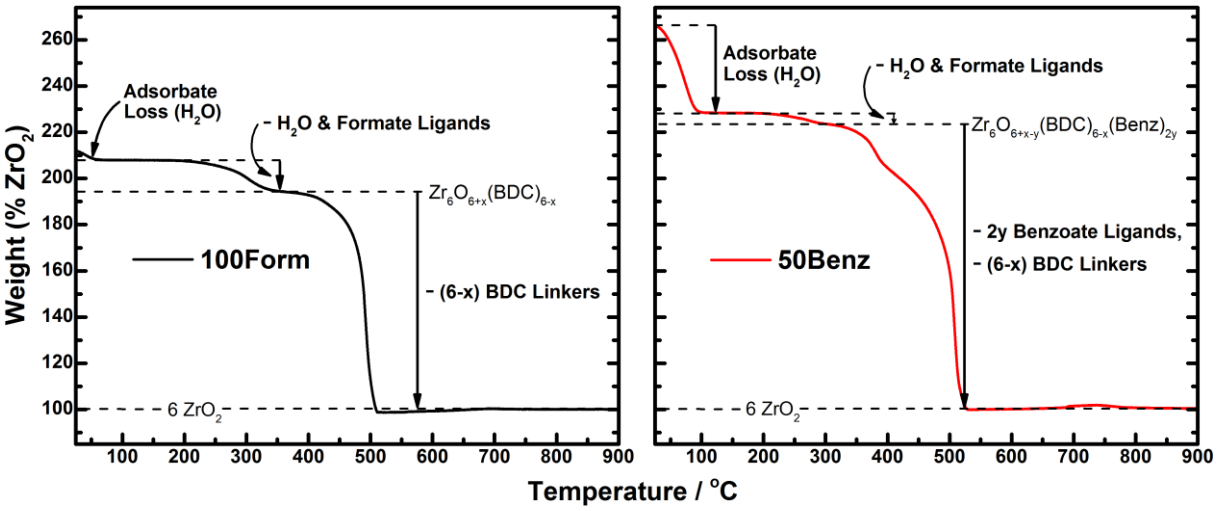

Figure S9. Typical examples of TGA traces obtained on left: a defective UiO-66 sample without benzoate ligands (100Form from our previous study),[3] right: a defective sample with a large amount of benzoate ligands (50Benz from the current study). Data has been normalized such that the end weight = 100 %. The same y-scale is adopted in both plots. As can be seen, the final weight loss of the UiO-66 sample without benzoate ligands is purely due to the loss of $(\mathbf{6-x})$ **BDC** linkers (per Zr_6 formula unit), while the benzoate containing sample loses **2y benzoate** ligands (per Zr_6 formula unit) in addition. This makes it impossible to calculate the number of linker deficiencies per Zr_6 formula unit (i.e. the value of **x**) with our previously published method (see **Section 3.4.3**), which relies on the assumption that the final weight loss is ***solely due to*** the loss of $(\mathbf{6-x})$ **BDC** linkers.

3.4.5. Deriving our Method for Determining the Number of Linker Deficiencies in Defective UiO-66 Samples with Benzoate Ligands

Table of Contents

3.4.5.1. Introduction

As explained in **Section 3.4.4**, our previously published method cannot be used to determine the number of linker deficiencies in benzoate-containing defective UiO-66 samples. We have therefore developed a new, more general method which circumvents the failings of its predecessor by utilizing quantitative data from both TGA and dissolution/^{1}H NMR results.

Let us recall from **Section 3.4.4** that the general composition of a defective UiO-66 sample with benzoate ligands is $\mathbf{Zr_6O_{6+x-y}(BDC)_{6-x}(Benz)_{2y}}$ before the final resolvable weight loss in its TGA trace. As is clear from the title of this section, our goal is to calculate the number of linker deficiencies per Zr_6 formula unit in any given sample, which is the value of $\boldsymbol{x}$ in the aforementioned composition.

To do so, we must deconvolute the individual contributions that benzoate and BDC each make to the magnitude of the final TGA weight loss. To this end, 4 key pieces of information are required:

1) The benzoate/BDC molar ratio $\left(\frac{\mathbf{Benz.}}{\mathbf{BDC}}\mathbf{m}_{\boldsymbol{R}}\right)$ in the sample. This can be reliably determined by dissolution/^{1}H NMR, as discussed in **Section 3.3**.

2) The magnitude of the final weight loss $\left(\boldsymbol{Wt.Loss_{Exp.}}\right)$ in the TGA trace obtained on the sample.

3) The theoretical weight loss magnitude ***per BDC linker lost*** from the Zr_6 formula unit ($\boldsymbol{Wt.PL_{Theo.}}$). This value depends solely on the TGA normalization method and is not influenced by the specific sample under investigation.

4) The theoretical weight loss magnitude ***per benzoate ligand lost*** from the Zr_6 formula unit ($\boldsymbol{Wt.PB_{Theo.}}$). This value depends solely on the TGA normalization method and is not influenced by the specific sample under investigation.

The following 3 subsections demonstrate how the latter 3 values ($\boldsymbol{Wt.Loss_{Exp.}}$, $\boldsymbol{Wt.PL_{Theo.}}$, and $\boldsymbol{Wt.PB_{Theo.}}$) are calculated, while the method used to calculate $\frac{\mathbf{Benz.}}{\mathbf{BDC}}\mathbf{m}_{\boldsymbol{R}}$ is thoroughly outlined in **Section 3.3**.

3.4.5.2. Determining the Magnitude of the Final Weight Loss in the TGA Trace $(\boldsymbol{Wt.Loss_{Exp.}})$

The calculation of $\boldsymbol{Wt.Loss_{Exp.}}$ is best explained by example. To this end, the TGA-DSC results obtained on 50Benz are shown in **Figure S10** below:

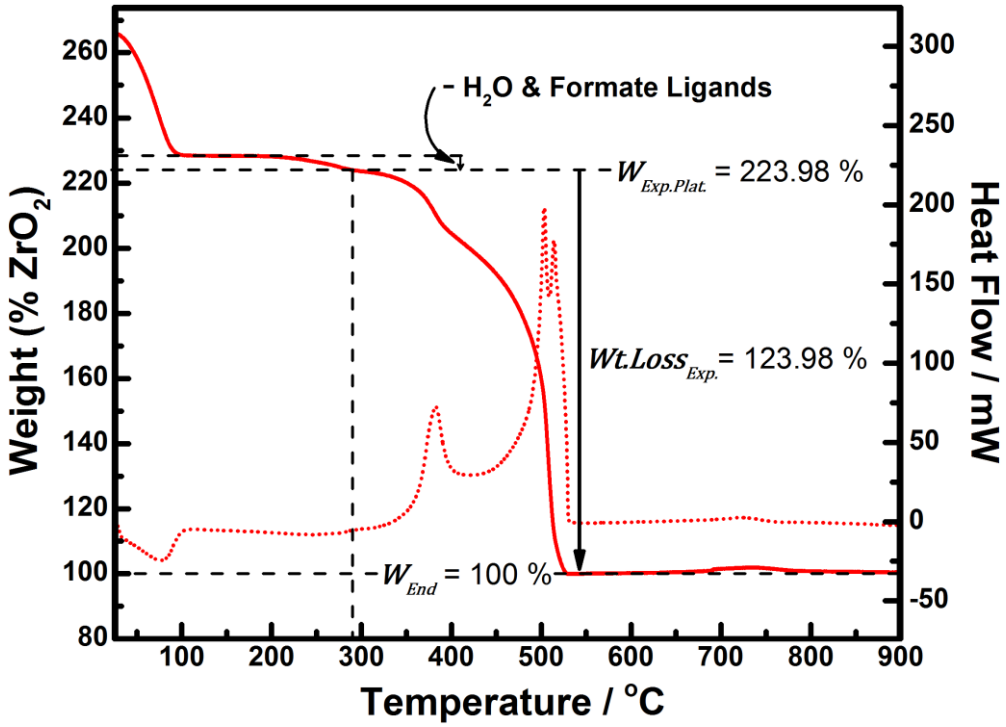

Figure S10. Calculation of $\boldsymbol{Wt.Loss_{Exp.}}$ from the TGA-DSC results obtained on 50Benz. Solid curve, left axis - TGA trace (normalized such that end weight $(\boldsymbol{W_{End}})$ = 100 %). Dotted curve, right axis – DSC signal.

As can be seen, $\boldsymbol{Wt.Loss_{Exp.}}$ is simply the weight difference between $\boldsymbol{W_{Exp.Plat.}}$ and $\boldsymbol{W_{End}}$, where $\boldsymbol{W_{Exp.Plat.}}$ is the experimentally measured TGA plateau after dehydroxylation and formate loss (see **Section 3.4.4**), and $\boldsymbol{W_{End}}$ is the end weight of the material (i.e. its weight at 900 °C in the TGA trace):

$$\boldsymbol{Wt.Loss_{Exp.}} = \boldsymbol{W_{Exp.Plat.}} - \boldsymbol{W_{End}} \tag{23}$$

As mentioned throughout this section, we normalize $\boldsymbol{W_{End}}$ to 100 % as standard practice, meaning that only the $\boldsymbol{W_{Exp.Plat.}}$ value is needed to calculate $\boldsymbol{Wt.Loss_{Exp.}}$. Choosing the correct $\boldsymbol{W_{Exp.Plat.}}$ value is critical to accurate analysis and requires one to pinpoint the temperature at which all dehydroxylation and formate loss is complete. This is not completely straightforward since the final weight loss often commences very shortly thereafter. Nevertheless, we use the DSC trace as a guide, noting that a sharp exothermic peak begins to emerge at the onset of the final weight loss. It is the temperature immediately preceding the emergence of this exothermic peak (in this case 290 °C, as highlighted by the vertical dashed line on the above figure) that is chosen as the plateau temperature. The $\boldsymbol{W_{Exp.Plat.}}$ value is simply the (normalized) sample weight at this temperature (= 223.98 % in this case, as shown in the figure). Inserting this value into **Equation (23)** yields a $\boldsymbol{Wt.Loss_{Exp.}}$ value of **123.98 %**, as also shown in the figure. It should be noted that the choice of $\boldsymbol{W_{Exp.Plat.}}$ was much simpler in 50Benz-HA, whose TGA trace features a clearer plateau after dehydroxylation and formate loss, as demonstrated in **Section 3.4.7.2.1**.

3.4.5.3. Deriving the Theoretical Weight Loss Magnitude per BDC Linker Lost from the Zr_6 formula Unit ($\boldsymbol{Wt.PL_{Theo.}}$)

The theoretical weight loss magnitude ***per BDC linker lost*** from the Zr_6 formula unit ($\boldsymbol{Wt.PL_{Theo.}}$) is calculated by taking the difference between the theoretical TGA plateau of ***ideal dehydroxylated*** UiO-66 ($\boldsymbol{W_{Ideal.Plat.}}$) and the end weight of the TGA run ($\boldsymbol{W_{End}}$), and dividing by the ***ideal*** number of linkers in UiO-66's Zr_6 formula unit, $\boldsymbol{NL_{Ideal.}}$:

$$\boldsymbol{Wt.PL_{Theo.}} = \frac{(\boldsymbol{W_{Ideal.Plat.}} - \boldsymbol{W_{End}})}{\boldsymbol{NL_{Ideal.}}} \quad (24)$$

As demonstrated in **Section 3.4.2**, $\boldsymbol{W_{Ideal.Plat.}}$ is equal to **220.2 %** when $\boldsymbol{W_{End}}$ is normalized to **100 %** (which we do as standard practice), while the ideal number of linkers in the UiO-66's Zr_6 formula unit is **6** ($\mathbf{Zr_6O_6(BDC)_{\underline{6}}}$ = **<u>6</u>** BDC linkers). Inserting these values into **Equation (24)** allows $\boldsymbol{Wt.PL_{Theo.}}$ to be calculated:

$$\boldsymbol{Wt.PL_{Theo.}} = \frac{(\mathbf{220.2}\ \% - \mathbf{100}\ \%)}{\mathbf{6}}$$

$$= \underline{\mathbf{20.03}}\ \%$$

<u>Note</u>: this value is not influenced by the specific sample under investigation and would only be affected if an alternative method of TGA normalization were to be employed.

3.4.5.4. Deriving the Theoretical Weight Loss Magnitude per Benzoate Ligand Lost from the Zr_6 formula Unit ($Wt.PB_{Theo.}$)

The theoretical weight loss magnitude ***per benzoate ligand lost*** from the Zr_6 formula unit ($Wt.PB_{Theo.}$) is calculated in an analogous manner to $Wt.PL_{Theo.}$ (see previous subsection). First, we must calculate the theoretical TGA plateau ($W_{Theo.Plat.}$) of a hypothetical compound with a composition of $\mathbf{Zr_6O_6(Benz.)_{12}}$, where **Benz.** is benzoate. This is achieved via **Equation (21)**, first presented in **Section 3.4.2**:

$$W_{Theo.Plat.} = \left(\frac{M_{Comp.}}{M_{6\,ZrO_2}}\right) \cdot W_{End} \qquad (21)$$

As mentioned throughout this section, we normalize the end weight of our TGA experiments (W_{End}) to 100 % as standard practice, while the molar mass of 6 moles of ZrO_2 ($M_{6\,ZrO_2}$) is **739.34 g mol^{-1}**. This leaves $M_{Comp.}$, the molar mass of the composition of interest (in this case $\mathbf{Zr_6O_6(Benz)_{12}}$) as the only unknown. The molar mass of $\mathbf{Zr_6O_6(Benz)_{12}}$ is **2096.70 g mol^{-1}**, and thus its theoretical TGA plateau is:

$$W_{Theo.Plat.} = \left(\frac{\mathbf{2096.70\ g\ mol^{-1}}}{\mathbf{739.34\ g\ mol^{-1}}}\right) \cdot \mathbf{100}\ \%$$

$$= \underline{\mathbf{283.59}\ \%}$$

The theoretical weight loss magnitude ***per benzoate ligand lost*** from the Zr_6 formula unit ($Wt.PB_{Theo.}$) can then be calculated by taking the difference between this $W_{Theo.Plat.}$ value and the end weight of the TGA run (W_{End}), and dividing by NB, the number of benzoate ligands in the hypothetical composition (per Zr_6 formula unit):

$$Wt.PB_{Theo.} = \frac{(W_{Theo.Plat.} - W_{End})}{NB} \qquad (25)$$

As discussed/calculated above, the $W_{Theo.Plat.}$ and W_{End} values are $\mathbf{283.59}$ and $\mathbf{100}$ %, respectively, while the number of benzoate ligands in the hypothetical composition (per Zr_6 formula unit) is **12** ($\mathbf{Zr_6O_6(Benz)_{\underline{12}}}$ = **12** benzoate ligands). Inserting these values into **Equation (25)** allows $Wt.PB_{Theo.}$ to be calculated:

$$Wt.PB_{Theo.} = \frac{(\mathbf{283.59}\ \% - \mathbf{100}\ \%)}{\mathbf{12}}$$

$$= \underline{\mathbf{15.30}}\ \%$$

Note: this value is not influenced by the specific sample under investigation and would only be affected if an alternative method of TGA normalization were to be employed.

3.4.5.5. Final Derivation of the Equation for x, the Number of Linker Deficiencies per Zr_6 Formula Unit

As discussed in **Section 3.4.4**, the final weight loss in TGA traces obtained on defective UiO-66 samples with benzoate ligands involves the loss of $(\mathbf{6}-\boldsymbol{x})$ BDC linkers and $\mathbf{2}\boldsymbol{y}$ benzoate ligands per Zr_6 formula unit. Each BDC linker in the Zr_6 formula unit contributes a (normalized) weight loss of $\boldsymbol{Wt.PL_{Theo.}}$ (= 20.03 %, as calculated in **Section 3.4.5.3**). Since $(\mathbf{6}-\boldsymbol{x})$ BDC linkers (per Zr_6 formula unit) are lost during the final weight loss, their total contribution to its magnitude is $(\mathbf{6}-\boldsymbol{x})\cdot\boldsymbol{Wt.PL_{Theo.}}$.

Similarly, each benzoate ligand in the Zr_6 formula unit contributes a (normalized) weight loss of $\boldsymbol{Wt.PB_{Theo.}}$ (= 15.30 %, as calculated in **Section 3.4.5.4**). Since $\mathbf{2}\boldsymbol{y}$ benzoate ligands (per Zr_6 formula unit) are lost during the final weight loss, their total contribution to its magnitude is $\mathbf{2}\boldsymbol{y}\cdot\boldsymbol{Wt.PB_{Theo.}}$.

The total magnitude of the final TGA weight loss ($\boldsymbol{Wt.Loss_{Exp.}}$, calculated by the method outlined in **Section 3.4.5.2**) is equal to the sum of the weight loss contributions made by BDC and benzoate:

$$\boldsymbol{Wt.Loss_{Exp.}} = \left((\mathbf{6}-\boldsymbol{x})\cdot\boldsymbol{Wt.PL_{Theo.}}\right) + \left(\mathbf{2}\boldsymbol{y}\cdot\boldsymbol{Wt.PB_{Theo.}}\right) \tag{26}$$

Now let us recall from **Section 3.4.4** that the general composition of a defective UiO-66 sample with benzoate ligands, after dehydroxylation and formate loss, is:

$$\mathbf{Zr_6O_{6+x-y}(BDC)_{6-x}(Benz)_{2y}}$$

In this composition, one can see that the molar ratio between **Benz** (benzoate) and **BDC**, $\frac{\mathbf{Benz.}}{\mathbf{BDC}}\mathbf{m_R}$ is:

$$\frac{\mathbf{Benz.}}{\mathbf{BDC}}\mathbf{m_R} = \frac{\mathbf{2}\boldsymbol{y}}{(\mathbf{6}-\boldsymbol{x})} \tag{27}$$

This equation can then be solved for $\mathbf{2}\boldsymbol{y}$:

$$\mathbf{2}\boldsymbol{y} = (\mathbf{6}-\boldsymbol{x})\cdot\frac{\mathbf{Benz.}}{\mathbf{BDC}}\mathbf{m_R} \tag{28}$$

Which can be substituted into **Equation (26)** to generate **Equation (29)**:

$$\boldsymbol{Wt.Loss_{Exp.}} = \left((\mathbf{6}-\boldsymbol{x})\cdot \boldsymbol{Wt.PL_{Theo.}}\right) + \left(\mathbf{2}\boldsymbol{y}\cdot \boldsymbol{Wt.PB_{Theo.}}\right) \tag{26}$$

$$\boldsymbol{Wt.Loss_{Exp.}} = \left((\mathbf{6}-\boldsymbol{x})\cdot \boldsymbol{Wt.PL_{Theo.}}\right) + \left(\left((\mathbf{6}-\boldsymbol{x})\cdot \frac{\mathbf{Benz.}}{\mathbf{BDC}}\mathbf{m_R}\right)\cdot \boldsymbol{Wt.PB_{Theo.}}\right) \tag{29}$$

Taking out a common factor of $(\mathbf{6}-\boldsymbol{x})$ on the right hand side:

$$\boldsymbol{Wt.Loss_{Exp.}} = (\mathbf{6}-\boldsymbol{x})\cdot\left(\boldsymbol{Wt.PL_{Theo.}} + \left(\frac{\mathbf{Benz.}}{\mathbf{BDC}}\mathbf{m_R}\cdot \boldsymbol{Wt.PB_{Theo.}}\right)\right) \tag{30}$$

Solving for $(\mathbf{6}-\boldsymbol{x})$:

$$(\mathbf{6}-\boldsymbol{x}) = \left(\frac{\boldsymbol{Wt.Loss_{Exp.}}}{\left(\boldsymbol{Wt.PL_{Theo.}} + \left(\frac{\mathbf{Benz.}}{\mathbf{BDC}}\mathbf{m_R}\cdot \boldsymbol{Wt.PB_{Theo.}}\right)\right)}\right) \tag{31}$$

And finally, for $\boldsymbol{x}$:

$$\boldsymbol{x} = \mathbf{6} - \left(\frac{\boldsymbol{Wt.Loss_{Exp.}}}{\left(\boldsymbol{Wt.PL_{Theo.}} + \left(\frac{\mathbf{Benz.}}{\mathbf{BDC}}\mathbf{m_R}\cdot \boldsymbol{Wt.PB_{Theo.}}\right)\right)}\right) \tag{32}$$

Where $\boldsymbol{Wt.Loss_{Exp.}}$, $\boldsymbol{Wt.PL_{Theo.}}$, $\frac{\mathbf{Benz.}}{\mathbf{BDC}}\mathbf{m_R}$, and $\boldsymbol{Wt.PB_{Theo.}}$ are determined by the methods outlined in **Sections 3.4.5.2**, **3.4.5.3**, **3.3**, and **3.4.5.4**, respectively.

Note: **Equation (32)** is generally applicable, even to samples without benzoate ligands. Such samples have a benzoate/BDC ratio $\left(\frac{\mathbf{Benz.}}{\mathbf{BDC}}\mathbf{m_R}\right)$ of 0, which effectively transforms **Equation (32)** into the **Equation (22)** (see **Section 3.4.3**), meaning that $\boldsymbol{x}$ can still be calculated.

3.4.6. Extending the Method to Attain Estimates for the Full Composition of Our Samples

Table of Contents

3.4.6.1. Introduction

As originally proposed in **Section 3.4.4**, the general (hydroxylated) composition of our (non L-Serine functionalized) UiO-66 samples is:

$$\mathbf{Zr_6O_{4+2x-2y-2z}(OH)_{4-2x+2y+2z}(BDC)_{6-x}(Benz)_{2y}(Form)_{2z}}$$

Where **Benz** is benzoate and **Form** is formate.

After dehydroxylation and formate loss (the 2nd TGA weight loss step, see **Section 3.4.4**), this composition becomes:

$$\mathbf{Zr_6O_{6+x-y}(BDC)_{6-x}(Benz)_{2y}}$$

From the above general formulae, one can see that calculating the values of $\boldsymbol{x}$, $\boldsymbol{y}$, and $\boldsymbol{z}$ in our samples will allow us to attain their full composition at two different stages in their TGA traces. The equation for $\boldsymbol{x}$ (**Equation (32)**) was derived in **Section 3.4.5.5**, leaving $\boldsymbol{y}$, and $\boldsymbol{z}$ as the remaining unknowns. The following 2 subsections are dedicated to deriving equations for these two values.

3.4.6.2. Deriving the Equation for $2y$, the Number of Benzoate Ligands per Zr_6 Formula Unit

The equation for $\mathbf{2}\boldsymbol{y}$ is derived in essentially the same manner as the equation for $\boldsymbol{x}$ (see **Section 3.4.5.5**). Let us start by revisiting **Equation (27)** (originally presented in **Section 3.4.5.5**):

$$\frac{\mathbf{Benz.}}{\mathbf{BDC}}\mathbf{m_R} = \frac{\mathbf{2}\boldsymbol{y}}{(\mathbf{6}-\boldsymbol{x})} \tag{27}$$

Solving this equation for $(\mathbf{6}-\boldsymbol{x})$ yields **Equation (33)**:

$$(\mathbf{6}-\boldsymbol{x}) = \mathbf{2}\boldsymbol{y}\cdot\left(\frac{\mathbf{Benz.}}{\mathbf{BDC}}\mathbf{m_R}\right)^{-\mathbf{1}} \tag{33}$$

Which we can then substitute into **Equation (26)** (see **Section 3.4.5.5**) to obtain **Equation (34)**:

$$\boldsymbol{Wt.Loss_{Exp.}} = \left((\mathbf{6}-\boldsymbol{x})\cdot\boldsymbol{Wt.PL_{Theo.}}\right) + \left(\mathbf{2}\boldsymbol{y}\cdot\boldsymbol{Wt.PB_{Theo.}}\right) \tag{26}$$

$$\boldsymbol{Wt.Loss_{Exp.}} = \left(\left(\mathbf{2}\boldsymbol{y}\cdot\left(\frac{\mathbf{Benz.}}{\mathbf{BDC}}\mathbf{m_R}\right)^{-\mathbf{1}}\right)\cdot\boldsymbol{Wt.PL_{Theo.}}\right) + \left(\mathbf{2}\boldsymbol{y}\cdot\boldsymbol{Wt.PB_{Theo.}}\right) \tag{34}$$

Taking out a common factor of $\mathbf{2}\boldsymbol{y}$ on the right hand side gives us:

$$\boldsymbol{Wt.Loss_{Exp.}} = \mathbf{2}\boldsymbol{y}\cdot\left(\left(\left(\frac{\mathbf{Benz.}}{\mathbf{BDC}}\mathbf{m_R}\right)^{-\mathbf{1}}\cdot\boldsymbol{Wt.PL_{Theo.}}\right) + \boldsymbol{Wt.PB_{Theo.}}\right) \tag{35}$$

Finally, solving for $\mathbf{2}\boldsymbol{y}$:

$$\mathbf{2}\boldsymbol{y} = \left(\frac{\boldsymbol{Wt.Loss_{Exp.}}}{\left(\left(\frac{\mathbf{Benz.}}{\mathbf{BDC}}\mathbf{m_R}\right)^{-\mathbf{1}}\cdot\boldsymbol{Wt.PL_{Theo.}}\right) + \boldsymbol{Wt.PB_{Theo.}}}\right) \tag{36}$$

Where $\boldsymbol{Wt.Loss_{Exp.}}$, $\boldsymbol{Wt.PL_{Theo.}}$, $\frac{\mathbf{Benz.}}{\mathbf{BDC}}\mathbf{m_R}$, and $\boldsymbol{Wt.PB_{Theo.}}$ are determined by the methods outlined in **Sections 3.4.5.2**, **3.4.5.3**, **3.3**, and **3.4.5.4**, respectively. Obviously, $\boldsymbol{y}$ is calculated by dividing $\mathbf{2}\boldsymbol{y}$ by 2.

3.4.6.3. Deriving the Equation for $2z$, the Number of Formate Ligands per Zr_6 Formula Unit

Let us recall from **Section 3.4.4** that the general composition of our (non L-Serine functionalized) UiO-66 samples in their hydroxylated form is:

$$\mathbf{Zr_6O_{4+2x-2y-2z}(OH)_{4-2x+2y+2z}(BDC)_{6-x}(Benz)_{2y}(Form)_{2z}}$$

In the above composition, one can see that the molar ratio between **Form** (formate) and **BDC**, $\left(\frac{\mathbf{Form.}}{\mathbf{BDC}}\mathbf{m_R}\right)$ is:

$$\frac{\mathbf{Form.}}{\mathbf{BDC}}\mathbf{m_R} = \frac{\mathbf{2}\boldsymbol{z}}{(\mathbf{6}-\boldsymbol{x})} \tag{37}$$

Which can easily be solved for $\mathbf{2}\boldsymbol{z}$:

$$\mathbf{2}\boldsymbol{z} = (\mathbf{6}-\boldsymbol{x}) \cdot \frac{\mathbf{Form.}}{\mathbf{BDC}}\mathbf{m_R} \tag{38}$$

Where $\frac{\mathbf{Form.}}{\mathbf{BDC}}\mathbf{m_R}$ and $\boldsymbol{x}$ are determined by the methods outlined in **Sections 3.3** and **3.4.5.5**, respectively. Obviously, $\boldsymbol{z}$ is calculated by dividing $\mathbf{2}\boldsymbol{z}$ by 2.

3.4.7. Example Composition Calculations

Table of Contents

3.4.7.1. 50Benz

Table of Contents

3.4.7.1.1. Calculating the Values of x, y, and z

Upon inspection of the equations for $\boldsymbol{x}$, $\boldsymbol{y}$, and $\boldsymbol{z}$ (**Equations (32)**, **(36)**, and **(38)**, respectively) one can see that 5 input values ($\boldsymbol{Wt.Loss_{Exp.}}$, $\boldsymbol{Wt.PL_{Theo.}}$, $\boldsymbol{Wt.PB_{Theo.}}$, $\frac{\textbf{Benz.}}{\textbf{BDC}}\mathbf{m_R}$, and $\frac{\textbf{Form.}}{\textbf{BDC}}\mathbf{m_R}$) are required for their calculation.

However, two of these input values ($\boldsymbol{Wt.PL_{Theo.}}$ and $\boldsymbol{Wt.PB_{Theo.}}$) are automatically known ($\boldsymbol{Wt.PL_{Theo.}}$ = 20.03 %, $\boldsymbol{Wt.PB_{Theo.}}$ = 15.30 %) when TGA data is normalized by setting the end weight to 100 %, as we do herein (see **Sections 3.4.5.3** and **3.4.5.4** for relevant calculations).

Furthermore, the $\boldsymbol{Wt.Loss_{Exp.}}$ value of 50Benz (= 123.98 %) was calculated in **Section 3.4.5.2**, leaving $\frac{\textbf{Benz.}}{\textbf{BDC}}\mathbf{m_R}$, and $\frac{\textbf{Form.}}{\textbf{BDC}}\mathbf{m_R}$ as the remaining unknowns. Fortunately, both of these inputs can be determined by dissolution/^{1}H NMR spectroscopy (see **Section 3.3** for details of the method), and the following values were obtained from the spectrum acquired on 50Benz:

$$\frac{\textbf{Benz.}}{\textbf{BDC}}\mathbf{m_R} = \underline{\mathbf{0.78}}$$

$$\frac{\textbf{Form.}}{\textbf{BDC}}\mathbf{m_R} = \underline{\mathbf{0.01}}$$

These values are also presented later in **Table S3** (see **Section 4.2.1**), along with the numerical values of the ^{1}H NMR integrals relevant to their calculation. The spectrum from which these values were obtained is presented in **Figure 2** in the main article (black curves).

Returning to the task at hand, all 5 input values are now known, meaning that $\boldsymbol{x}$, $\boldsymbol{y}$, and $\boldsymbol{z}$ can be calculated with **Equations (32)**, **(36)** and **(38)**, respectively:

$$\boldsymbol{x} = \mathbf{6} - \left(\frac{\boldsymbol{Wt.Loss_{Exp.}}}{\left(\boldsymbol{Wt.PL_{Theo.}} + \left(\frac{\textbf{Benz.}}{\textbf{BDC}}\mathbf{m_R} \cdot \boldsymbol{Wt.PB_{Theo.}} \right) \right)} \right) \tag{32}$$

$$\boldsymbol{x} = \mathbf{6} - \left(\frac{\mathbf{123.98\ \%}}{\left(\mathbf{20.03\ \%} + \left(\mathbf{0.78} \cdot \mathbf{15.30\ \%} \right) \right)} \right)$$

$$\boldsymbol{x} = \underline{\mathbf{2.12}}$$

$$\mathbf{2}\boldsymbol{y} = \left(\frac{\boldsymbol{Wt.Loss_{Exp.}}}{\left(\left(\frac{\mathbf{Benz.}}{\mathbf{BDC}} \mathbf{m_R} \right)^{-1} \cdot \boldsymbol{Wt.PL_{Theo.}} \right) + \boldsymbol{Wt.PB_{Theo.}}} \right) \tag{36}$$

$$\mathbf{2}\boldsymbol{y} = \left(\frac{\mathbf{123.98}\ \%}{\left((\mathbf{0.78})^{-1} \cdot \mathbf{20.03}\ \% \right) + \mathbf{15.30}\ \%} \right)$$

$$\mathbf{2}\boldsymbol{y} = \mathbf{3.03}$$

$$\boldsymbol{y} = \underline{\mathbf{1.52}}$$

$$\mathbf{2}\boldsymbol{z} = (\mathbf{6} - \boldsymbol{x}) \cdot \frac{\mathbf{Form.}}{\mathbf{BDC}} \mathbf{m_R} \tag{38}$$

$$\mathbf{2}\boldsymbol{z} = (\mathbf{6} - \mathbf{2.12}) \cdot \mathbf{0.01}$$

$$\mathbf{2}\boldsymbol{z} = \mathbf{0.04}$$

$$\boldsymbol{z} = \underline{\mathbf{0.02}}$$

Note: all input values were rounded to 2 decimal places before being used to calculate $\boldsymbol{x}$, $\boldsymbol{y}$, and $\boldsymbol{z}$. This resulted in a very slight inaccuracy in the $\boldsymbol{y}$ value obtained. When more accurate input values were instead used, the $\boldsymbol{y}$ value became **1.51**, which is the value we will use hereafter.

3.4.7.1.2. Entering the x, y, & z Values into General Formulae to Obtain Full Compositions

Let us recall from **Section 3.4.4** that the general composition of our (non L-Serine functionalized) UiO-66 samples in their hydroxylated form is:

$$\mathbf{Zr_6O_{4+2x-2y-2z}(OH)_{4-2x+2y+2z}(BDC)_{6-x}(Benz)_{2y}(Form)_{2z}}$$

After dehydroxylation and formate loss (the 2nd TGA weight loss step, see **Section 3.4.4**), this composition becomes:

$$\mathbf{Zr_6O_{6+x-y}(BDC)_{6-x}(Benz)_{2y}}$$

With the x, y, and z values now known (= 2.12, 1.51, and 0.02, respectively, see previous subsection), they can be entered into the above general formulae to obtain the full composition of 50Benz at both stages in its TGA trace. Starting with the hydroxylated composition:

$$\mathbf{Zr_6O_{4+2\cdot(2.12)-2\cdot(1.51)-2\cdot(0.02)}(OH)_{4-2\cdot(2.12)+2\cdot(1.51)+2\cdot(0.02)}(BDC)_{6-2.12}(Benz)_{2\cdot(1.51)}(Form)_{2\cdot(0.02)}}$$

$$\mathbf{= Zr_6O_{5.18}(OH)_{2.82}(BDC)_{3.88}(Benz)_{3.02}(Form)_{0.04}}$$

Which becomes the following after dehydroxylation and formate loss:

$$\mathbf{Zr_6O_{6+2.12-1.51}(BDC)_{6-2.12}(Benz)_{2\cdot(1.51)}}$$

$$\mathbf{= Zr_6O_{6.61}(BDC)_{3.88}(Benz)_{3.02}}$$

3.4.7.1.3. Checking the Validity of the Calculated Compositions

In order to test the validity of our calculated compositions, we check that:

1) The compositions are charge neutral. Both of the compositions calculated in the previous subsection pass this test.

2) The molar ratios between the organic components in the compositions match with those obtained by dissolution/^{1}H NMR:

   In both of the compositions calculated in the previous subsection, the molar ratio between benzoate (**Benz**) and **BDC** is $\frac{3.02}{3.88} = \underline{\mathbf{0.78}}$, which is indeed the same value as that obtained by dissolution/^{1}H NMR (see **Section 3.4.7.1.1**).

   Moreover, the molar ratio between formate (**Form**) and **BDC** in the hydroxylated composition is $\frac{0.04}{3.88} = \underline{\mathbf{0.01}}$, which is indeed the same value as that obtained by dissolution/^{1}H NMR (see **Section 3.4.7.1.1**).

3) The theoretical TGA plateaus of the calculated compositions match well with those experimentally observed. To check this, we must first calculate the molar masses of our two compositions:

$$\mathbf{M\ Zr_6O_{6.61}(BDC)_{3.88}(Benz)_{3.02}} = \underline{\mathbf{1655.63}}\ \mathrm{g \cdot mol^{-1}}$$

and:

$$\mathbf{M\ Zr_6O_{5.18}(OH)_{2.82}(BDC)_{3.88}(Benz)_{3.02}(Form)_{0.04}} = \underline{\mathbf{1682.51}}\ \mathrm{g \cdot mol^{-1}}$$

We then obtain the theoretical TGA plateaus by entering these molar masses into **Equation (21)** (see **Section 3.4.2**):

$$\boldsymbol{W_{Theo.Plat.}} = \left(\frac{\boldsymbol{M_{Comp.}}}{\boldsymbol{M_{6\ ZrO_2}}}\right) \cdot \boldsymbol{W_{End}} \qquad (21)$$

$$\boldsymbol{W_{Theo.Plat.}} = \left(\frac{\mathbf{1655.63\ g \cdot mol^{-1}}}{\mathbf{739.34\ g \cdot mol^{-1}}}\right) \cdot \mathbf{100}\ \% = \underline{\mathbf{223.93}}\ \%$$

and:

$$\boldsymbol{W_{Theo.Plat.}} = \left(\frac{\mathbf{1682.51\ g \cdot mol^{-1}}}{\mathbf{739.34\ g \cdot mol^{-1}}}\right) \cdot \mathbf{100}\ \% = \underline{\mathbf{227.57}}\ \%$$

Simply from the value of its theoretical plateau, it is possible to scrutinize the validity of the composition after dehydroxylation and formate loss (in this case, $\mathbf{Zr_6O_{6.61}(BDC)_{3.88}(Benz)_{3.02}}$). Specifically, it should be equal to the experimental TGA plateau weight ($\boldsymbol{W_{Exp.Plat.}}$) originally entered into **Equation (23)** to calculate $\boldsymbol{Wt.Loss_{Exp.}}$ (see **Section 3.4.5.2**). In this case, the $\boldsymbol{W_{Exp.Plat.}}$ value was 223.98 % (see **Section 3.4.5.2**), which is extremely close to the theoretical value ($\boldsymbol{W_{Theo.Plat.}}$) calculated above (= 223.93 %). The small difference is purely due to the fact that several rounded values were used during the calculation of $\boldsymbol{W_{Theo.Plat.}}$.

Such a numerical comparison cannot be performed for the fully hydroxylated composition (in this case, $\mathbf{Zr_6O_{5.18}(OH)_{2.82}(BDC)_{3.88}(Benz)_{3.02}(Form)_{0.04}}$). Instead, we must compare its theoretical plateau (= 227.57 %, see above) with that experimentally observed in the TGA trace obtained on the sample (50Benz):

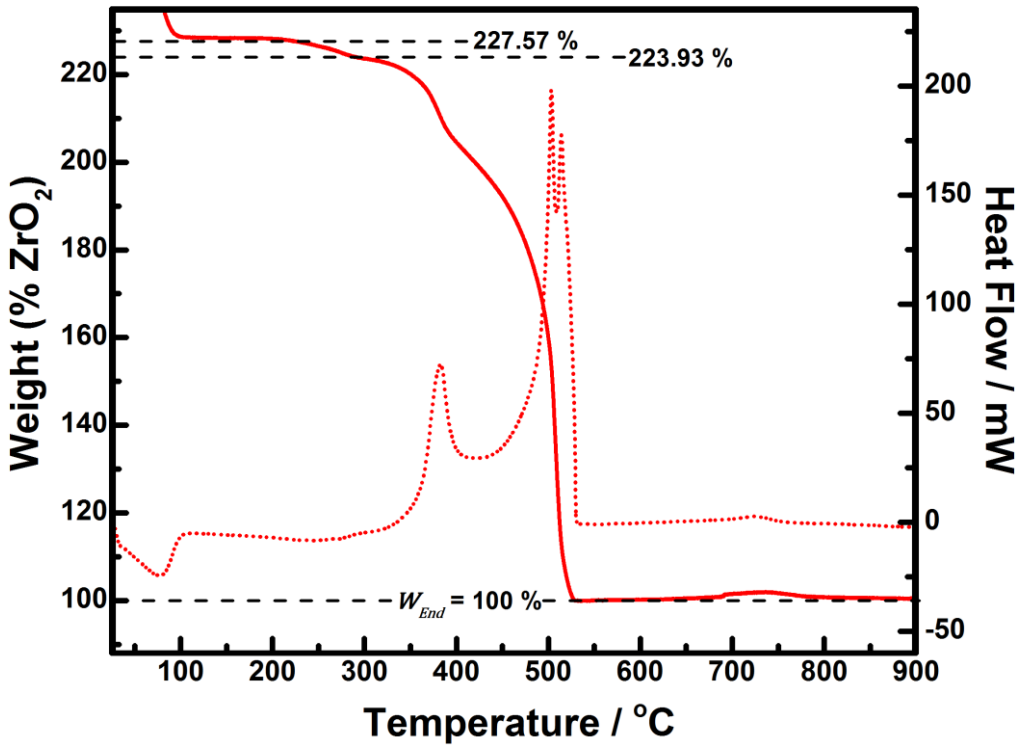

Figure S11. Comparing the theoretical TGA plateaus of our calculated compositions with those experimentally observed on 50Benz. Solid curve, left axis - TGA trace (normalized such that end weight ($\boldsymbol{W_{End}}$) = 100 %). Dotted curve, right axis – DSC signal. The horizontal dashed lines pinpoint the theoretical TGA plateaus of the compositions calculated in **Section 3.4.7.1.2**. The first weight loss (adsorbate volatilization) has been cut off from the y-scale range in order to improve the visual resolution of the two plateaus.

The two calculated theoretical TGA plateau weights are pinpointed by horizontal dashed lines in the above figure. As one can see, the theoretical plateau (= 227.57 %) of the hydroxylated composition (in this case, $\mathbf{Zr_6O_{5.18}(OH)_{2.82}(BDC)_{3.88}(Benz)_{3.02}(Form)_{0.04}}$) matches very closely with the first plateau observed in the TGA trace, during which the material is indeed expected to be in the hydroxylated form. Thus, our calculated hydroxylated composition (consistent with both TGA and NMR data) appears to be highly accurate, emphasizing the incredible power of the method.

Furthermore, the theoretical plateau (= 223.93 %) of the composition after dehydroxylation and formate loss (in this case, $\mathbf{Zr_6O_{6.61}(BDC)_{3.88}(Benz)_{3.02}}$) matches very closely with the second plateau in the TGA trace, further demonstrating the strength of the method.

3.4.7.2. 50Benz-HA

Table of Contents

3.4.7.2.1. Calculating the Values of x, y, and z

Upon inspection of the equations for $\boldsymbol{x}$, $\boldsymbol{y}$, and $\boldsymbol{z}$ (**Equations (32)**, **(36)**, and **(38)**, respectively) one can see that 5 input values ($\boldsymbol{Wt.Loss_{Exp.}}$, $\boldsymbol{Wt.PL_{Theo.}}$, $\boldsymbol{Wt.PB_{Theo.}}$, $\frac{\textbf{Benz.}}{\textbf{BDC}}\mathbf{m_R}$, and $\frac{\textbf{Form.}}{\textbf{BDC}}\mathbf{m_R}$) are required for their calculation.

However, two of these input values ($\boldsymbol{Wt.PL_{Theo.}}$ and $\boldsymbol{Wt.PB_{Theo.}}$) are automatically known ($\boldsymbol{Wt.PL_{Theo.}}$ = 20.03 %, $\boldsymbol{Wt.PB_{Theo.}}$ = 15.30 %) when TGA data is normalized by setting the end weight to 100 %, as we do herein (see **Sections 3.4.5.3** and **3.4.5.4** for relevant calculations).

This leaves $\boldsymbol{Wt.Loss_{Exp.}}$, $\frac{\textbf{Benz.}}{\textbf{BDC}}\mathbf{m_R}$, and $\frac{\textbf{Form.}}{\textbf{BDC}}\mathbf{m_R}$ as the remaining 3 inputs required to calculate $\boldsymbol{x}$, $\boldsymbol{y}$, and $\boldsymbol{z}$. As exemplified in **Section 3.4.5.2**, $\boldsymbol{Wt.Loss_{Exp.}}$ is calculated by analyzing TGA-DSC data. To this end, let us observe the TGA-DSC results obtained on 50Benz-HA:

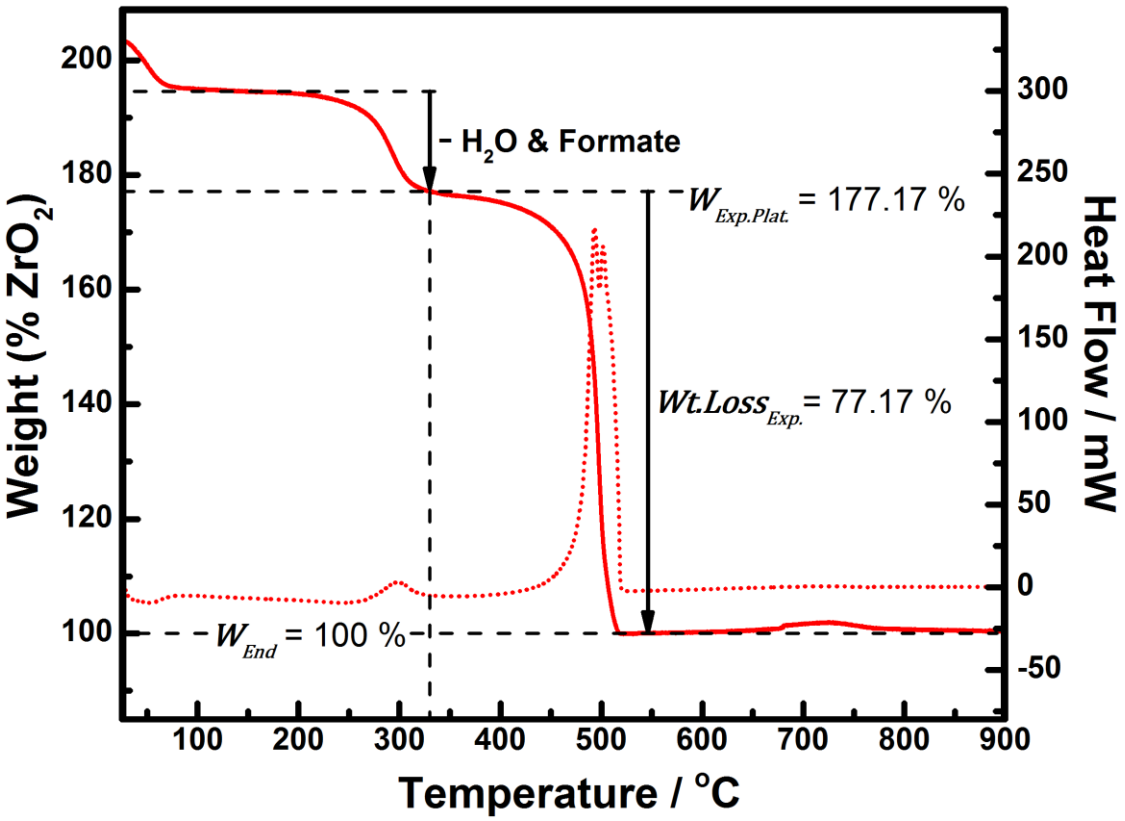

Figure S12. Calculation of $\boldsymbol{Wt.Loss_{Exp.}}$ from the TGA-DSC results obtained on 50Benz-HA. Solid curve, left axis - TGA trace (normalized such that end weight ($\boldsymbol{W_{End}}$) = 100 %). Dotted curve, right axis – DSC signal.

As can be seen, $\boldsymbol{Wt.Loss_{Exp.}}$ is simply the weight difference between $\boldsymbol{W_{Exp.Plat.}}$ and $\boldsymbol{W_{End}}$, where $\boldsymbol{W_{Exp.Plat.}}$ is the experimentally measured TGA plateau after dehydroxylation and formate loss (see **Section 3.4.4**) and $\boldsymbol{W_{End}}$ is the end weight of the material (i.e. its weight at 900 °C in the TGA trace):

$$\boldsymbol{Wt.Loss_{Exp.}} = \boldsymbol{W_{Exp.Plat.}} - \boldsymbol{W_{End}} \qquad (23)$$

As mentioned throughout this section, we normalize $\boldsymbol{W_{End}}$ to 100 % as standard practice, meaning that only the $\boldsymbol{W_{Exp.Plat.}}$ value is needed to calculate $\boldsymbol{Wt.Loss_{Exp.}}$. Choosing the correct $\boldsymbol{W_{Exp.Plat.}}$ value is critical to accurate analysis and requires one to pinpoint the temperature at which all dehydroxylation and formate loss is complete. To this end, we use the DSC trace as a guide, noting that a small exothermic peak (spanning a temperature range of *ca*. 250-330 °C) accompanies the TGA weight loss in this range. This peak is due to the loss of formate ligands (via combustion). The fact that the peak completely tails off at 330 °C strongly suggests that this is the temperature at which all formate has been completely removed. Moreover, dehydroxylation (which occurs over a temperature range of 200-325 °C, see **Figure S6** in **Section 3.4.2.1**) is also complete at 330 °C, which we have therefore chosen as the plateau temperature (emphasized by the vertical dashed line in the above figure). The $\boldsymbol{W_{Exp.Plat.}}$ value of the sample is simply its (normalized) weight at this temperature (= 177.17 % in this case, see figure). Inserting this value into **Equation (23)** yields a $\boldsymbol{Wt.Loss_{Exp.}}$ value of **<u>77.17 %</u>**, as also shown on the figure.

With $\boldsymbol{Wt.Loss_{Exp.}}$ now known, only $\frac{\textbf{Benz.}}{\textbf{BDC}}\mathbf{m_R}$, and $\frac{\textbf{Form.}}{\textbf{BDC}}\mathbf{m_R}$ are needed to fill in the equations for $\boldsymbol{x}$, $\boldsymbol{y}$, and $\boldsymbol{z}$. Fortunately, both of these values can be determined by dissolution/^{1}H NMR spectroscopy (see **Section 3.3** for details of the method), and the following values were obtained from the spectrum acquired on 50Benz-HA:

$$\frac{\textbf{Benz.}}{\textbf{BDC}}\mathbf{m_R} = \underline{\mathbf{0.04}}$$

$$\frac{\textbf{Form.}}{\textbf{BDC}}\mathbf{m_R} = \underline{\mathbf{0.72}}$$

These values are also presented later in **Table S3** (see **Section 4.2.1**), along with the numerical values of the ^{1}H NMR integrals relevant to their calculation. The spectrum from which these values were obtained is presented in **Figure 2** in the main article (red curves).

Returning to the task at hand, all 5 input values are now known, meaning that $\boldsymbol{x}$, $\boldsymbol{y}$, and $\boldsymbol{z}$ can finally be calculated with **Equations (32)**, **(36)** and **(38)**, respectively:

$$\boldsymbol{x} = \mathbf{6} - \left(\frac{\boldsymbol{Wt.Loss_{Exp.}}}{\left(\boldsymbol{Wt.PL_{Theo.}} + \left(\frac{\textbf{Benz.}}{\textbf{BDC}}\mathbf{m_R} \cdot \boldsymbol{Wt.PB_{Theo.}} \right) \right)} \right) \tag{32}$$

$$\boldsymbol{x = 6 - \left(\frac{77.17}{(20.03\,\% + \ (0.04 \cdot 15.30\,\%))} \right)}$$

$$\boldsymbol{x = \underline{2.26}}$$

$$\boldsymbol{2y = \left(\frac{Wt.Loss_{Exp.}}{\left(\left(\left(\frac{Benz.}{BDC} m_R \right)^{-1} \cdot Wt.PL_{Theo.} \right) + Wt.PB_{Theo.} \right)} \right)} \quad (36)$$

$$\boldsymbol{2y = \left(\frac{77.17}{(((0.04)^{-1} \cdot 20.03\,\%) + 15.30\,\%)} \right)}$$

$$\boldsymbol{2y = 0.15}$$

$$\boldsymbol{y = \underline{0.08}}$$

$$\boldsymbol{2z \ = (6 - x) \cdot \frac{Form.}{BDC} m_R} \quad (38)$$

$$\boldsymbol{2z \ = (6 - 2.26) \cdot \ 0.72}$$

$$\boldsymbol{2z = 2.69}$$

$$\boldsymbol{z = \underline{1.35}}$$

Note: all input values were rounded to 2 decimal places before being used to calculate $\boldsymbol{x}$, $\boldsymbol{y}$, and $\boldsymbol{z}$. Fortunately, this did not lead to any inaccuracies in this case – the exact same $\boldsymbol{x}$, $\boldsymbol{y}$, and $\boldsymbol{z}$ values (rounded to 2 decimal places) were obtained when more accurate input values were used.

3.4.7.2.2. Entering the x, y, & z Values into General Formulae to Obtain Full Compositions

Let us recall from **Section 3.4.4** that the general composition of our (non L-Serine functionalized) UiO-66 samples in their hydroxylated form is:

$$\mathbf{Zr_6O_{4+2x-2y-2z}(OH)_{4-2x+2y+2z}(BDC)_{6-x}(Benz)_{2y}(Form)_{2z}}$$

After dehydroxylation and formate loss (the 2nd TGA weight loss step, see **Section 3.4.4**), this composition becomes:

$$\mathbf{Zr_6O_{6+x-y}(BDC)_{6-x}(Benz)_{2y}}$$

With the x, y, and z values now known (= 2.26, 0.08, and 1.35, respectively, see previous subsection), they can be entered into the above general formulae to obtain the full composition of 50Benz-HA at both stages in its TGA trace. Starting with the hydroxylated composition:

$$\mathbf{Zr_6O_{4+2\cdot(2.26)-2\cdot(0.08)-2\cdot(1.35)}(OH)_{4-2\cdot(2.26)+2\cdot(0.08)+2\cdot(1.35)}(BDC)_{6-2.26}(Benz)_{2\cdot(0.08)}(Form)_{2\cdot(1.35)}}$$

$$\mathbf{= Zr_6O_{5.66}(OH)_{2.34}(BDC)_{3.74}(Benz)_{0.16}(Form)_{2.70}}$$

Which becomes the following after dehydroxylation and formate loss:

$$\mathbf{Zr_6O_{6+2.26-0.08}(BDC)_{6-2.26}(Benz)_{2\cdot(0.08)}}$$

$$\mathbf{= Zr_6O_{8.18}(BDC)_{3.74}(Benz)_{0.16}}$$

3.4.7.2.3. Checking the Validity of the Calculated Compositions

In order to test the validity of our calculated compositions, we check that:

1) The compositions are charge neutral. Both of the compositions calculated in the previous subsection pass this test.

2) The molar ratios between the organic components in the composition match with those obtained by dissolution/^{1}H NMR:

   In both compositions calculated in the previous subsection, the molar ratio between benzoate (**Benz**) and **BDC** is $\frac{0.16}{3.74} = \underline{\mathbf{0.04}}$, which is indeed the same value as that obtained by dissolution/^{1}H NMR (see **Section 3.4.7.2.1**).

   Moreover, the molar ratio between formate (**Form**) and **BDC** in the hydroxylated composition is $\frac{2.70}{3.74} = \underline{\mathbf{0.72}}$, which is indeed the same value as that obtained by dissolution/^{1}H NMR (see **Section 3.4.7.2.1**).

3) The theoretical TGA plateaus of the calculated compositions match well with those experimentally observed. To check this, we must first calculate the molar masses of our two compositions:

$$\mathbf{M\ Zr_6O_{8.18}(BDC)_{3.74}(Benz)_{0.16}} = \underline{\mathbf{1311.39}}\ \mathrm{g \cdot mol^{-1}}$$

and:

$$\mathbf{M\ Zr_6O_{5.66}(OH)_{2.34}(BDC)_{3.74}(Benz)_{0.16}(Form)_{2.70}} = \underline{\mathbf{1432.41}}\ \mathrm{g \cdot mol^{-1}}$$

We then obtain the theoretical TGA plateaus by entering these molar masses into **Equation (21)** (see **Section 3.4.2**):

$$\boldsymbol{W_{Theo.Plat.}} = \left(\frac{\boldsymbol{M_{Comp.}}}{\boldsymbol{M_{6\ ZrO_2}}}\right) \cdot \boldsymbol{W_{End}} \qquad (21)$$

$$\boldsymbol{W_{Theo.Plat.}} = \left(\frac{\mathbf{1311.39\ g \cdot mol^{-1}}}{\mathbf{739.34\ g \cdot mol^{-1}}}\right) \cdot \mathbf{100}\ \% = \underline{\mathbf{177.37}}\ \%$$

and:

$$\boldsymbol{W_{Theo.Plat.}} = \left(\frac{\mathbf{1432.41\ g \cdot mol^{-1}}}{\mathbf{739.34\ g \cdot mol^{-1}}}\right) \cdot \mathbf{100}\ \% = \underline{\mathbf{193.74}}\ \%$$

Simply from the value of its theoretical plateau, it is possible to scrutinize the validity of the composition after dehydroxylation and formate loss (in this case, $\mathbf{Zr_6O_{8.18}(BDC)_{3.74}(Benz)_{0.16}}$). Specifically, it should be equal to the experimental TGA plateau weight ($\boldsymbol{W_{Exp.Plat.}}$) originally entered into **Equation (23)** to calculate $\boldsymbol{Wt.Loss_{Exp.}}$ (see **Section 3.4.7.2.1**). In this case, the $\boldsymbol{W_{Exp.Plat.}}$ value was 177.17 % (see **Section 3.4.7.2.1**), which is extremely close to the theoretical value ($\boldsymbol{W_{Theo.Plat.}}$) calculated above (= 177.37 %). The small difference is purely due to the fact that several rounded values were used during the calculation of $\boldsymbol{W_{Theo.Plat.}}$.

Such a numerical comparison cannot be performed for the fully hydroxylated composition (in this case, $\mathbf{Zr_6O_{5.66}(OH)_{2.34}(BDC)_{3.74}(Benz)_{0.16}(Form)_{2.70}}$). Instead, we must compare its theoretical plateau weight (= 193.74 %, see above) with that experimentally observed in the TGA trace obtained on the sample (50Benz-HA):

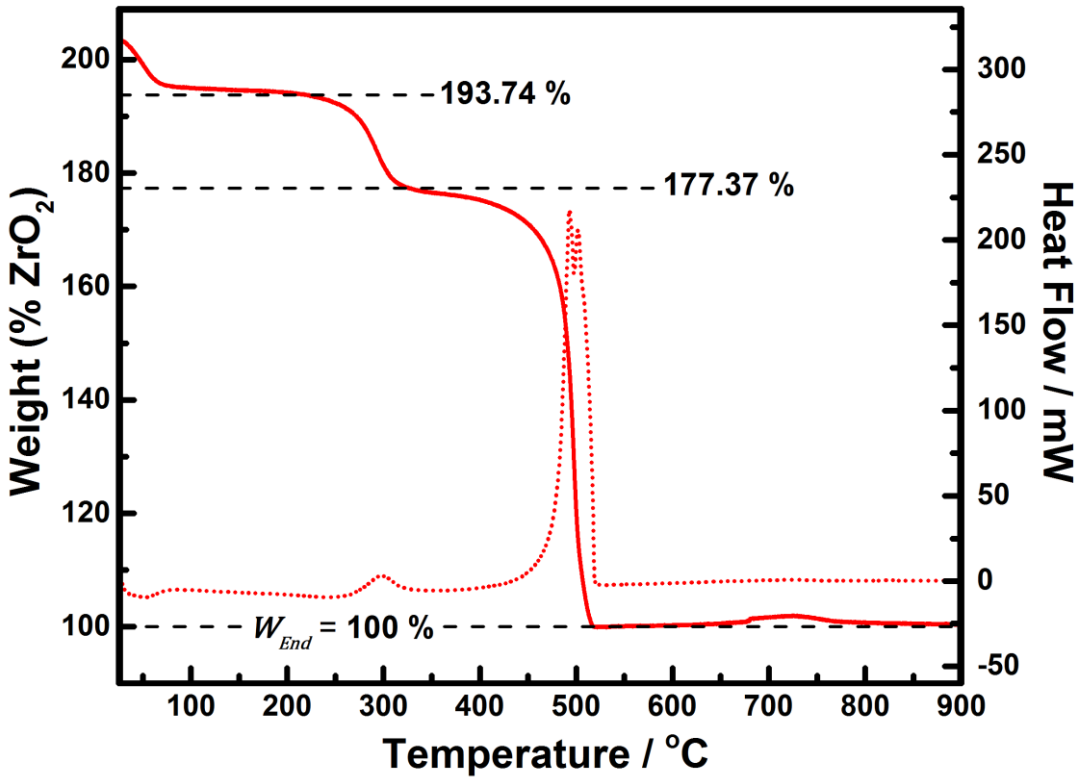

Figure S13. Comparing the theoretical TGA plateaus of our calculated compositions with those experimentally observed on 50Benz-HA. Solid curve, left axis - TGA trace (normalized such that end weight ($\boldsymbol{W_{End}}$) = 100 %). Dotted curve, right axis – DSC signal. The horizontal dashed lines pinpoint the theoretical TGA plateaus of the compositions calculated in **Section 3.4.7.2.2**.

The two calculated theoretical TGA plateau weights are pinpointed by horizontal dashed lines in the above figure. As one can see, the theoretical plateau (= 193.74 %) of the hydroxylated composition (in this case, $\mathbf{Zr_6O_{5.66}(OH)_{2.34}(BDC)_{3.74}(Benz)_{0.16}(Form)_{2.70}}$) matches quite closely with the first plateau observed in the TGA trace, during which the material is indeed expected to be in the hydroxylated form. Thus, our calculated hydroxylated composition (consistent with both TGA and NMR data) appears to be highly accurate, emphasizing the incredible power of the method.

Moreover, the theoretical plateau (= 177.37 %) of the composition after dehydroxylation and formate loss (in this case, $\mathbf{Zr_6O_{8.18}(BDC)_{3.74}(Benz)_{0.16}}$) matches closely with the second plateau in the TGA trace, further demonstrating the strength of the method.

3.5. Calculating CO_2/N_2 Adsorption Selectivities

CO_2/N_2 adsorption selectivities under conditions similar to that of post-combustion flue gases from coal-fueled power plants (a 150 mbar CO_2 / 750 mbar N_2 mixture at a total pressure of 1000 mbar and a temperature of 40 °C) were calculated from our pure component N_2 and CO_2 adsorption isotherms (obtained at 40 °C, see **Sections 4.6.1** and **4.6.2**) by application of Ideal Adsorbed Solution Theory[18] (IAST) using the pyIAST code.[19] With this code, each isotherm was first fit to the Langmuir model. These fits, together with the flue gas composition outlined above, were then provided as input for the IAST calculations, giving us the adsorbed loadings of CO_2 ($\mathbf{N_{CO_2}}$, labelled $\boldsymbol{x_a}$ in the program) and N_2 ($\mathbf{N_{N_2}}$, labelled $\boldsymbol{x_b}$ in the program) under these conditions (both in mmol·g^{-1}). These values were then entered into the following equation to calculate the CO_2/N_2 adsorption selectivities $\left(\mathbf{S_{CO_2/N_2}}\right)$:[20]

$$\mathbf{S_{CO_2/N_2}} = \frac{\mathbf{N_{CO_2} p_{N_2}}}{\mathbf{N_{N_2} p_{CO_2}}} \tag{39}$$

Where $\mathbf{p_{N_2}}$ and $\mathbf{p_{CO_2}}$ are the partial pressures of N_2 (= 750 mbar) and CO_2 (= 150 mbar) in flue gas, respectively.

3.6. Calculating the Isosteric Heat of CO_2 Adsorption

In accordance with the linearized Clausius-Clapeyron equation, the isosteric heat of CO_2 adsorption, ($\mathbf{Q_{iso}}$) was calculated from our CO_2 adsorption isotherms by entering their data into a plot of $\boldsymbol{ln(p)}$ against $\frac{\mathbf{1}}{\boldsymbol{T}}$ and extracting the slope:

$$\mathbf{ln(P)} = \frac{\mathbf{Q_{iso}}}{\mathbf{R}} \cdot \left(\frac{\mathbf{1}}{\mathbf{T}}\right) + \mathbf{C} \qquad (40)$$

Where:

R is the gas constant (8.314462 $JK^{-1}mol^{-1}$).

T is the temperature (in Kelvin) at which the isotherm was obtained. Herein, the isotherms were obtained at only two different temperatures (298.15 K and 313.15 K), meaning that there are just 2 data points in each linear plot.

P is the pressure (in mbar) at which the CO_2 adsorption loading **N** (in $mmol \cdot g^{-1}$) is reached, according to the following rearrangement of the Langmuir adsorption model (see **Section 2.11**):

$$\mathbf{P} = \left(\frac{\mathbf{N}}{\mathbf{kN_{sat}}}\right) - \mathbf{kN} \qquad (41)$$

Where $\mathbf{N_{sat}}$ and **k** were extracted from the Langmuir fits of our isotherms (see **Table S12** and **Table S13** in **Sections 4.6.1** and **4.6.2**, respectively).

The $\mathbf{Q_{iso}}$ values reported in **Table S14** (**Section 4.6.3**) were calculated at a CO_2 loading (i.e. **N**) of 0.01 $mmol \cdot g^{-1}$.

4. Results and Discussion

Table of Contents

4.1. Defectivity of 50Benz

Table of Contents

4.1.1. PXRD

The PXRD pattern obtained on 50Benz (after activation, see **Section 1.1**) is presented in **Figure S14**, where it is compared with the patterns obtained on a very defective (36Trif, see reference 3) and a near defect free (UiO-66-Ideal, see **Sections 1.3** and **3.4.2.1**) UiO-66 sample:

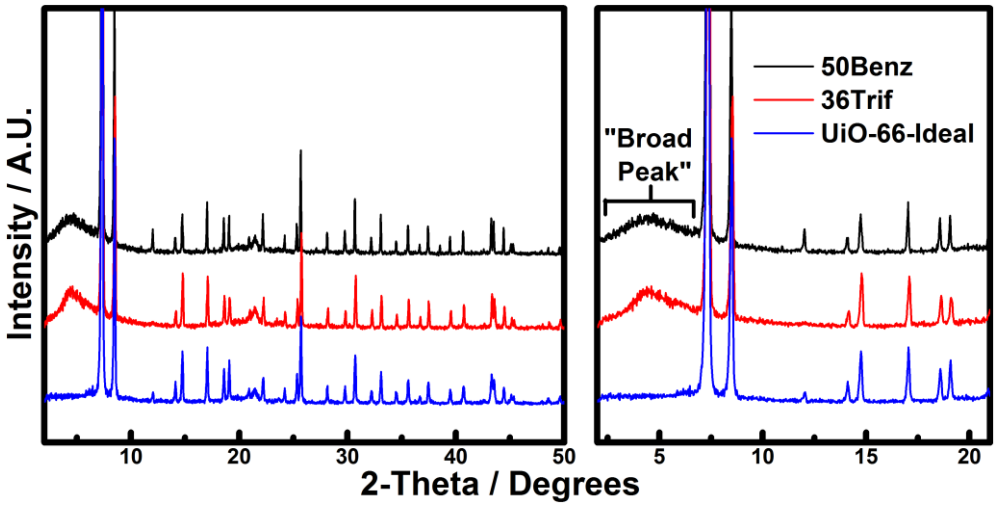

Figure S14. Comparison of the PXRD patterns obtained on three different UiO-66 samples; 50Benz, 36Trif, and UiO-66-Ideal. The same y-Scale is applied to both plots.

As one can see from the overall patterns (left plot in figure), all 3 samples are highly crystalline. However, the patterns differ in the region preceding the first reflection of the UiO-66 phase. This region is emphasized in the right plot of the figure, where it can be seen that a very broad peak (spanning a 2θ range of *ca*. 2-7°) is observed in the PXRD patterns obtained on 50Benz and 36Trif.

In a previous study, we unambiguously assigned this "broad peak" to very tiny "nanoregions" of missing cluster defects.[3] In the same study, we went on to show that the relative intensity of the broad peak ($\boldsymbol{Rel(I)_{B.P.}}$, see **Section 3.1**) is proportional to the concentration of missing cluster defects, and that 36Trif was the most defective of a series of 15 UiO-66 samples. The absence of this peak in the pattern obtained on UiO-66-Ideal is testament to its very low defectivity.

As can be seen from the figure, the intensity of the broad peak in the pattern obtained on 50Benz is similar to that of 36Trif (albeit with a different shape), implying that it contains a similar concentration of missing cluster defects. In order to scrutinize this observation in a more quantitative manner, we calculated the $\boldsymbol{Rel(I)_{B.P.}}$ values from the patterns (see **Section 3.1** for method) and found that the value (and thus the concentration of missing cluster defects) is actually higher for 50Benz (0.454) than it is for 36Trif (0.340). The peak intensities relevant to the calculation of $\boldsymbol{Rel(I)_{B.P.}}$ are provided in **Table S2**:

Table S2. Quantitative data extracted from the PXRD patterns shown in **Figure S14**. See **Section 3.1** for details of the method used to extract this data. $\boldsymbol{Rel(I)_{B.P.}}$ values were calculated with **Equation (4)**.

Sample Name	Peak Intensity / Error				$\boldsymbol{Rel(I)_{B.P.}}$ / Error*
	Broad Peak	(111)	(200)	(600)	
50Benz	0.484 / 0.032	1.578 / 0.024	0.384 / 0.015	1.239 / 0.075	0.454 / 0.032
36Trif[3]	0.372 / 0.016	1.262 / 0.024	0.464 / 0.018	1.555 / 0.098	0.340 / 0.018

***** Error calculated with standard rules of error propagation.

4.1.2. TG-DSC

The TGA-DSC results obtained on 50Benz are presented in **Figure S15**:

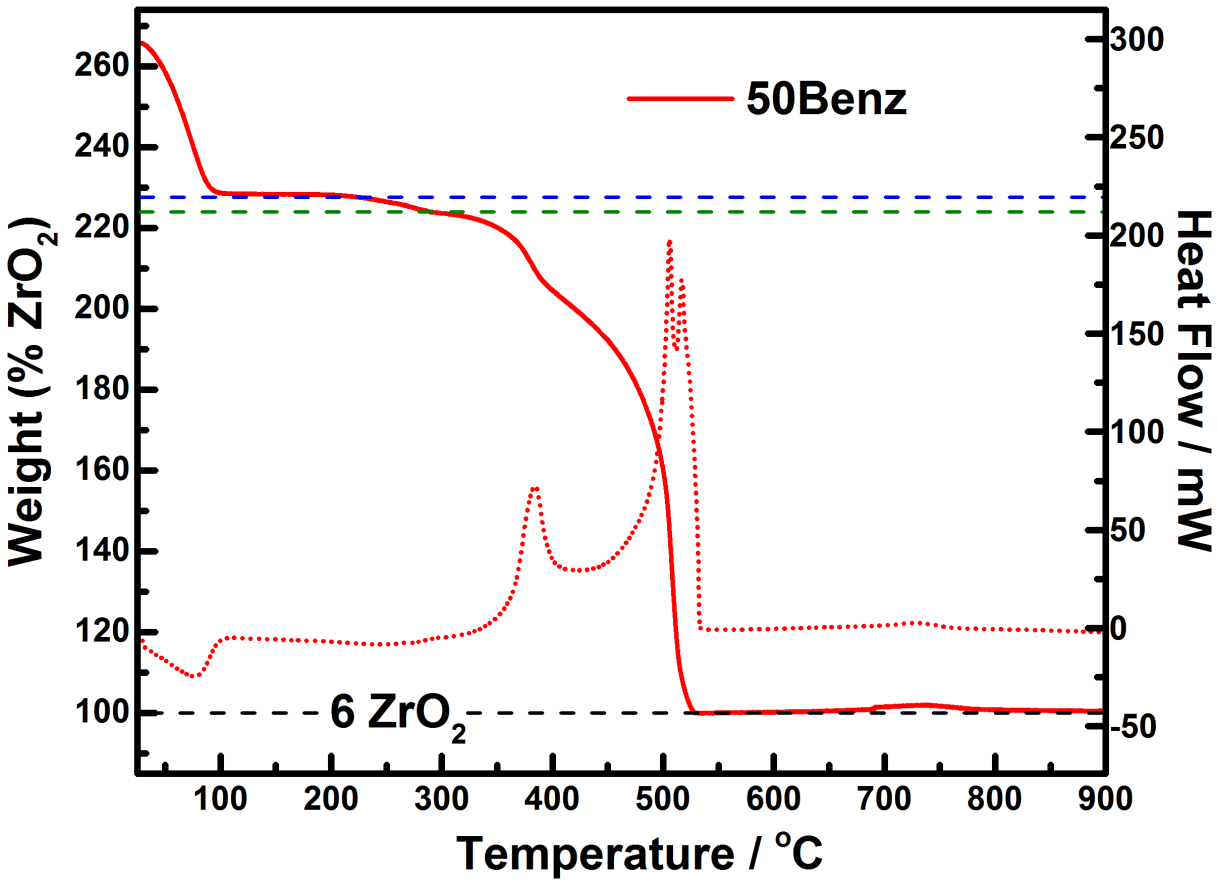

Figure S15. TGA-DSC results obtained on 50Benz. The sample was activated prior to measurement (see **Section 1.1** for details). Solid curve, left axis - TGA trace (normalized such that end weight = 100%). Dotted curve, right axis – DSC trace.

Three well resolved weight losses are observed in the TGA trace (end weight normalized to 100 %). In accordance with previous studies, the losses are assigned to the following chemical processes:

1) Adsorbate volatilization (in this case H_2O). Occurs over a temperature range of *ca.* 25-100 °C. After this weight loss, the material is in the empty, hydroxylated form.

2) Formate loss and dehydroxylation of the Zr_6 cornerstones. These two weight loss events occur over a similar temperature range (*ca.* 200-290 °C here) and are thus not well resolved from one another. The magnitude of this weight loss step is rather small in this case, an observation which can easily be attributed to the very low amount of formate in the sample (see dissolution/^{1}H NMR results in **Figure 2** (main article) and **Section 4.2.1**).

3) Benzoate loss and framework decomposition. These two weight loss events are not well resolved from one another. The temperature range of the combined weight loss is *ca.* 290 – 530 °C. These weight losses are accompanied by very intense exothermic peaks in the DSC trace. The final product is ZrO_2.

By combining TGA and dissolution/^{1}H NMR results (see **Section 3.4** for details of the method and how it is derived), we estimate that the composition of 50Benz (in the fully hydroxylated form) is $\mathbf{Zr_6O_{5.18}(OH)_{2.82}(BDC)_{3.88}(Benz)_{3.02}(Form)_{0.04}}$. The calculation of this composition was exemplified and scrutinized in **Section 3.4.7.1**. The theoretical TGA plateau weight (calculated by **Equation (21)**, see **Section 3.4.2**) of this composition (given its weight relative to the final product (6 moles of ZrO_2)) is emphasized by the blue dashed line in the figure. As one can see, it matches very well with the experimentally observed TGA plateau, highlighting that the calculated composition is indeed reasonable.

After dehydroxylation and formate loss, the composition of the same material is expected to be $\mathbf{Zr_6O_{6.61}(BDC)_{3.88}(Benz)_{3.02}}$ (as also calculated in **Section 3.4.7.1**). Indeed, the theoretical TGA plateau weight (calculated by **Equation (21)**, see **Section 3.4.2**) of this composition (emphasized by a green dashed line in the figure) once again matches well with the experimentally observed TGA plateau. These observations provide confidence that the estimated compositions (consistent with both TGA and dissolution/^{1}H NMR results) are reasonable.

Perhaps more importantly, these compositions allow us to assess the defectivity of the sample. In our previous study,[3] we used TGA to quantitatively compare the defectivity of 15 different UiO-66 samples. Specifically, we calculated the number of linker deficiencies per Zr_6 formula unit, i.e. the value of $\boldsymbol{x}$ in the molecular formula $\mathbf{Zr_6O_{6+x}(BDC)_{6-x}}$.

However, such a composition is never reached in benzoate-containing defective UiO-66 sample such as 50Benz. Instead, the general composition of benzoate-containing defective UiO-66 samples (after dehydroxylation and labile ligand (e.g. formate) loss, see **Section 3.4.4**) is $\mathbf{Zr_6O_{6+x-y}(BDC)_{6-x}(Benz)_{2y}}$, where $\boldsymbol{x}$ is again the number of linker deficiencies per Zr_6 formula unit and is still a quantitative measure of the defectivity of the material.

As discussed above, the composition of 50Benz is $\mathbf{Zr_6O_{6.61}(BDC)_{3.88}(Benz)_{3.02}}$ at this stage, and thus its $\boldsymbol{x}$ value is (6 - 3.88) = **<u>2.12</u>** (as was also calculated in **Section 3.4.7.1.1**). To put this into context, this means that there are only 12 - (2.12 x 2) = **<u>7.76</u>** BDC linkers coordinated to the average Zr_6 cluster in 50Benz, far less than the 12 linkers in defect free UiO-66. Even more interestingly, this $\boldsymbol{x}$ value makes 50Benz even more defective than the most defective sample from our previous study (36Trif, $\boldsymbol{x}$ = **<u>2.01</u>**),[3] a finding which is in agreement with the PXRD results presented in **Section 4.1.1**.

Table of Contents

4.2.1. Benzoate/Formate Ligand Exchange: Molar Ratios from Dissolution / ^{1}H NMR

Figure S16 graphically depicts how the HCl activation procedure affects $\frac{\text{Benz.}}{\text{BDC}}\mathbf{m}_R$ and $\frac{\text{Form.}}{\text{BDC}}\mathbf{m}_R$ (the benzoate/BDC and the formate/BDC molar ratio, respectively). The values (presented in **Table S3**, along with the numerical values of the ^{1}H NMR integrals relevant to their calculation) were obtained via integration of the dissolution/^{1}H NMR spectra shown in **Figure 2** (main article). See **Section 3.3** for details of the method.

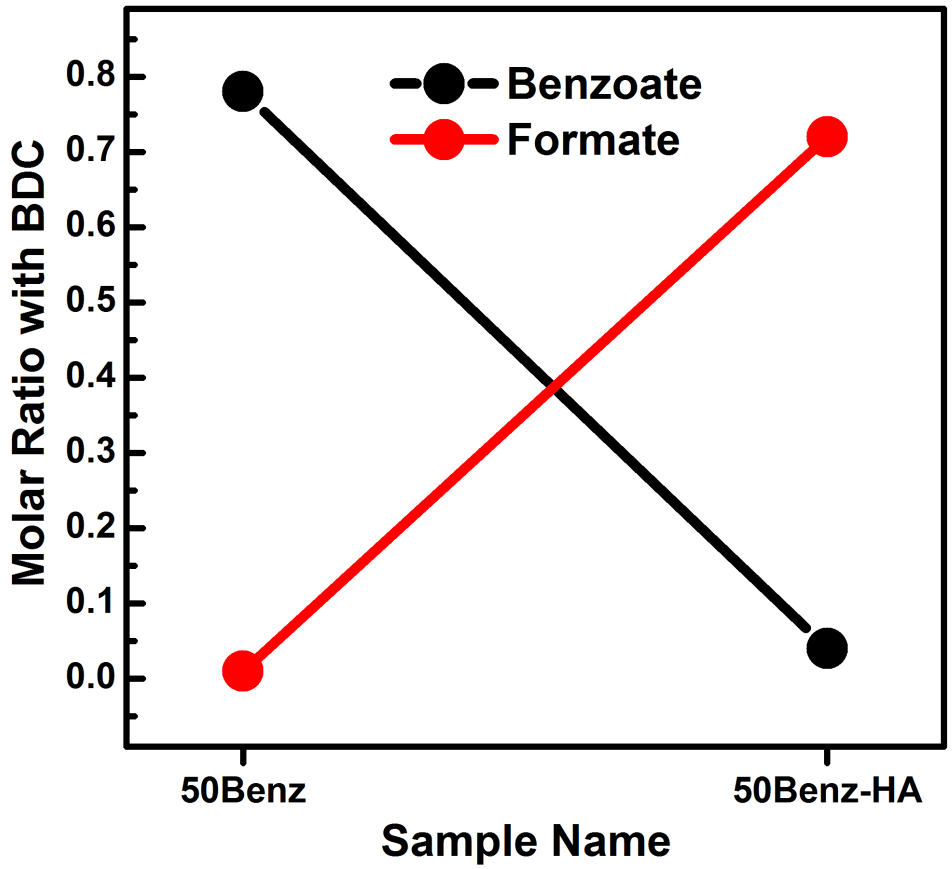

Figure S16. Benzoate to BDC $\left(\frac{\text{Benz.}}{\text{BDC}}\mathbf{m}_R\right)$ and formate to BDC $\left(\frac{\text{Form.}}{\text{BDC}}\mathbf{m}_R\right)$ molar ratios before (50Benz) and after HCl activation (50Benz-HA).

By analyzing the figure and the tabulated data, it is clear that HCl activation results in an almost quantitative ligand exchange reaction between benzoate and formate.

Table S3. Quantitative data extracted from the dissolution/^{1}H NMR spectra obtained before (50Benz) and after HCl activation (50Benz-HA). The meaning of these values (and the method with which they were obtained) is outlined in **Section 3.3**.

Sample	$(\mathbf{BDC} + \mathbf{Benz.H_a})$ Int.	$\mathbf{Benz.H_b}$ Int.	Form. Int.	$\frac{\text{Benz.}}{\text{BDC}}\mathbf{m}_R$ †	$\frac{\text{Form.}}{\text{BDC}}\mathbf{m}_R$ ‡
50Benz	6.00*	1.68	0.01	0.78	0.01
50Benz-HA	6.00*	0.12	1.06	0.04	0.72

* The $(\mathbf{BDC} + \mathbf{Benz.H_a})$ signal was integrated and its numerical value normalized to 6.00 prior to all further integration.
† Calculated by **Equation (16)**, derived in **Section 3.3.4**.
‡ Calculated by **Equation (18)**, derived in **Section 3.3.4**.

4.2.2. PXRD: Crystallinity and Defectivity

Figure S17 compares the PXRD results obtained on 50Benz before (50Benz) and after (50Benz-HA) HCl activation:

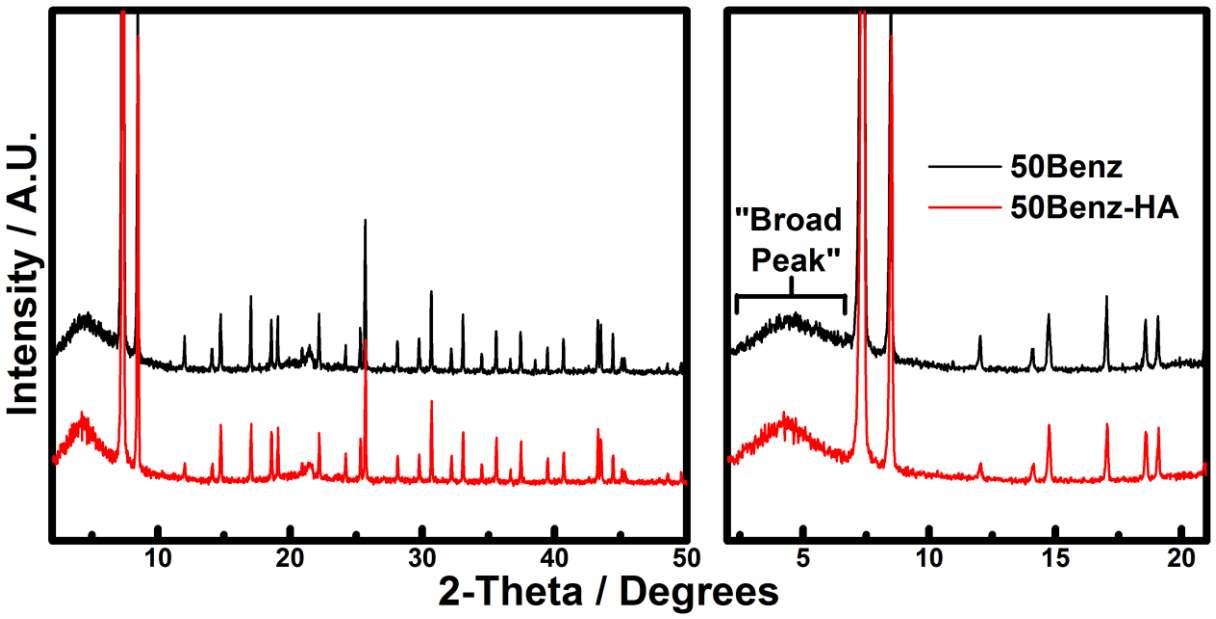

Figure S17. Comparison of the PXRD patterns obtained before (50Benz) and after (50Benz-HA) HCl activation. Samples were activated (i.e. desolvated) prior to measurement (see **Sections 1.1** and **1.2**). The same y-Scale is applied to both plots.

As one can see from the overall patterns (left plot in figure), the crystallinity of the material is completely preserved after HCl activation. Moreover, the intensity of the "broad peak" (spanning a 2θ range of *ca*. 2-7°, emphasized in the right plot) does not appear to change significantly. As discussed in **Section 4.1.1**, this peak is due to very tiny "nanoregions" of missing cluster defects in the samples, and its relative intensity ($\boldsymbol{Rel(I)_{B.P.}}$, see **Section 3.1**) is propotional to the concentration of these defects. The fact that the intensity of the broad peak does not appear to significantly change after HCl activation therefore suggests that 50Benz's very high concentration of missing cluster defects (see **Section 4.1.1**) is preserved. In order to quantitatively scrutinize this qualitative observation, we calculated the relative intensity of the broad peak ($\boldsymbol{Rel(I)_{B.P.}}$) from the patterns (see **Section 3.1** for method). The values and the peak intensities relevant to their calculation are provided in **Table S4**:

Table S4. Quantitative data extracted from the PXRD patterns shown in **Figure S14**. See **Section 3.1** for details of the method used to extract this data. $\boldsymbol{Rel(I)_{B.P.}}$ values were calculated with **Equation (4)**.

Sample Name	Peak Intensity / Error				$\boldsymbol{Rel(I)_{B.P.}}$ / Error*
	Broad Peak	(111)	(200)	(600)	
50Benz	0.484 / 0.032	1.578 / 0.024	0.384 / 0.015	1.239 / 0.075	0.454 / 0.032
50Benz-HA	0.508 / 0.005	1.455 / 0.023	0.504 / 0.016	1.264 / 0.077	0.473 / 0.013

***** Error calculated with standard rules of error propagation.

As can be seen, the relative intensity of the broad peak (and thus the concentration of missing cluster defects) actually increases very slightly after HCl activation. This might indicate that a small number of clusters may be removed during HCl activation, but the numbers are too similar to make a definitive statement on this.

4.2.3. TGA-DSC

Figure S18 compares the TGA-DSC results obtained on 50Benz before (50Benz) and after (50Benz-HA) HCl activation:

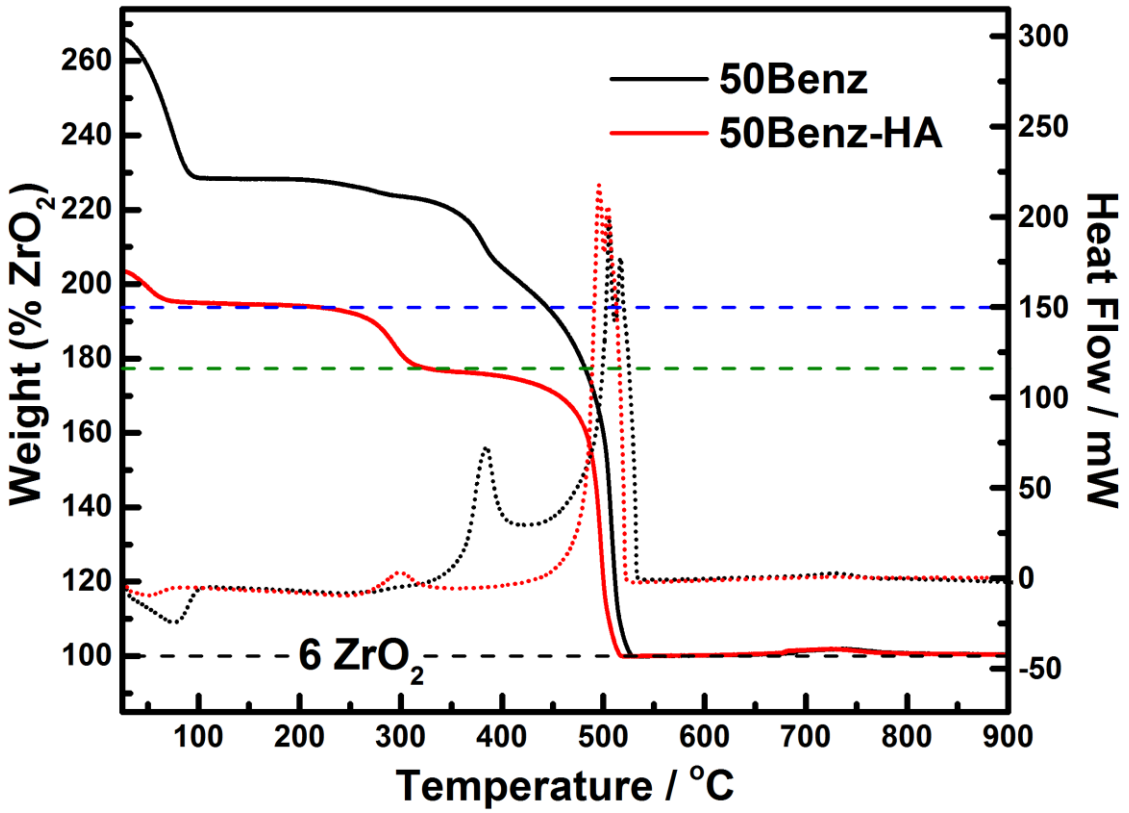

Figure S18. Comparison of the TGA-DSC results obtained before (50Benz) and after (50Benz-HA) HCl activation. Solid curves, left axis - TGA traces (normalized such that end weight = 100%). Dotted curve, right axis – DSC traces. Samples were activated (i.e. desolvated) prior to measurement (see **Sections 1.1** and **1.2**)

The results obtained on 50Benz were discussed in **Section 4.1.2** and are merely shown for comparison.

Three well resolved weight losses are observed in the TGA trace obtained on 50Benz-HA. In accordance with previous studies, the losses are assigned to the following chemical processes:

1) Adsorbate volatilization (in this case H_2O). Occurs over a temperature range of *ca*. 25-80 °C. After this weight loss, the material is in the empty, hydroxylated form.
2) Formate loss and dehydroxylation of the Zr_6 cornerstones. These two weight loss events occur over a similar temperature range (*ca*. 210-330 °C) and are thus not well resolved from one another. Note that this weight loss step (accompanied by a small exothermic peak in the DSC trace) is much larger in 50Benz-HA than in 50Benz. This is due to the fact that 50Benz-HA contains much more formate than 50Benz (see NMR results in **Figure 2** (main article) and **Section 4.2.1**).
3) Benzoate loss and framework decomposition. These two weight loss steps occur over a similar temperature range (*ca*. 330-530 °C) and are thus not well resolved from one another. Note that this weight loss step is much smaller in 50Benz-HA than it is for 50Benz. This is due to the fact that 50Benz-HA contains much less benzoate than 50Benz (see NMR results in **Figure 2** (main article) and **Section 4.2.1**).

By combining TGA and dissolution/^{1}H NMR results (see **Section 3.4** for details of the method and how it is derived), we estimate that the composition of 50Benz-HA (in the fully hydroxylated form) is $\mathbf{Zr_6O_{5.66}(OH)_{2.34}(BDC)_{3.74}(Benz)_{0.16}(Form)_{2.70}}$. The calculation of this composition was exemplified and scrutinized in **Section 3.4.7.2**. The theoretical TGA plateau (calculated by **Equation (21)**, see **Section 3.4.2**) of this composition (given its weight relative to the final product (6 moles of ZrO_2)) is emphasized by the blue dashed line in the figure. As one can see, it matches very well with the experimentally observed TGA plateau, highlighting that the calculated composition is indeed reasonable.

After dehydroxylation and formate loss, the composition of the same material is expected to be $\mathbf{Zr_6O_{8.18}(BDC)_{3.74}(Benz)_{0.16}}$ (as also calculated in **Section 3.4.7.2**). Indeed, the theoretical TGA plateau (calculated by **Equation (21)**, see **Section 3.4.2**) of this composition (emphasized by a green dashed line in the figure) once again matches well with the experimentally observed TGA plateau. These observations provide confidence that the estimated compositions (consistent with both TGA and dissolution/^{1}H NMR results) are reasonable.

Perhaps more importantly, these compositions allow us to assess the defectivity of the sample. In our previous study,[3] we used TGA to quantitatively compare the defectivity of 15 different UiO-66 samples. Specifically, we calculated the number of linker deficiencies per Zr_6 formula unit, i.e. the value of $\boldsymbol{x}$ in the molecular formula $\mathbf{Zr_6O_{6+x}(BDC)_{6-x}}$.

However, such a composition is never reached in benzoate containing defective UiO-66 sample such as 50Benz-HA. Instead, the general composition of benzoate containing defective UiO-66 samples (after dehydroxylation and labile ligand (e.g. formate) loss, see **Section 3.4.4**) is $\mathbf{Zr_6O_{6+x-y}(BDC)_{6-x}(Benz)_{2y}}$, where $\boldsymbol{x}$ is again the number of linker deficiencies per Zr_6 formula unit and is still a quantitative measure of the defectivity of the material.

As discussed above, the composition of 50Benz-HA is $\mathbf{Zr_6O_{8.18}(BDC)_{3.74}(Benz)_{0.16}}$ at this stage, and thus its $\boldsymbol{x}$ value is (6 - 3.74) = **2.26** (as was also calculated in **Section 3.4.7.2**). To put this into context, this means that there are only 12 - (2.26 x 2) = **7.48** BDC linkers coordinated to the average Zr_6 cluster in 50Benz, far less than the 12 linkers in defect free UiO-66. Moreover, this $\boldsymbol{x}$ value reveals that 50Benz-HA is slightly more defective than the 50Benz starting material, in which $\boldsymbol{x}$ = **2.12** (see **Section 4.1.2**). This suggests that a small amount of linkers and/or clusters are removed during HCl activation, a finding which is in agreement with the PXRD results presented in **Section 4.2.2**.

4.2.4. ATR-IR

Figure S19 compares the ATR-IR spectra obtained on 50Benz before (50Benz) and after (50Benz-HA) HCl activation:

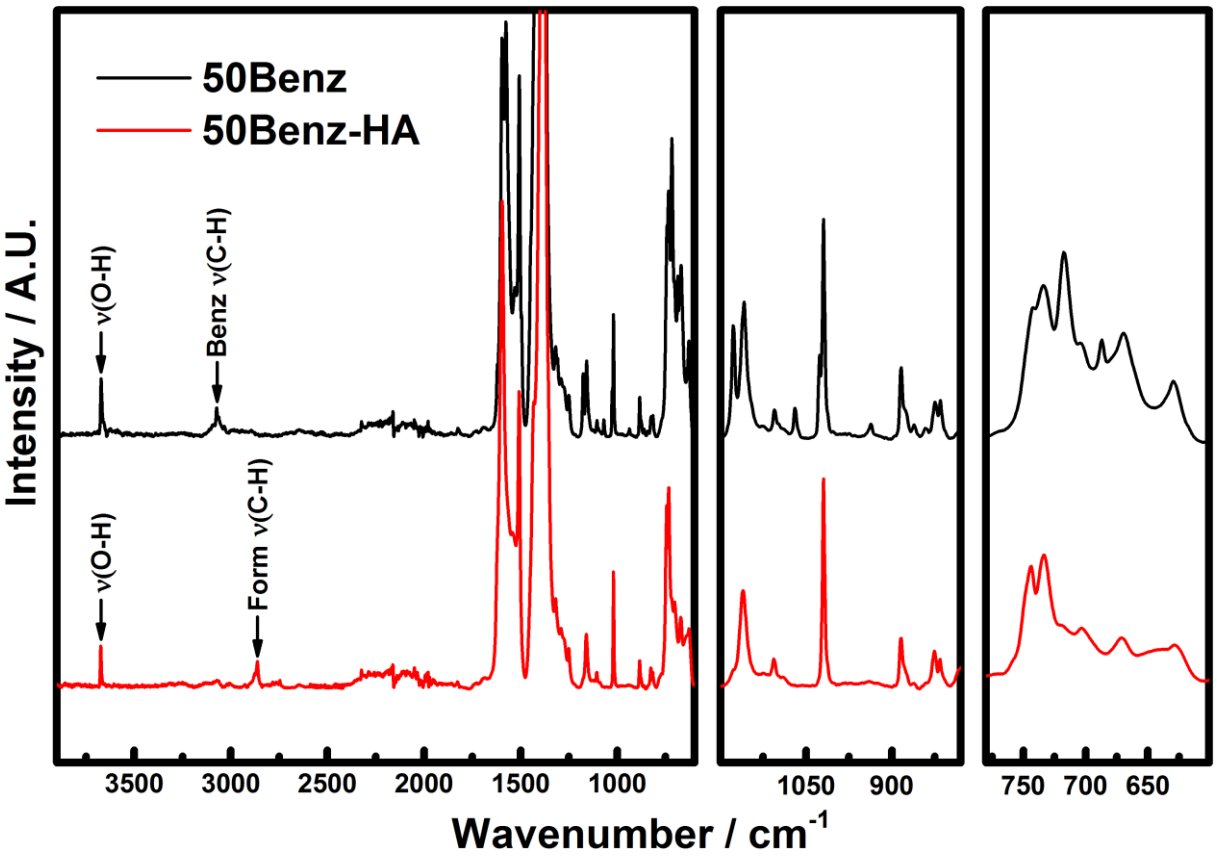

Figure S19. Comparison of the ATR-IR spectra obtained before (50Benz) and after (50Benz-HA) HCl activation. Samples were activated (i.e. desolvated) by simultaneous vacuum and heat treatment (see **Table S1**) before being transferred to a glovebox (N_2 atmosphere) for measurement.

As can be seen in the figure, only one band (appearing at 3672 cm^{-1}) is observed in the O-H stretching region of the spectra. This band has previously been conclusively assigned to the O-H stretching mode of the μ^3 hydroxyl groups on the inorganic cornerstones. The fact that no new O-H stretching bands appear after HCl activation strongly suggests that the benzoate ligands are not replaced by –OH groups (contrary to what was observed by Farha et al. in their work on NU-1000).[2]

Considering the overall spectrum (see left plot in figure), one can see that, as a whole, the spectrum isn't altered too significantly after HCl activation. However, some clear differences can be observed upon closer inspection. The most important difference is in the C-H stretching region, where the two spectra each feature a mutually exclusive band. Given our dissolution/^{1}H NMR results (see **Figure 2** (main article) and **Section 4.2.1**), we confidently assign these bands to C-H stretching modes of benzoate (50Benz) and formate (50Benz-HA), appearing at 3074 and 2861 cm^{-1}, respectively. These assignments are highlighted on the figure.

Other differences between the spectra are highlighted in the middle and rightmost plots in the figure. Some of the bands in the middle plot disappear after HCl activation. These bands are thus likely to be associated with vibrational modes of the benzoate ligands (e.g. C-O stretching modes).

4.2.5. EDX: Chlorine Content

Figure S20 compares the energy dispersive X-ray spectra obtained on 50Benz before (50Benz) and after (50Benz-HA) HCl activation:

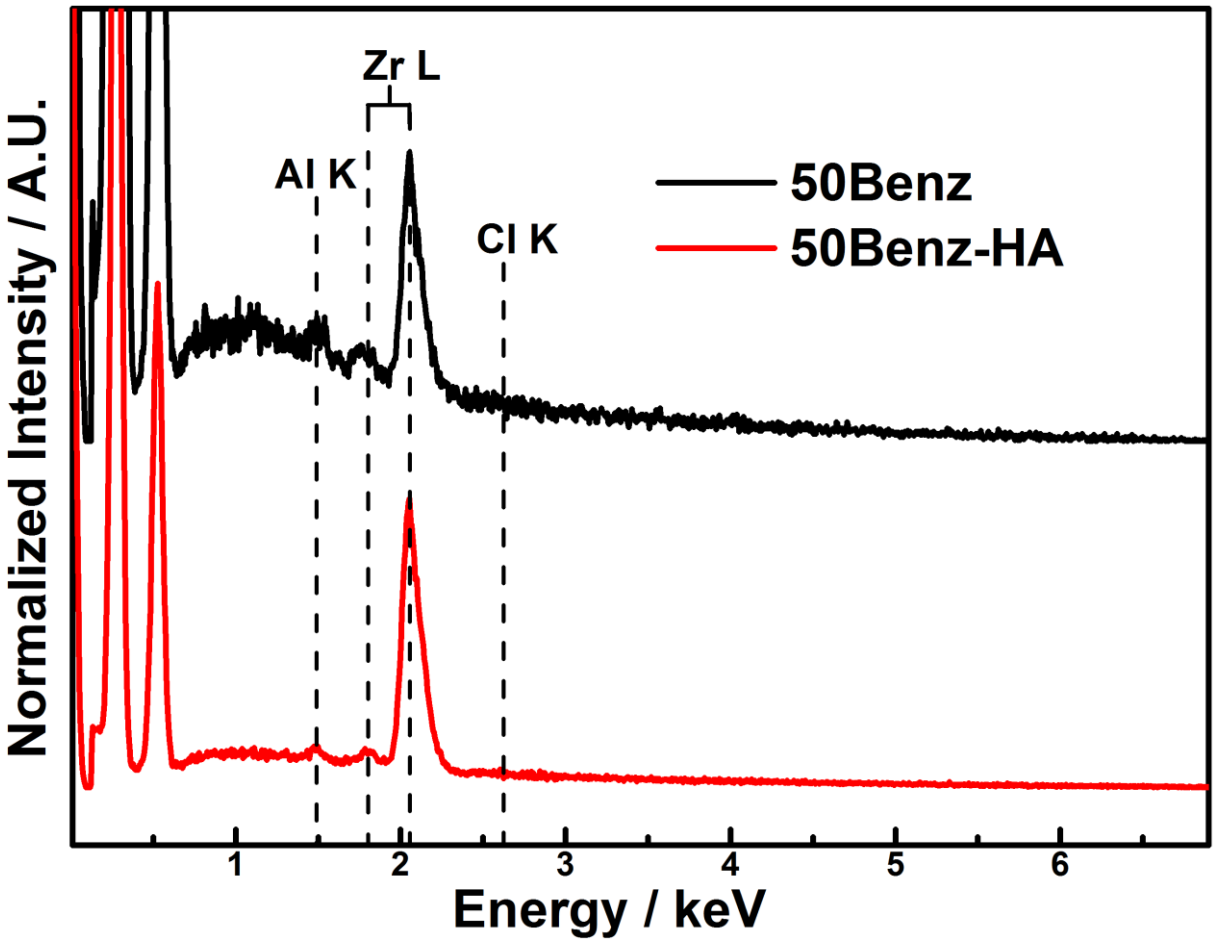

Figure S20. EDX spectra obtained on 50Benz and 50Benz-HA. The aluminum originates from the sample holder.

As can be seen, neither of the samples (both of which were measured in the "as synthesized" form) contain a detectable amount of chlorine. This observation rules out the possibility that the defects are compensated by chloride ligands.

4.3. Comparing 50Benz-HA to Formic Acid Modulated Samples

Table of Contents

4.3.1. PXRD: Crystallinity and Defectivity

Figure S21 compares the PXRD pattern collected on 50Benz-HA with those obtained on the formic acid modulated samples from our previous study.[3]

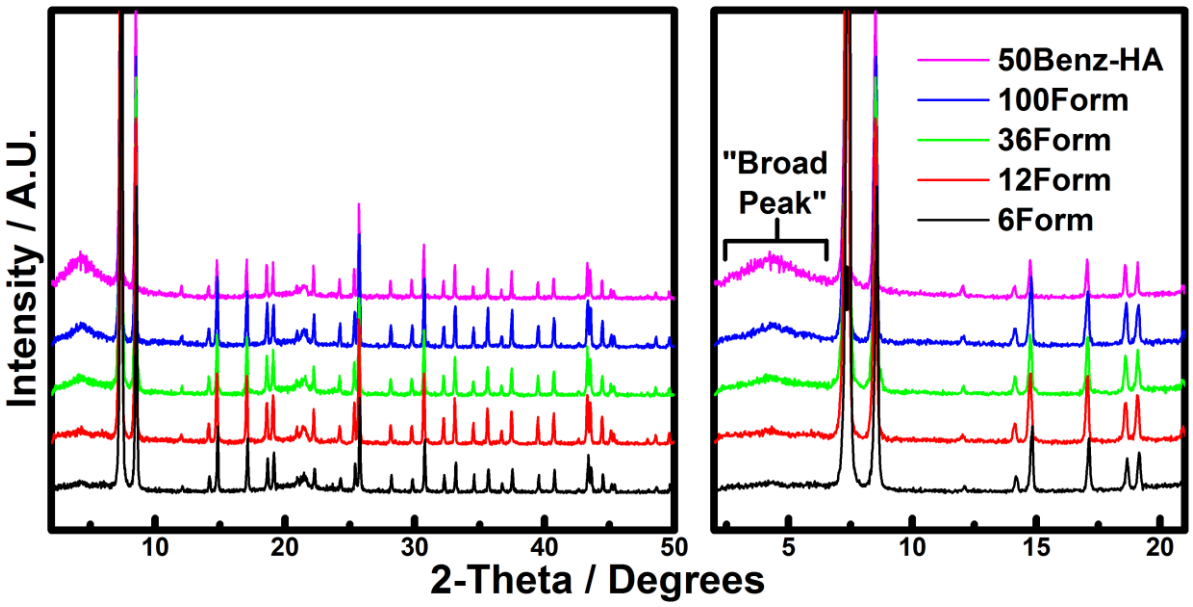

Figure S21. Comparison of the PXRD patterns obtained on 50Benz-HA and the formic acid modulated samples from our previous study.[3] The same y-Scale is applied to both plots.

As one can see from the overall patterns (left plot in figure), all 5 samples are highly crystalline. However, the intensity of the "broad peak" (see right plot) varies among the patterns. In our previous work,[3] we unambiguously assigned this peak to very tiny "nanoregions" of missing cluster defects and demonstrated that it's relative intensity ($\boldsymbol{Rel(I)_{B.P.}}$) is proportional to the concentration of these defects in the sample.

Qualitatively speaking, one can see that the intensity of the broad peak in the pattern obtained on 50Benz-HA is far greater than those observed in the other samples. In order to scrutinize this observation in a more quantitative manner, we calculated the $\boldsymbol{Rel(I)_{B.P.}}$ values from the patterns (see **Section 3.1** for method). The values and the peak intensities relevant to their calculation are provided in **Table S5**:

Table S5. Quantitative data extracted from the PXRD patterns shown in **Figure S14**. See **Section 3.1** for details of the method used to extract this data. $\boldsymbol{Rel(I)_{B.P.}}$ values were calculated with **Equation (4)**.

Sample Name	Peak Intensity / Error				$\boldsymbol{Rel(I)_{B.P.}}$ / Error*
	Broad Peak	(111)	(200)	(600)	
50Benz-HA	0.508 / 0.005	1.455 / 0.023	0.504 / 0.016	1.264 / 0.077	0.473 / 0.013
100Form	0.196 / 0.030	1.911 / 0.033	0.651 / 0.024	1.950 / 0.130	0.130 / 0.020
36Form	0.136 / 0.022	2.025 / 0.031	0.760 / 0.024	1.880 / 0.120	0.087 / 0.014
12Form	0.104 / 0.038	1.901 / 0.033	0.729 / 0.025	2.240 / 0.063	0.064 / 0.023
6Form	0.066 / 0.011	1.764 / 0.031	0.690 / 0.024	1.990 / 0.120	0.045 / 0.008

***** Error calculated with standard rules of error propagation.

Indeed, one can see that the relative intensity of the broad peak (and hence the concentration of missing cluster defects) in 50Benz-HA ($\boldsymbol{Rel(I)_{B.P.}}$ = 0.473) is much higher than the formic acid modulated samples from our previous study. The most defective of the formic acid modulated samples, 100Form ($\boldsymbol{Rel(I)_{B.P.}}$ = 0.130) is much less defective than 50Benz-HA, despite the fact that it was synthesized with a very large (100-fold) excess of formic acid. This suggests that it may not be possible to attain a sample as defective as 50Benz-HA by directly employing formic acid as a modulator in the UiO-66 synthesis mixture. However, we cannot completely rule out the possibility that similar results could be obtained by using an enormous excess of formic acid as modulator.

4.3.2. Dissolution / ^{1}H NMR

Figure S22 compares the dissolution/^{1}H NMR spectrum collected on 50Benz-HA with those obtained on the formic acid modulated samples from our previous study.[3]

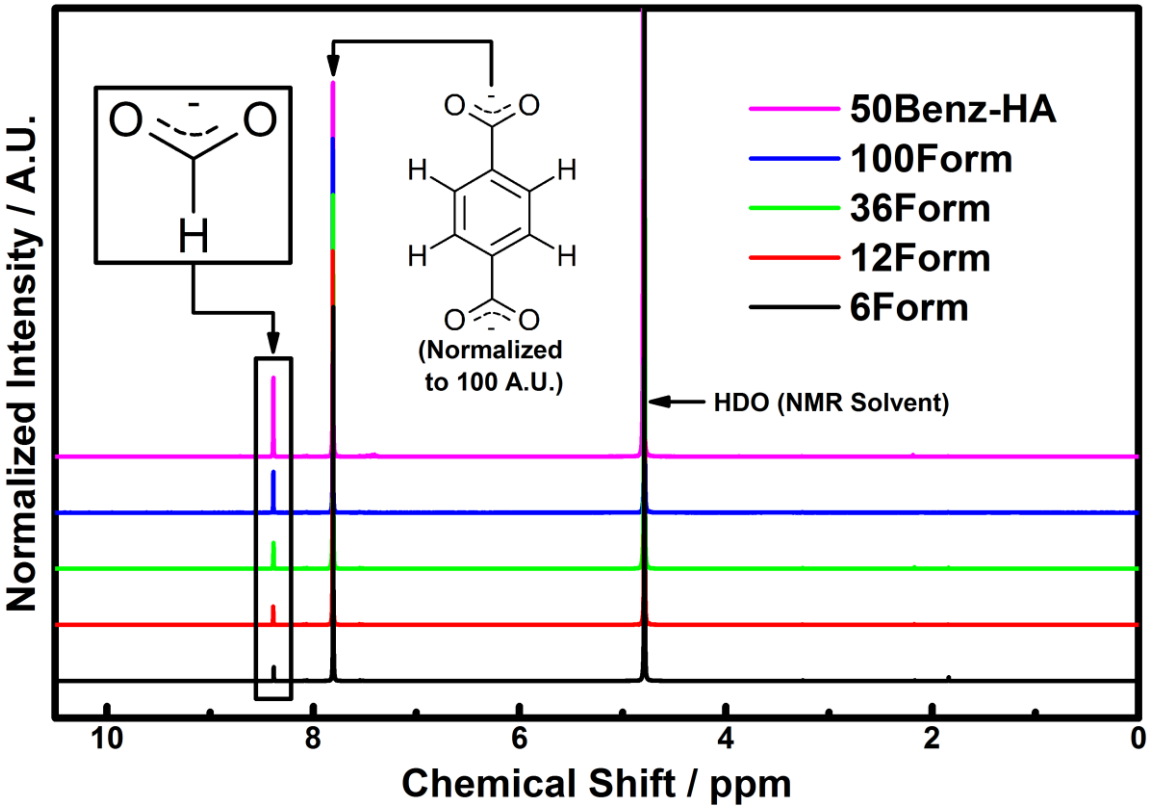

Figure S22. Comparison of the dissolution/^{1}H NMR spectra obtained on 50Benz-HA and the formic acid modulated samples from our previous study.[3]

We have previously demonstrated that monocarboxylate ligands compensate for missing cluster defects in UiO-66 samples synthesized in the presence of monocarboxylic acid modulators under the most typical reaction conditions.[3] The extent of monocarboxylate incorporation (in this case, formate) is therefore strongly correlated with the concentration of missing cluster defects in the sample.[3]

As can be seen in the figure, the formate signal is most intense (by a considerable margin) in the spectrum obtained on 50Benz-HA, suggesting that it contains much more defects than the other samples. This conclusion is quantitatively confirmed in **Table S6**, where the formate to BDC molar ratios $\left(\frac{\mathbf{Form.}}{\mathbf{BDC}}\mathbf{m}_R\right)$ (obtained via integration, see **Section 3.3** for method) are presented:

Table S6. Numerical values of $\frac{\mathbf{Form.}}{\mathbf{BDC}}\mathbf{m}_R$ obtained via integration of the dissolution/^{1}H NMR spectra presented in **Figure S22**.

Sample	$\frac{\mathbf{Form.}}{\mathbf{BDC}}\mathbf{m}_R$
50Benz-HA	0.72
100Form	0.37
36Form	0.24
12Form	0.17
6Form	0.12

As one can see, the $\frac{\mathbf{Form.}}{\mathbf{BDC}}\mathbf{m_R}$ value obtained on 50Benz-HA (0.72) is indeed much higher than those obtained on any of the formic acid modulated samples (its nearest rival is 100Form, whose $\frac{\mathbf{Form.}}{\mathbf{BDC}}\mathbf{m_R}$ value is 0.37). 50Benz-HA is therefore far more defective than any of the formic acid modulated samples. It should also be mentioned that 50Benz-HA contains some benzoate ligands in addition to the formate ligands. The benzoate to BDC molar ratio $\left(\frac{\mathbf{Benz.}}{\mathbf{BDC}}\mathbf{m_R}\right)$ in the sample is 0.04 (as shown in **Section 4.2.1**), bringing its "total modulator to BDC molar ratio" (a.k.a $\frac{\mathbf{Tot.\ Mod.}}{\mathbf{BDC}}\mathbf{m_R}$, see reference 3) to (0.72 + 0.04) = **0.76**. On the other hand, only formate ligands were present in the formic acid modulated samples from our previous study, meaning that their $\frac{\mathbf{Tot.\ Mod.}}{\mathbf{BDC}}\mathbf{m_R}$ values are simply equal to their $\frac{\mathbf{Form.}}{\mathbf{BDC}}\mathbf{m_R}$ values presented in the above table.

4.3.3. ATR-IR

Figure S23 compares the ATR-IR spectrum collected on 50Benz-HA with those obtained on the formic acid modulated samples from our previous study.[3]

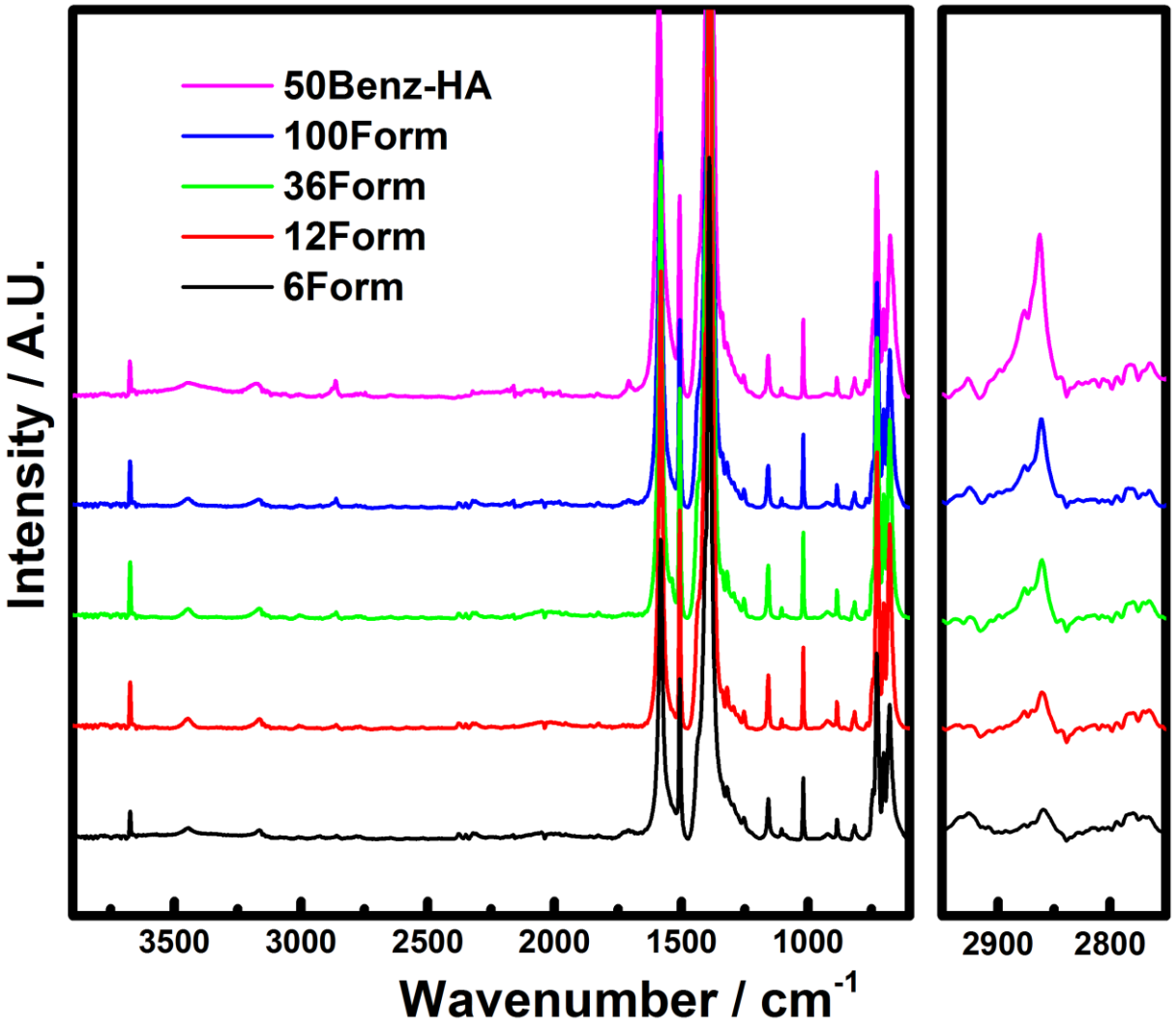

Figure S23. Comparison of the ATR-IR spectra obtained on 50Benz-HA and the formic acid modulated samples from our previous study.[3] Samples were not subjected to vacuum activation for these measurements and thus their pores are filled with water.

As can be seen from the left plot of the above figure, the spectra are very similar overall. However, the intensity of the band at 2861 cm^{-1} (right plot) differs throughout. In our previous study (and **Section 4.2.4** herein), we assigned this band to the C-H stretch of formate ligands. As one can see, it is most intense (by a considerable margin) in the spectrum obtained on 50Benz-HA, providing further evidence that it contains significantly more formate (and is thus much more defective) than the formic acid modulated samples from our previous study.

4.3.4. TGA-DSC

Figure S24 compares the TGA-DSC results collected on 50Benz-HA with those obtained on the formic acid modulated samples from our previous study.[3]

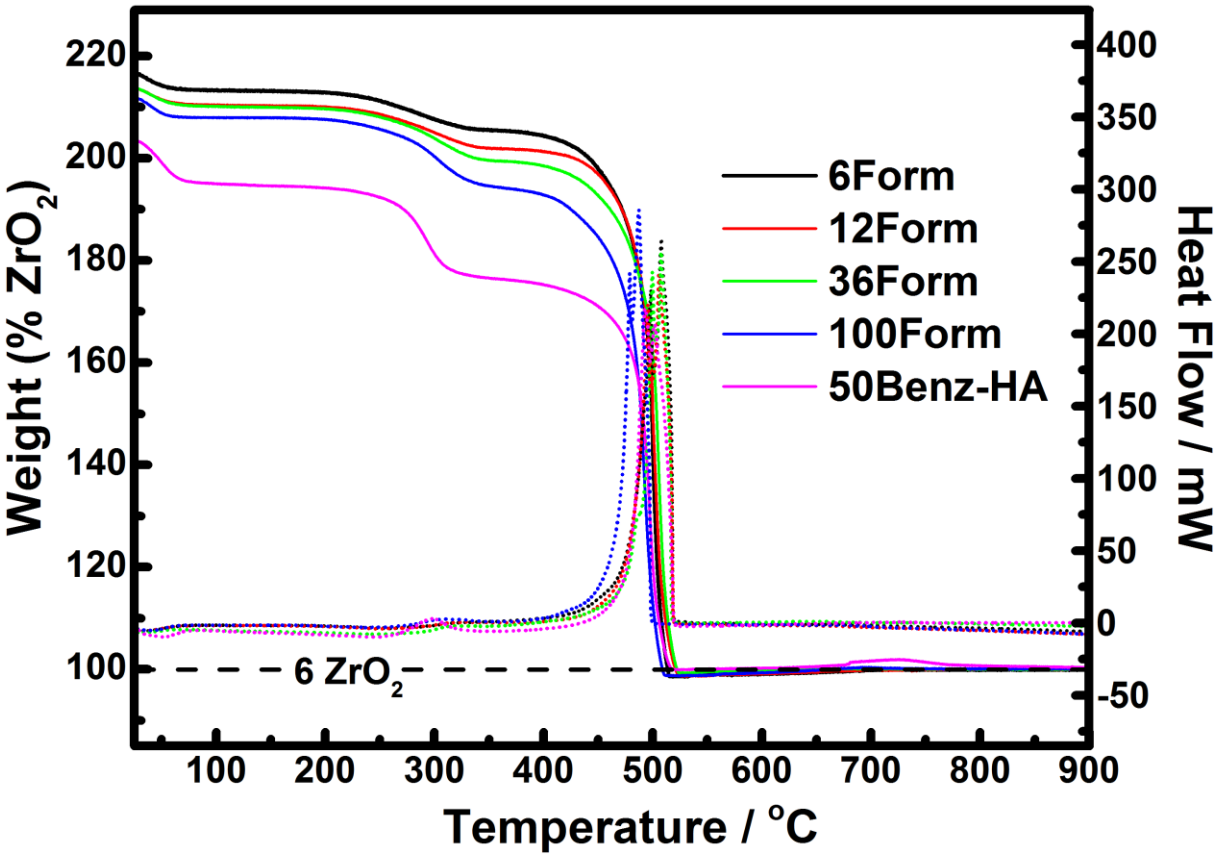

Figure S24. Comparison of the TGA-DSC results obtained on 50Benz-HA and the formic acid modulated samples from our previous study.[3] Solid curves, left axis - TGA traces (normalized such that end weight = 100%). Dotted curve, right axis – DSC traces. Samples were activated (i.e. desolvated) prior to measurement (see **Section 1.2**).

The TGA traces are qualitatively very similar in that they each feature 3 distinct weight loss events:

1) Adsorbate volatilization (in this case H_2O). Temperature range = *ca*. 25-100 °C.
2) Formate loss and dehydroxylation of the inorganic cornerstones. These two weight loss events occur over a similar temperature range (*ca*. 200 - 350 °C) and are thus unresolvable.
3) Framework decomposition (via linker combustion). Temperature range = *ca*. 380-530 °C.

The 2nd and 3rd weight losses give us useful information:

- The normalized magnitude of the 2nd weight loss step is **proportional** to the amount of formate incorporated into the sample.
- The normalized magnitude of the 3nd weight loss step is **inversely proportional** to the number of linker deficiencies per Zr_6 formula unit ($\boldsymbol{x}$) in the sample. Linker deficiencies can originate from both missing linker and missing cluster defects. The value of $\boldsymbol{x}$ is proportional to the overall defectivity of the sample.[3] See **Section 3.4** for more detail on this.

The normalized magnitudes of these weight losses are provided in **Table S7** along with the number of linker deficiencies per Zr_6 formula unit ($\boldsymbol{x}$) in the samples. The $\boldsymbol{x}$ values of the formic acid samples were calculated via the method outlined in the supporting information of our previous study.[3] Due to complications arising from the presence of benzoate ligands (see **Section 3.4.4**), the $\boldsymbol{x}$ value of 50Benz-HA was calculated via an alternative method (exemplified in **Section 3.4.7.2.1**) that is derived and discussed in **Section 3.4**.

Table S7. Quantitative data derived from the TGA traces presented in **Figure S24**.

Sample	**Magnitude of 2nd Weight Loss / %**	**Magnitude of 3rd Weight Loss / %**	$\boldsymbol{x}$
6Form	7.3	105.5	0.73
12Form	8.2	101.9	0.91
36Form	10.1	99.5	1.03
100Form	12.9	94.6	1.28
50Benz-HA	17.7	77.2	2.26

As can be seen from the table:

- The magnitude of the 2nd weight loss is highest in 50Benz-HA, meaning that it contains more formate than the other samples.

- The magnitude of the 3rd weight loss is lowest in 50Benz-HA, meaning that it is more linker deficient (i.e. defective) than the other samples. This is confirmed by the $\boldsymbol{x}$ values: 50Benz-HA has 2.26 linker deficiencies per Zr_6 formula unit, meaning that there are only (12 – (2.26 x 2)) = **7.48** BDC linkers coordinated to its average Zr_6 cluster. This is far less than the 12 linkers expected for the ideal material, emphasizing the incredible defectivity of the sample. With an $\boldsymbol{x}$ value of 1.28 (and thus (12-(1.28 x 2)) = **9.44** BDC linkers coordinated to its average Zr_6 cluster), the most defective formic acid modulated sample (100Form) is much less defective than 50Benz-HA.

4.3.5. Nitrogen Adsorption Isotherms (77 K)

Figure S25 compares the nitrogen adsorption isotherm obtained (at 77 K) on 50Benz-HA with those obtained on the formic acid modulated samples from our previous study.[3]

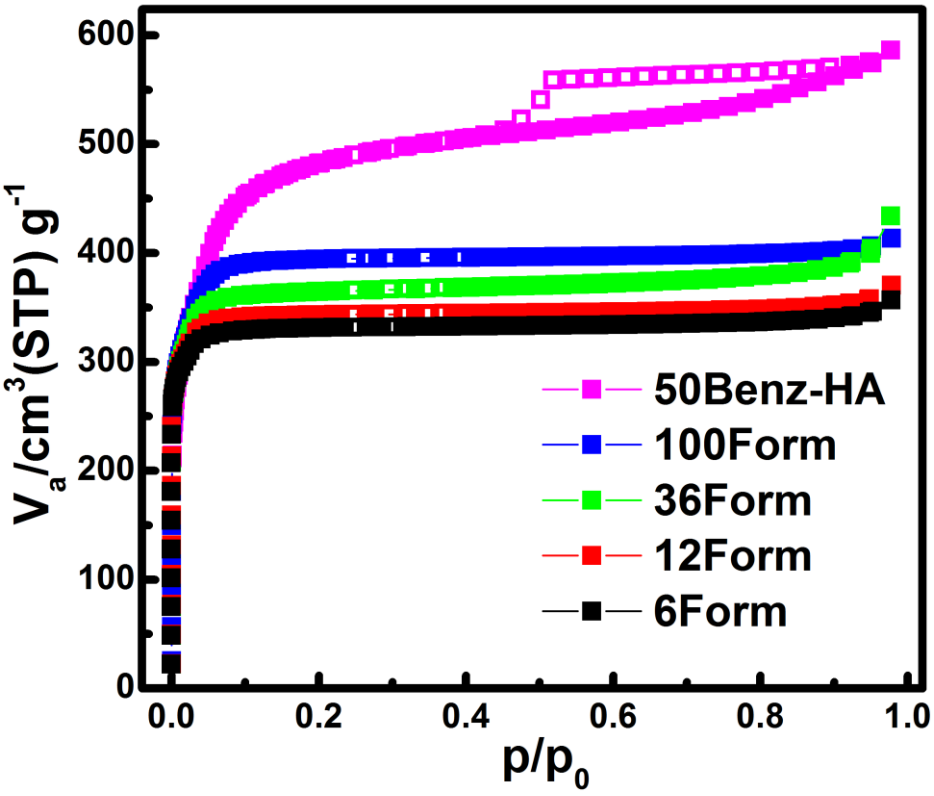

Figure S25. Comparison of the nitrogen adsorption isotherms obtained (at 77 K) on 50Benz-HA and the formic acid modulated samples from our previous study.[3] The adsorption and desorption branches of the isotherm are shown in filled and open squares, respectively.

It is now well established that the porosity of UiO-66 is positively correlated with the concentration of defects in the sample of interest.[3] This is especially true for missing cluster defects. Upon observation of the above figure, one can immediately see that the nitrogen uptake (and thus porosity and defectivity) of 50Benz-HA is far higher than any of the formic acid modulated samples. The same conclusion is reached by comparing the BET surface area (see **Section 3.2** for method) and pore volume values calculated from the isotherms (see **Table S8** below). Another interesting observation is that the isotherm obtained on 50Benz-HA is the only isotherm that features a hysteresis loop, indicating the presence of mesopores in this highly defective sample.

Table S8. BET surface area and pore volume values calculated from the nitrogen adsorption isotherms displayed in **Figure S25**. A detailed description of the method used to obtain the BET surface areas is presented in **Section 3.2**. Pore volumes were calculated at a P/P_0 value of 0.5.

Sample	BET S.A. / m^2g^{-1}	Pore Volume / cm^3g^{-1}
50Benz-HA	1903	0.79
100Form	1645	0.61
36Form	1512	0.57
12Form	1428	0.53
6Form	1372	0.52

Table of Contents

4.4.1. Effect of L-Serine Concentration

The dissolution/^{1}H NMR spectra obtained on the products of the small scale L-Serine PSE reactions performed on 50Benz-HA (at 85 °C, see **Section 1.4** for details) are presented in **Figure S26**:

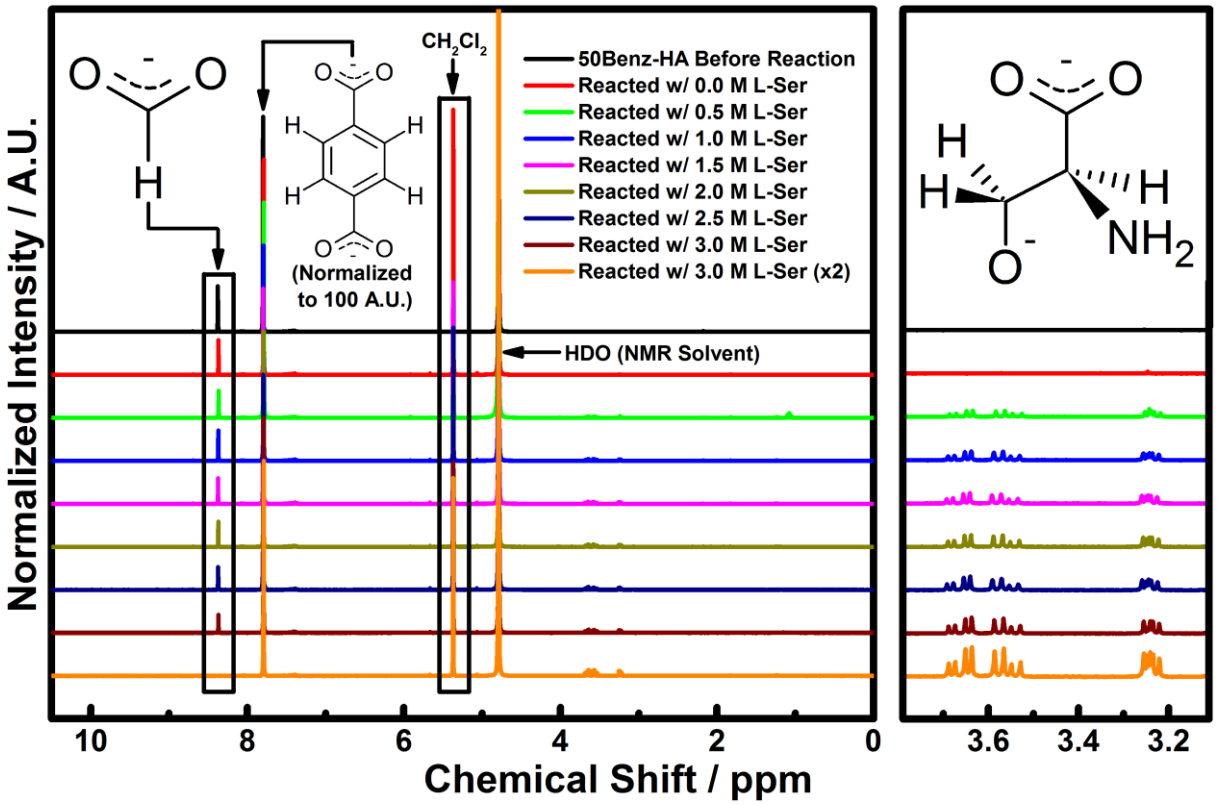

Figure S26. Dissolution/^{1}H NMR spectra obtained on the products of small scale L-Serine PSE reactions performed on 50Benz-HA at 85 °C.

As one can see in the figure, the L-Serine signal (and thus the L-Serine content in the sample) systematically increases in intensity as the molarity of the aqueous (pH = 7) L-Serine solution was increased. The opposite behavior is observed for the formate signal, indicating that the formate ligands exchange with L-Serine.

These results provided confidence that we could obtain samples with different extents of L-Serine functionalization simply by varying the concentration of the L-Serine solution. Seeking four samples whose L-Serine content differed as significantly as possible; we chose to upscale the 0.0, 1.5, 3M, and 3M (x2) reactions (red, magenta, brown, and orange curves, respectively).

4.4.2. Effect of Reaction Temperature

Displayed in **Figure S27** are the dissolution/^{1}H NMR results obtained on 50Benz-HA after performing small scale PSE reactions with a 3M aqueous solution of L-Serine (pH = 7) at 85 °C (black curves) and room temperature (red curves). See **Section 1.4** for full details of the method.

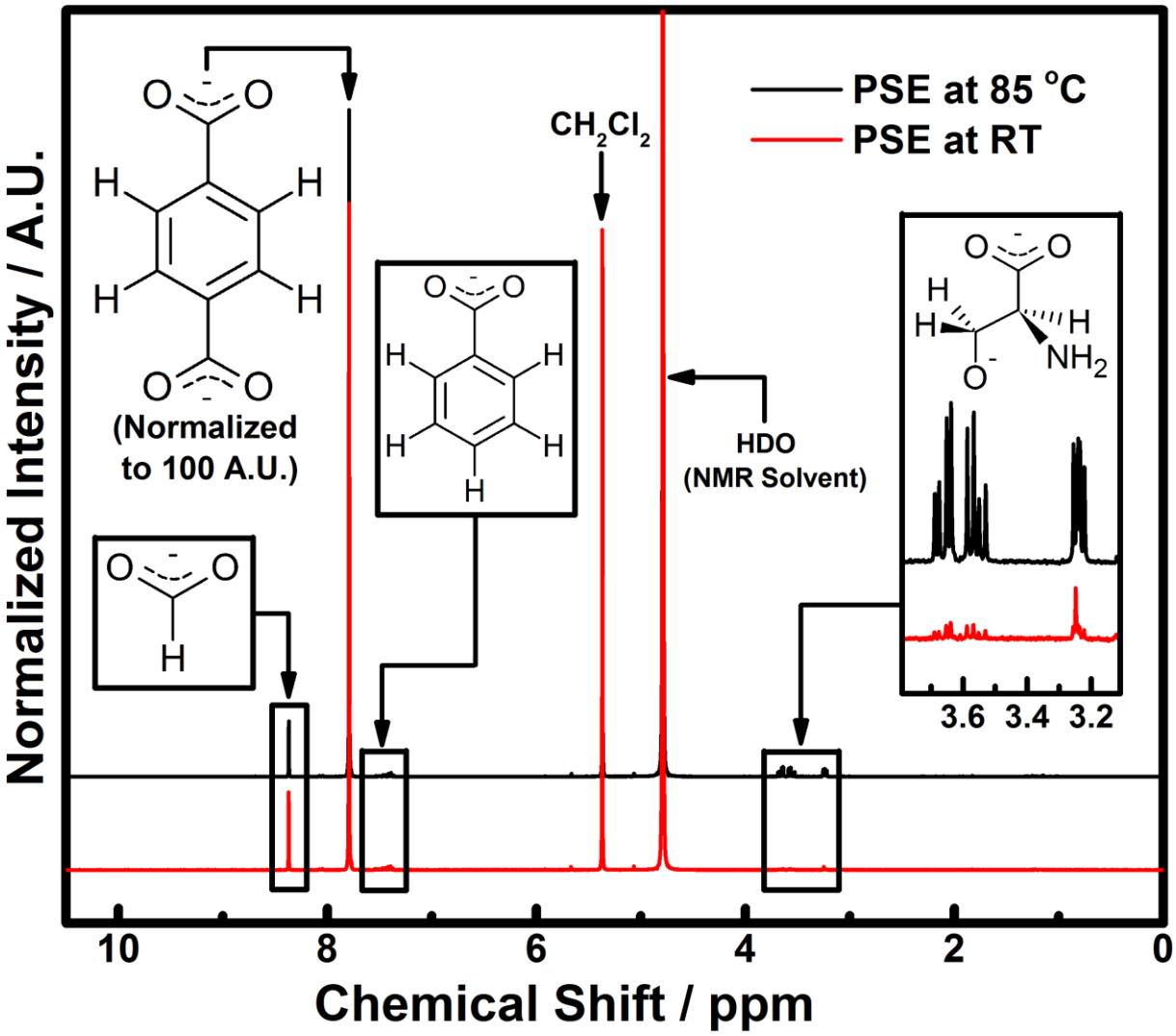

Figure S27. Comparison of the dissolution/^{1}H NMR spectra obtained on 50Benz-HA after performing PSE with a 3M aqueous solution of L-Serine (pH = 7) at two different temperatures; 85 °C (black curves), and room temperature (red curves). The black spectrum is the same as that presented in **Figure S26** (brown curves) and **Figure S28** (black curves).

As can be seen in the figure, the L-Serine signal is very weak in the spectrum obtained on the product of the room temperature PSE reaction, indicating meagre L-Serine incorporation. Indeed, integration (see **Section 3.3**) reveals that the amount of L-Serine incorporated into the framework is essentially negligible (the L-Serine to BDC ratio $\left(\frac{\text{Ser.}}{\text{BDC}}\mathbf{m}_{R}\right)$ in the sample is 0.02). On the other hand, a much more significant amount of L-Serine $\left(\frac{\text{Ser.}}{\text{BDC}}\mathbf{m}_{R}=\mathbf{0.19}\right)$was incorporated when the same reaction was performed at 85 °C.

Such a dramatic temperature effect would not be expected if L-Serine were simply occluded in the pores. This result therefore strongly suggests that L-Serine does indeed react with 50Benz-HA.

4.4.3. Attempts on 50Benz and UiO-66-Ideal

Figure S28 compares the dissolution/^{1}H NMR results obtained on 50Benz-HA, 50Benz, and UiO-66-Ideal after attempting small scale PSE reactions with 3M aqueous (pH = 7) solutions of L-Serine at 85 °C. See **Section 1.4** for full details of the method.

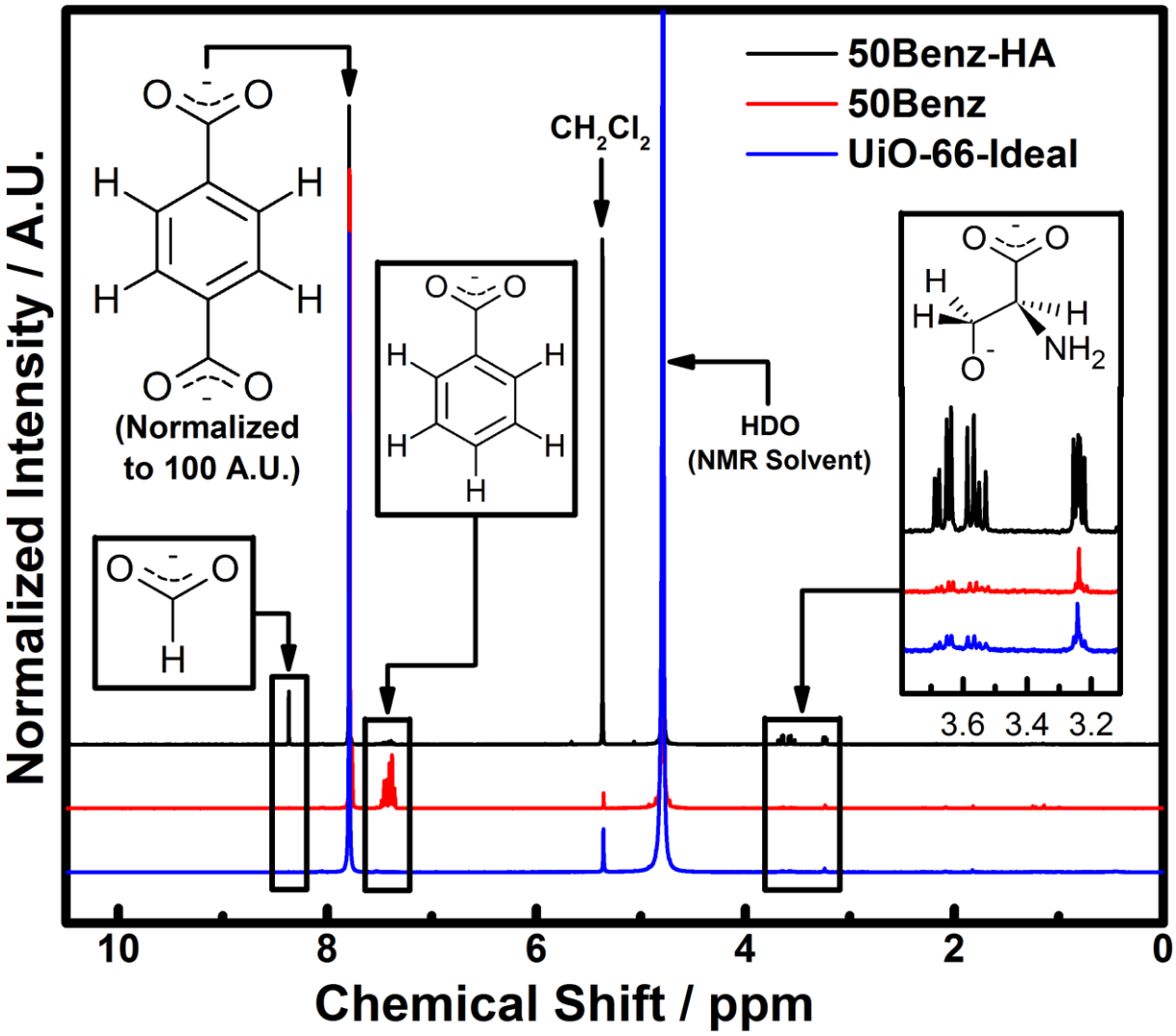

Figure S28. Comparison of the dissolution/^{1}H NMR spectra obtained on 50Benz-HA, 50Benz, and UiO-66-Ideal after attempting PSE with 3M aqueous (pH = 7) solutions of L-Serine at 85 °C. The black spectrum is the same as that presented in **Figure S26** (brown curves) and **Figure S27** (black curves).

As can be seen in the figure, the L-Serine signal is very weak in the spectra obtained on the products of the PSE reactions involving 50Benz or UiO-66-Ideal, indicating meagre L-Serine incorporation. Indeed, integration (see **Section 3.3**) reveals that the amount of L-Serine incorporated into either sample is essentially negligible (the L-Serine to BDC ratio $\left(\frac{\text{Ser.}}{\text{BDC}}\mathbf{m}_{R}\right)$ in each sample is a paltry 0.02).

On the other hand, a much more significant amount of L-Serine $\left(\frac{\text{Ser.}}{\text{BDC}}\mathbf{m}_{R} = \mathbf{0.19}\right)$ was incorporated into 50Benz-HA under the very same reaction conditions. This result emphasizes the incredible extent to which defects (and the identity of their compensating ligands) can affect the reactivity of UiO-66 towards PSE.

4.5. Characterization of the Large Scale L-Serine PSE Products

Table of Contents

4.5.1. Formate/L-Serine Ligand Exchange: Molar Ratios from Dissolution / ^{1}H NMR

Figure S29 graphically depicts how L-Serine PSE affects $\frac{\text{Form.}}{\text{BDC}}\mathbf{m}_R$ and $\frac{\text{Ser.}}{\text{BDC}}\mathbf{m}_R$ (the formate/BDC and the L-Serine/BDC molar ratio, respectively). The values (presented in **Table S9**, along with the numerical values of the ^{1}H NMR integrals relevant to their calculation) were obtained via integration of the dissolution/^{1}H NMR spectra shown in **Figure 5** (main article). See **Section 3.3** for details of the method.

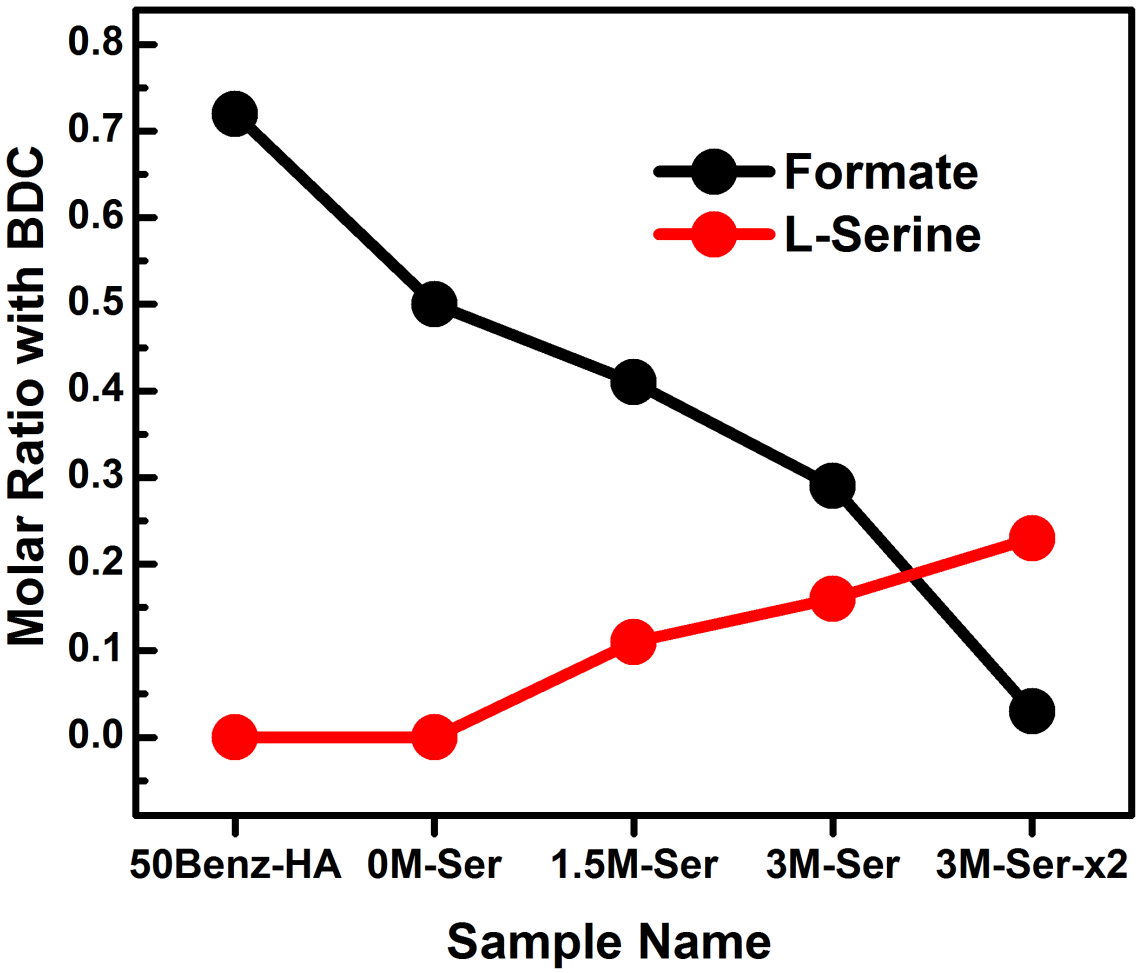

Figure S29. Graphical depiction of the formate to BDC $\left(\frac{\text{form.}}{\text{BDC}}\mathbf{m}_R\right)$ and L-Serine to BDC $\left(\frac{\text{Ser.}}{\text{BDC}}\mathbf{m}_R\right)$ molar ratios in the samples relevant to the large scale L-Serine PSE reactions.

As one can see from the figure and table (PTO), the formate/L-Serine content in the samples systematically decreased/increased as we increased the concentration of the L-Serine solution used for PSE. However, the decline in formate content is significantly steeper than the corresponding increase in L-Serine content, indicating that the exchange between formate and L-Serine is not stoichiometric. Some formate must therefore be lost by a different mechanism, e.g. hydrolysis. Indeed, one can see that the formate content decreases significantly even after PSE in pure (pH = 7) water (0M-Ser). This partial removal of formate is also clearly observed in TGA-DSC results (see **Figure S31**). However, it must be said that we do not have any direct evidence for formate hydrolysis, which would be expected to yield terminal H_2O and OH^- ligands,[2, 21] and thus (probably) the appearance of new ν(OH) bands in the ATR-IR spectra. However, no such new bands are observed in our ATR-IR spectra (see **Figure S35**).

Table S9. Quantitative data extracted from the dissolution/^{1}H NMR spectra on the samples relevant to the large scale L-Serine PSE reactions. The meaning of these values (and the method with which they were obtained) is outlined in **Section 3.3.**

Sample	$(\mathbf{BDC} + \mathbf{Benz.H_a})$ Int.	$\mathbf{Benz.H_b}$ Int.	Form. Int.	$\mathbf{Ser.H_a}$ Int.	$\frac{\mathbf{Form.}}{\mathbf{BDC}}\mathbf{m}_R$ †	$\frac{\mathbf{Ser.}}{\mathbf{BDC}}\mathbf{m}_R$ ‡
50Benz-HA	6.00*	0.12	1.06	0	0.72	0.00
0M-Ser	6.00*	0.12	0.74	0	0.50	0.00
1.5M-Ser	6.00*	0.12	0.61	0.31	0.41	0.11
3M-Ser	6.00*	0.11	0.42	0.46	0.29	0.16
3M-Ser-x2	6.00*	0.11	0.05	0.67	0.03	0.23

* The$(\mathbf{BDC} + \mathbf{Benz.H_a})$ signal was integrated and its numerical value normalized to 6.00 prior to all further integration.

† Calculated by **Equation (18)**, derived in **Section 3.3.4**.

‡ Calculated by **Equation (20)**, derived in **Section 3.3.4**.

4.5.2. PXRD: Crystallinity and Defectivity

Figure S30 compares the PXRD results obtained on the samples relevant to the large scale L-Serine PSE reactions:

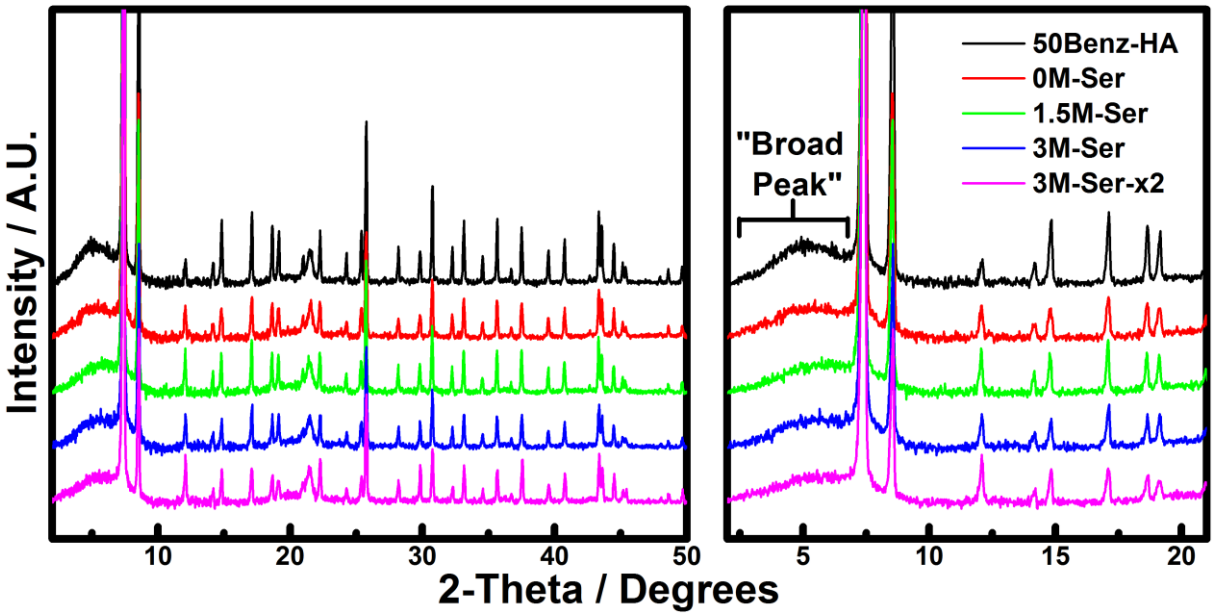

Figure S30. Comparison of the PXRD patterns obtained on the samples relevant to the large scale L-Serine PSE reactions. The same y-Scale is applied to both plots.

As one can see from the overall patterns (left plot in figure), the crystallinity of the material is completely preserved after all PSE reactions. Moreover, the intensity of the "broad peak" (emphasized in the right plot) does not appear to change significantly, indicating that the high concentration of missing cluster defects is preserved (see Sections **4.1.1**, **4.2.2**, and **4.3.1** for more details on this).

4.5.3. TGA-DSC

Figure S31 compares the TGA-DSC results obtained before (50Benz-HA) and after (0M-Ser) PSE (at 85 °C) with pure water (pH = 7) in the absence of L-Serine:

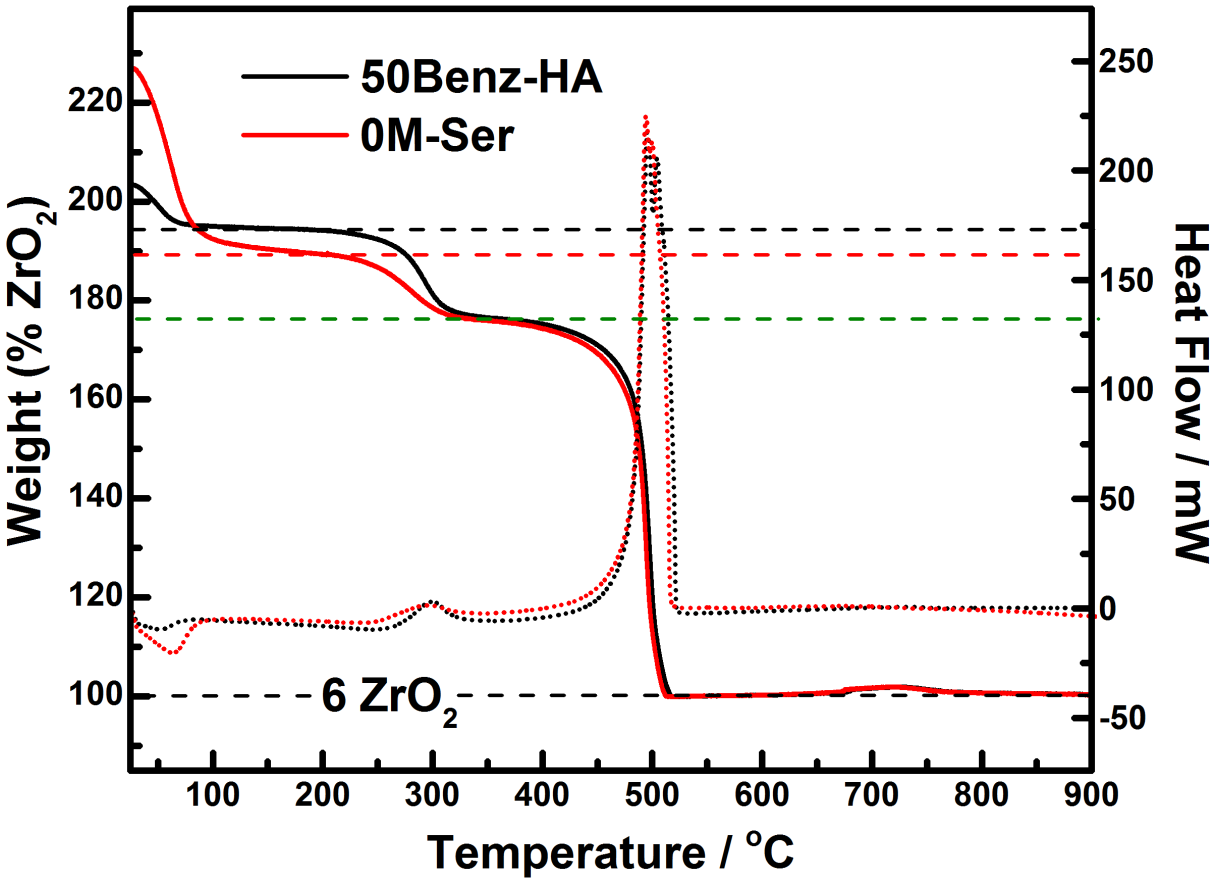

Figure S31. Comparison of the TGA-DSC results obtained before (50Benz-HA) and after (0M-Ser) PSE (at 85 °C) with pure water. Solid curves, left axis - TGA traces (normalized such that end weight = 100%). Dotted curve, right axis – DSC traces.

As can be seen, the results are very similar, especially at temperatures of 350 °C and upwards, where it is clear that the (normalized) magnitude of the final weight loss is identical. This tells us that the PSE reaction did not alter the defectivity of the material (see **Section 4.3.4** for more on this).

However, there are differences in the (normalized) magnitudes of the weight losses observed at lower temperatures:

- The magnitude of the first weight loss (due to adsorbate volatilization, see **Section 3.4.4**) is significantly larger in 0M-Ser. This due to the fact that 0M-Ser is filled with dichloromethane, which is a much heavier molecule (M.W. = 84.93 g mol^{-1}) than water (M.W. = 18.02 g mol^{-1}), which fills the pores of 50Benz-HA.

- The magnitude of the second weight loss (due to dehydroxylation and formate loss, see **Section 3.4.4**) is reduced in 0M-Ser. This strongly implies that the extent of formate incorporation was slightly diminished by PSE, as shown more directly by dissolution/^{1}H NMR (see **Figure 5** (main article) and **Section 4.5.1**).

Figure S32 compares the TGA-DSC results obtained on the L-Serine functionalized samples. The result obtained on 0M-Ser is included for further comparison.

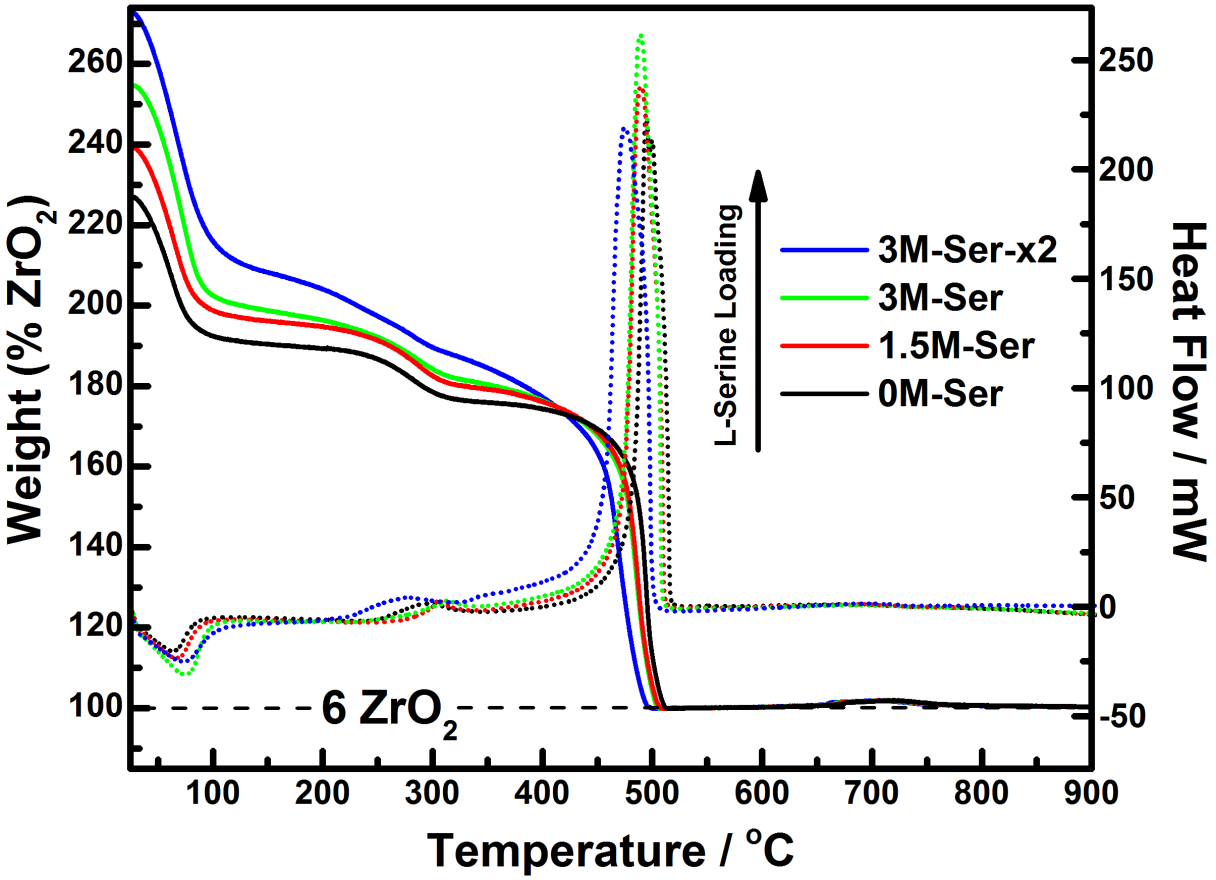

Figure S32. Comparison of the TGA-DSC results obtained on the L-Serine functionalized samples. The result obtained on 0M-Ser is included for further comparison. Solid curves, left axis - TGA traces (normalized such that end weight = 100%). Dotted curve, right axis – DSC traces.

As one can see, the TGA traces are similar overall. However, it is clear that the weight of the framework systematically increases with increasing L-Serine loading. This increase in framework weight is observed all the way until the decomposition of the material, suggesting that L-Serine (or a decomposition product thereof) is not removed until the framework collapses. This makes it difficult to use this data to accurately compare the defectivity of the samples, which is usually done on the assumption that the final weight loss is purely due to combustion of the BDC linkers (see **Section 3.4.3**). Nevertheless, given the overall similarity of the results, one can reasonably assume that all of the materials are of similar defectivity, and thus that the PSE reactions did not induce the formation of additional defects.

4.5.4. Nitrogen Adsorption Isotherms (77 K)

Figure S33 compares the simulated and experimental nitrogen adsorption isotherms (obtained at 77 K) of relevance to the large scale L-Serine PSE reactions:

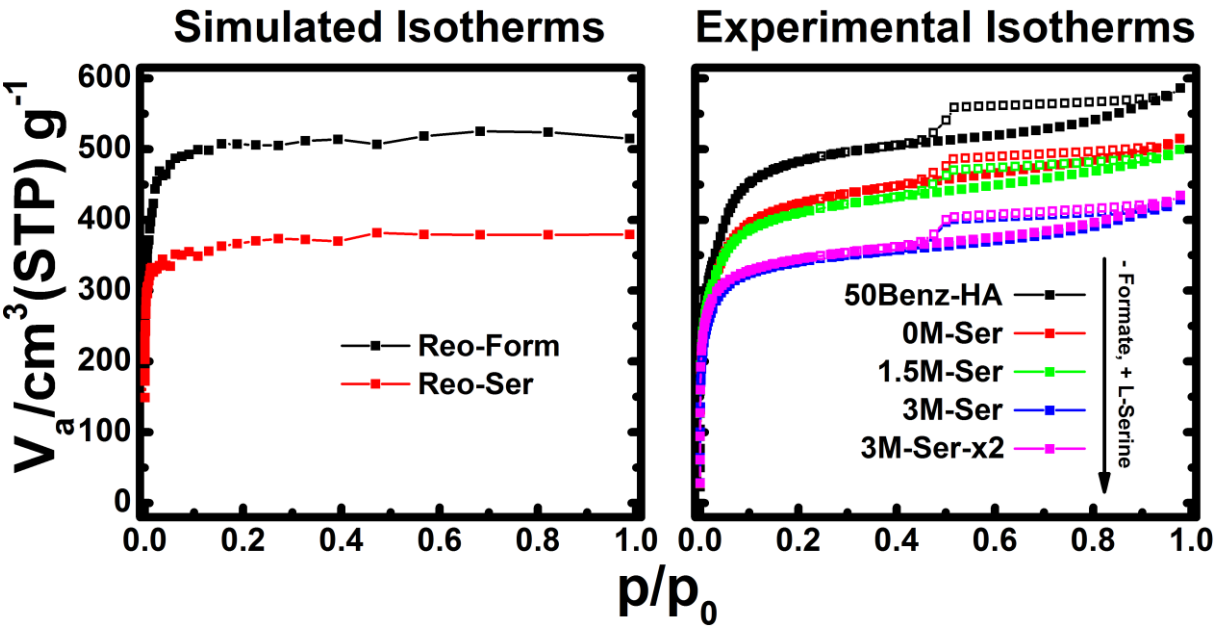

Figure S33. Comparison of simulated and experimental nitrogen adsorption isotherms (obtained at 77 K) of relevance to the large scale L-Serine PSE reactions. The simulated isotherms were obtained from the hypothetical model structures shown over the page in **Figure S34**. The adsorption and desorption branches of the experimental isotherms are shown in filled and open squares, respectively. The same y-Scale is applied to both plots.

Focusing first on the experimentally obtained isotherms (right plot), one can see that the nitrogen uptake (and hence, porosity) of the material systematically decreases as the extent of L-Serine functionalization increases. This behavior can be fully explained by the simulated isotherms (left plot), as discussed in the following paragraph:

Our multi-technique characterization results (see **Section 4.2**) have shown that 50Benz-HA contains a high concentration of missing cluster defects compensated by formate ligands. This is ultimately validated by the fact that its nitrogen adsorption isotherm matches very well with that simulated from Reo-Form, a hypothetical structural model in which formate ligands compensate for a high concentration of missing cluster defects (one defect per unit cell = 1 out of every 4 clusters missing). The model is illustrated in **Figure S34**. As shown by our dissolution/^{1}H NMR results (see **Section 4.5.1** and **Figure 5** in main article), 50Benz-HA's formate ligands are partially exchanged for L-Serine ligands after PSE. We thus constructed Reo-Ser (see **Figure S34**), a hypothetical defective structural model which is equivalent to Reo-Form, albeit with L-Serine as the defect compensating ligand. By assessing the nitrogen uptake in the isotherms above, one can clearly see that Reo-Ser is significantly less porous than Reo-Form, an observation which can be explained by the fact that L-Serine ligands are heavier and bulkier than formate ligands. When comparing these simulated isotherms with those experimentally obtained, one can see that the nitrogen uptake (and hence, porosity) of all the samples is within the range spanned by the 2 simulated isotherms. Ultimately, this indicates that the systematic decrease in the porosity of the PSE products can be fully explained by the proposed ligand exchange chemistry.

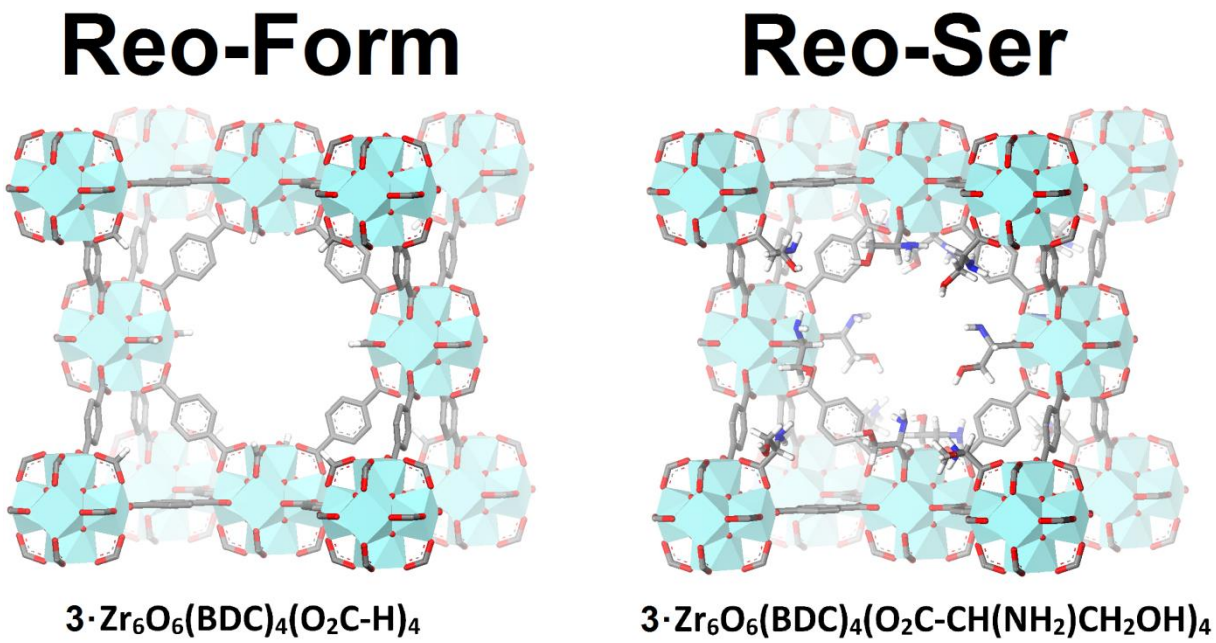

Figure S34. Hypothetical structural models used to simulate the isotherms shown in **Figure S33**. Both models contain one missing cluster defect per unit cell. The models differ only by the ligands which compensate for the defects (formate in Reo-Form and L-Serine in Reo-Ser). Reo-Form and Reo-Ser can also be seen in **Figures 4** and **1** in the main article, respectively.

The BET surface area and pore volume values calculated from all the simulated and experimental nitrogen adsorption isotherms of relevance to this work are provided below in **Table S10** and **Table S11**, respectively. The method used to calculate the BET surface area is detailed in **Section 3.2**.

Table S10. BET surface area and pore volume values calculated from the simulated nitrogen adsorption isotherms (see **Figure 3** in the main article and **Figure S33** herein). A detailed description of the method used to obtain the BET surface areas is presented in **Section 3.2**. Pore volumes were calculated at a P/P_0 value of 0.5.

Isotherm	BET S.A. / m^2g^{-1}	Pore Volume / cm^3g^{-1}
Reo-Benz*	1532	0.58
Reo-Form†	2104	0.78
Reo-Ser†	1441	0.59

* An illustration of this structural model can be found in **Figure 4** in the main article.
† An illustration of this structural model can be found in **Figure S34** above.

Table S11. BET surface are and pore volume values calculated from the experimental nitrogen adsorption isotherms (see **Figure 3** in the main article and **Figure S33** herein). A detailed description of the method used to obtain the BET surface areas is presented in **Section 3.2**. Pore volumes were calculated at a P/P_0 value of 0.5.

Sample	BET S.A. / m^2g^{-1}	Pore Volume / cm^3g^{-1}
50Benz*	1515	0.62
50Benz-HA	1903	0.79
0M-Ser	1664	0.71
1.5M-Ser	1619	0.68
3M-Ser	1347	0.56
3M-Ser-x2	1335	0.57

* Isotherm shown in **Figure 3** in the main article.

4.5.5. ATR-IR

Figure S35 compares the ATR-IR spectra obtained on the samples of relevance to the large scale L-Serine PSE reactions:

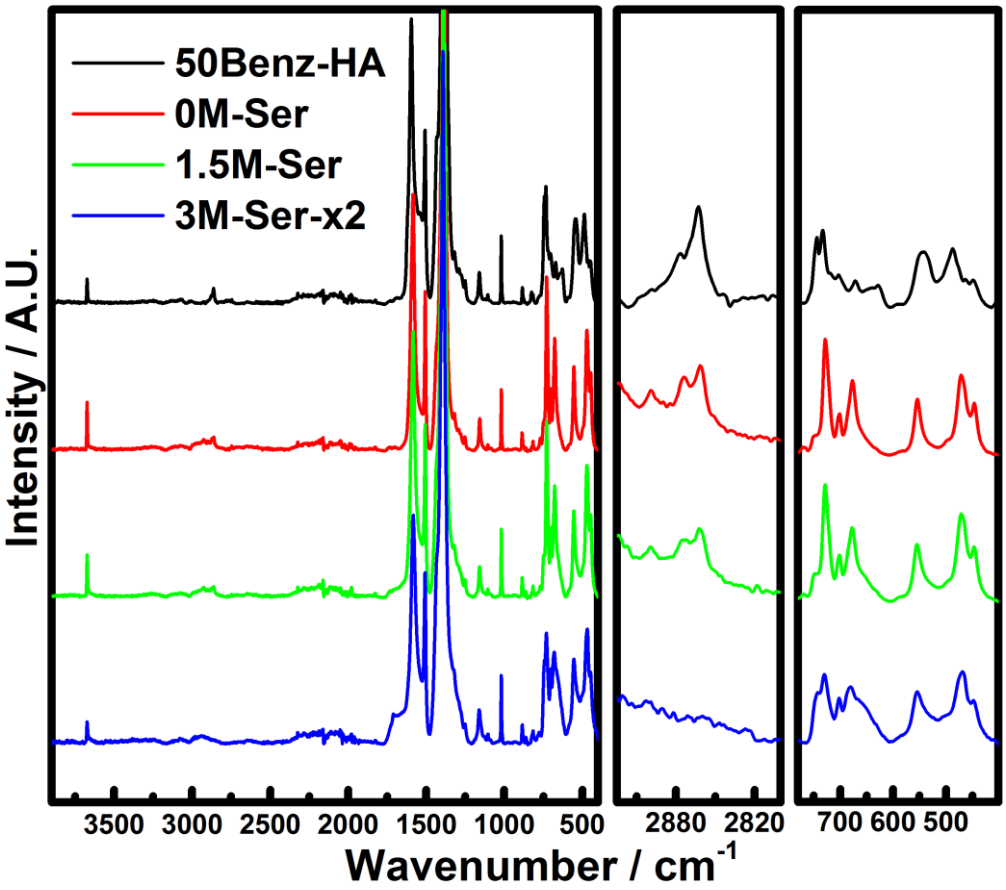

Figure S35. Comparison of the ATR-IR spectra obtained on the samples of relevance to the large scale L-Serine PSE reactions. Samples were activated (i.e. desolvated) by simultaneous vacuum and heat treatment (see **Table S1**) before being transferred to a glovebox (N_2 atmosphere) for measurement.

As can be seen from the figure, the overall spectra (left plot) are very similar. However, one can clearly see that the formate ν(C-H) band (2861 cm^{-1}, middle plot, see **Section 4.2.4** for more on this) systematically decreases in intensity as the extent of L-Serine functionalization increases, mirroring the observations in our dissolution/^{1}H NMR data (see **Figure 5** (main article) and **Section 4.5.1**) and further evidencing the gradual removal of formate ligands. Further differences can be observed in the low frequency region of the spectra (right plot). However, we cannot definitively assign these differences at this time.

One may have expected new bands related to L-Serine to appear in the spectra upon functionalization, but this is not the case. An explanation for this can be arrived at by revisiting results from our previous study.[3] Therein, we found that no acetate related bands were present in the ATR-IR spectra obtained on the acetic acid modulated samples (see **Figure S56** in our previous study[3]), despite the fact that acetate was clearly present in their dissolution/^{1}H NMR spectra (see **Figure S15** in our previous study[3]).We attributed this to the relatively low acetate loading in the samples. The L-Serine content in the samples herein is similar to the acetate content in the acetic acid modulated samples from our previous study, and thus it may simply be that the L-Serine loading in our samples is too low for detection by ATR-IR.

4.5.6. SEM

The SEM images obtained on all of the samples studied in this work are presented in **Figure S36**:

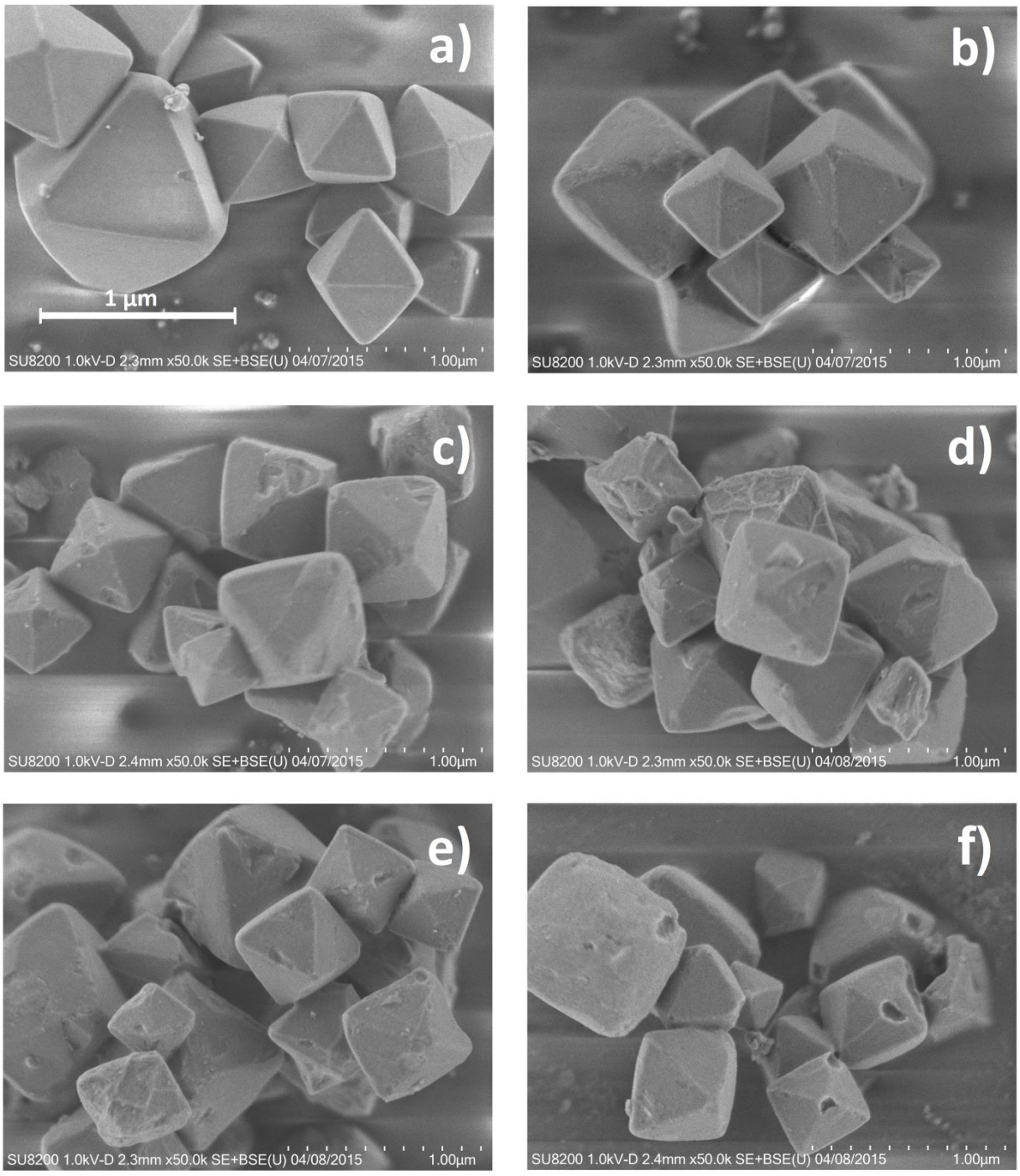

Figure S36. SEM images obtained on: a) 50Benz, b) 50Benz-HA, c) 0M-Ser, d) 1.5M-Ser, e) 3M-Ser, and f) 3M-Serx2. All images are presented at the same magnification level (see scale bar).

As can be seen, the crystals maintain their size and octahedral morphology after all post synthetic treatments. However, it is clear that they are partially eroded by the PSE reactions. This is perhaps unsurprising given that the treatments imposed on the samples were rather harsh (extensive ultrasonic and heat treatment in the presence of concentrated aqueous solutions). Nevertheless, our PXRD results show that the PSE reactions barely affected the crystallinity of the material (see **Section 4.5.2**).

4.6. CO_2 Capture Performance

Table of Contents

4.6.1. CO_2 Isotherms and Langmuir Fits Thereof

All CO_2 adsorption isotherms (scatter points) and Langmuir fits thereof (solid lines) are displayed in **Figure S37**. The isotherms obtained at 25 °C (298.15 K) and 40 °C (313.15 K) are displayed in part a) and b) of the figure, respectively.

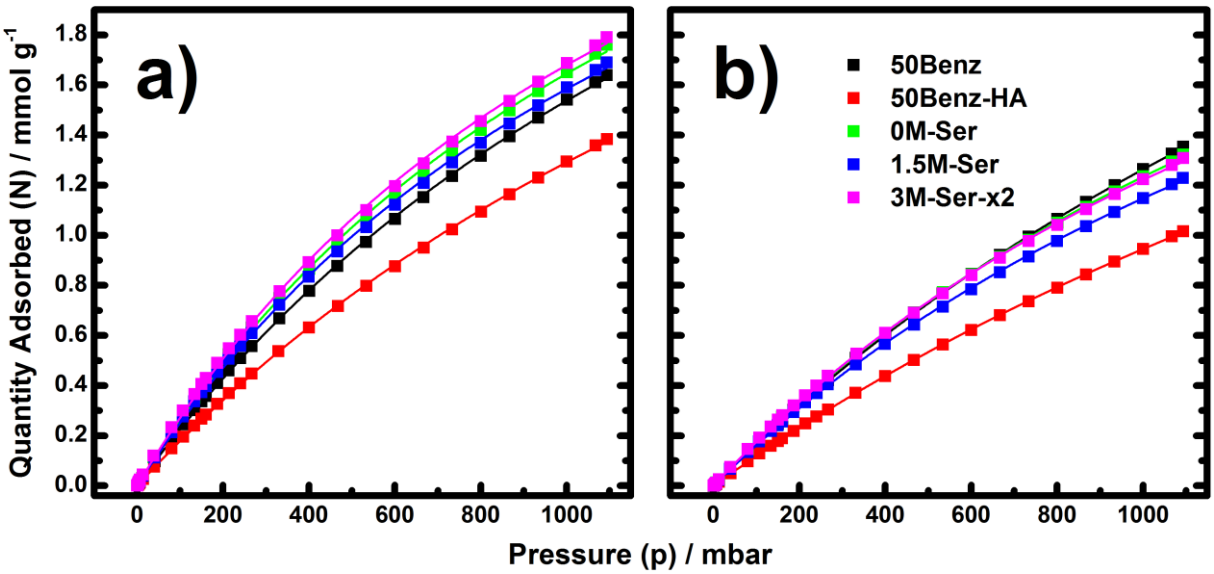

Figure S37. CO_2 adsorption isotherms obtained at a) 25 °C (298.15 K) and b) 40 °C (313.15 K). The scatter points represent the experimental data while the Langmuir fits are displayed with a solid line. The same y-Scale and legend is adopted in both plots.

As can be seen, all samples perform very similarly in terms of CO_2 uptake, except 50Benz-HA, which adsorbs significantly less CO_2. One can also see that the Langmuir fits (solid lines) are a very good match to the experimental data (scatter points). The $\mathbf{N_{Sat}}$ and **k** parameter values obtained from these fits are presented in **Table S12** below:

Table S12. Parameter values ($\mathbf{N_{Sat}}$ and **k**) obtained from the Langmuir fits of the CO_2 adsorption isotherms presented in **Figure S37**. The equation for the Langmuir model (in which $\mathbf{N_{Sat}}$ and **k** feature) is provided in **Section 2.11**.

	Temperature = 25 °C		**Temperature = 40 °C**	
Sample	$\mathbf{N_{Sat}}$ (mmol·g^{-1})	**k** (mbar^{-1} x10^{-4})	$\mathbf{N_{Sat}}$ (mmol·g^{-1})	**k** (mbar^{-1} x10^{-4})
50Benz	4.35573	5.45555	4.74939	3.62378
50Benz-HA	4.22171	4.40844	4.12279	2.97515
0M-Ser	4.06647	6.79753	3.85278	4.71163
1.5M-Ser	3.88191	6.89558	3.56541	4.74704
3M-Ser-x2	3.97370	7.32232	3.60328	5.12671

4.6.2. Nitrogen Adsorption Isotherms Obtained at 40 °C (313.15 K) and Langmuir Fits Thereof

All of the nitrogen adsorption isotherms acquired at 40 °C (scatter points) and the Langmuir fits thereof (solid lines) are displayed in **Figure S38**:

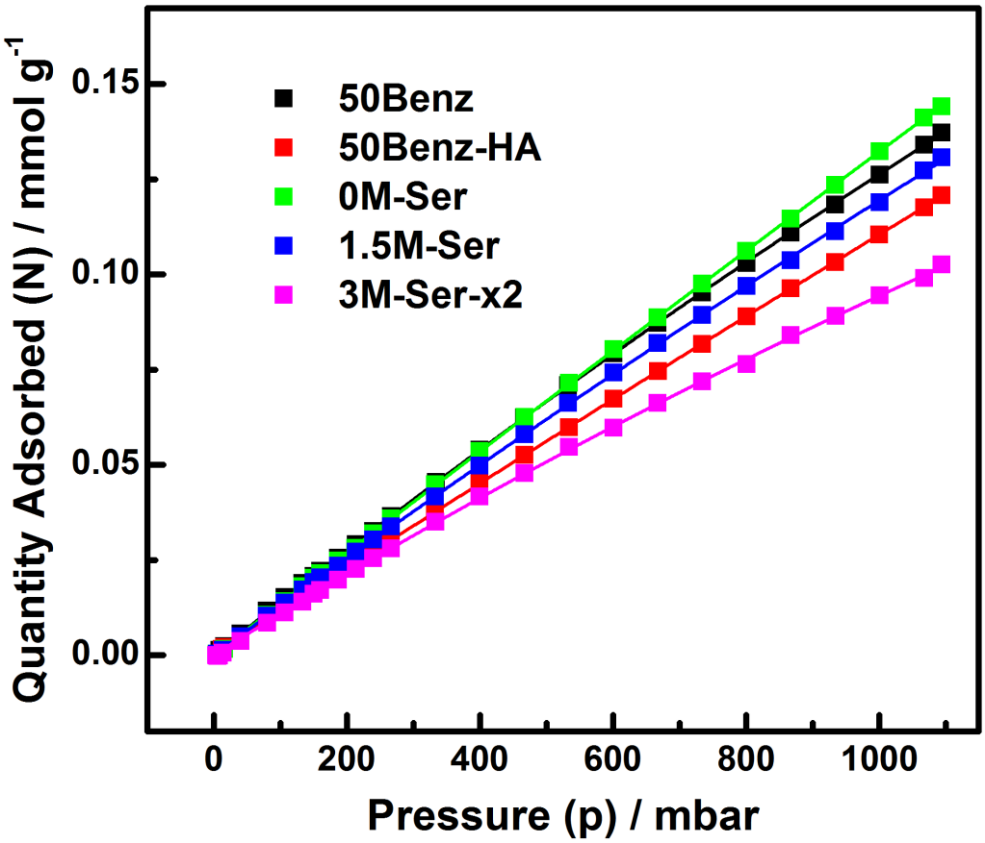

Figure S38. Nitrogen adsorption isotherms obtained at 40 °C (313.15 K). The scatter points represent the experimental data while the Langmuir fits are displayed with a solid line.

As can be seen, there is no obvious trend amongst the isotherms. One can also see that the Langmuir fits (solid lines) are a very good match to the experimental data (scatter points). The $\mathbf{N_{Sat}}$ and **k** parameter values obtained from these fits are presented in **Table S13** below:

Table S13. Parameter values ($\mathbf{N_{Sat}}$ and **k**) obtained from the Langmuir fits of the N_2 adsorption isotherms presented in **Figure S38**. The equation for the Langmuir model (in which $\mathbf{N_{Sat}}$ and **k** feature) is provided in **Section 2.11**.

Sample	$\mathbf{N_{Sat}}$ (mmol·g^{-1})	**k** (mbar^{-1} x10^{-4})
50Benz	1.20869	1.16706
50Benz-HA	3.22018	0.35534
0M-Ser	6.93967	0.19432
1.5M-Ser	1.66185	0.77461
3M-Ser-x2	0.66793	1.64602

4.6.3. Summary Table

The key CO_2 capture performance parameters of our UiO-66 samples are summarized in **Table S14**:

Table S14. Summary of the CO_2 capture performance of the UiO-66 samples investigated herein.

Sample	**CO_2 Adsorption Capacity** (mmol·g^{-1})*	**S_{CO_2/N_2}** †	**Q_{iso} (kJ·mol^{-1})** ‡
50Benz	1.64	13.6	16.7
50Benz-HA	1.38	10.8	21.6
0M-Ser	1.76	13.2	21.8
1.5M-Ser	1.69	13.9	23.7
3M-Ser-x2	1.79	20.7	23.5

* CO_2 uptake at 1100 mbar in the isotherms obtained at 25 °C (see **Figure S37**).

† CO_2/N_2 selectivity under flue gas conditions. Values were calculated by the method outlined in **Section 3.5**.

‡ Isosteric heat of CO_2 adsorption. Values were calculated by the method outlined in **Section 3.6**.

As one can see, $\mathbf{S_{CO_2/N_2}}$ increases systematically with the extent of L-serine functionalization. However, the value is still rather modest even at the highest L-serine loading (3M-Ser-x2). Moreover, the CO_2 adsorption capacities and $\mathbf{Q_{iso}}$ values vary very little amongst the samples. The CO_2 capture performance of our monoethanolamine functionalized materials is thus not as good as was hoped. However, this is actually not all that surprising – marginal gains in CO_2 adsorption capacity were also observed in previous work on UiO-66 samples with a similar degree of amine functionalization (with ABDC = 2-aminobenzene-1,4-dicarboxylic acid).[22] We suggest that very high amine loadings are required to significantly enhance the CO_2 capture performance of MOFs.

5. Appendix

Table of Contents

5.1. PXRD Before and After Activation and Nitrogen Sorption Measurements

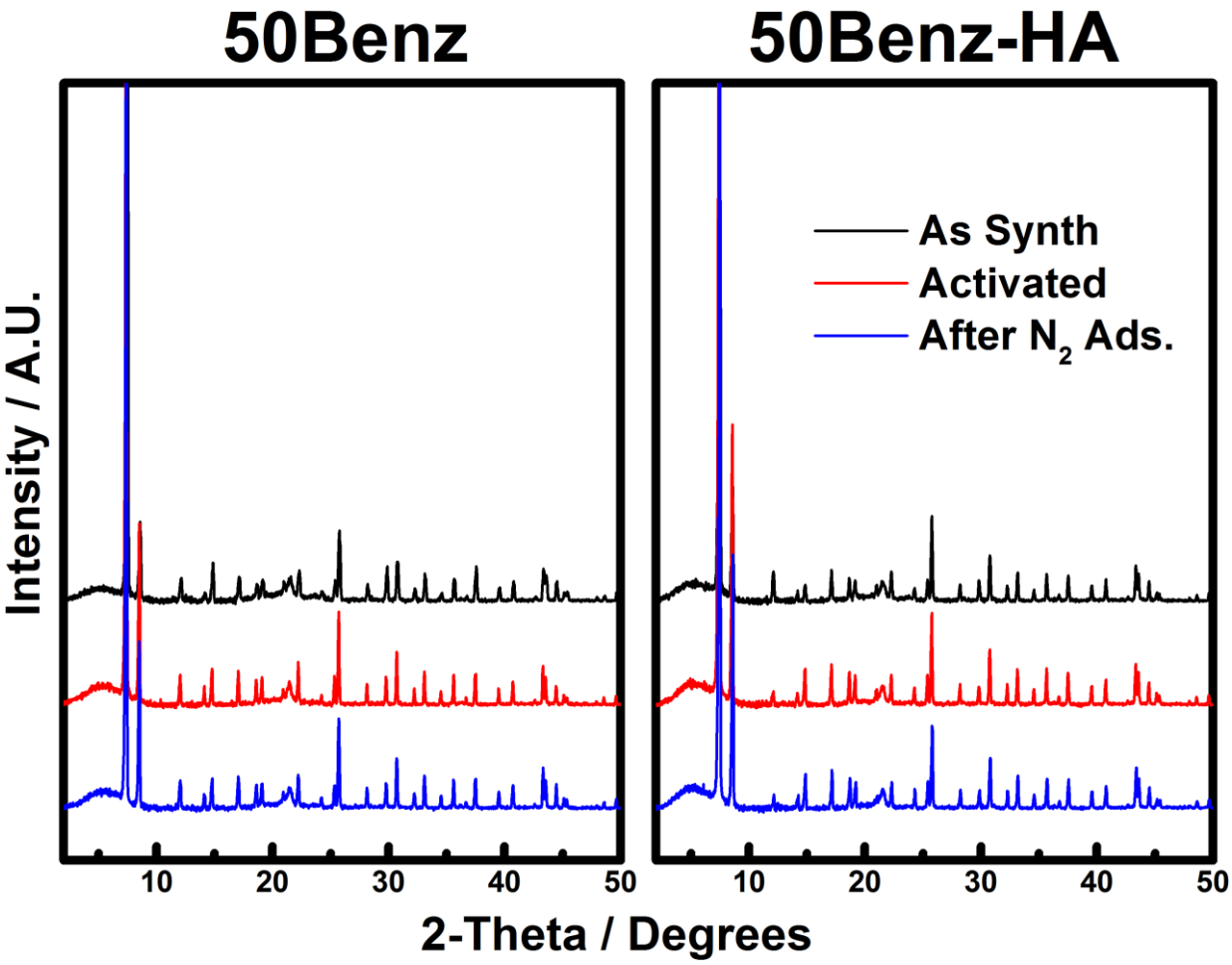

Figure S39. PXRD patterns obtained before (as synth) and after activation (at 200 °C, see Sections **1.1** and **1.2**) and nitrogen sorption measurements: 50Benz (left plot) and 50Benz-HA (right plot). This figure demonstrates that both samples were completely intact after all treatments. See **Table S1** for details of the pretreatment methods used before the nitrogen adsorption measurements.

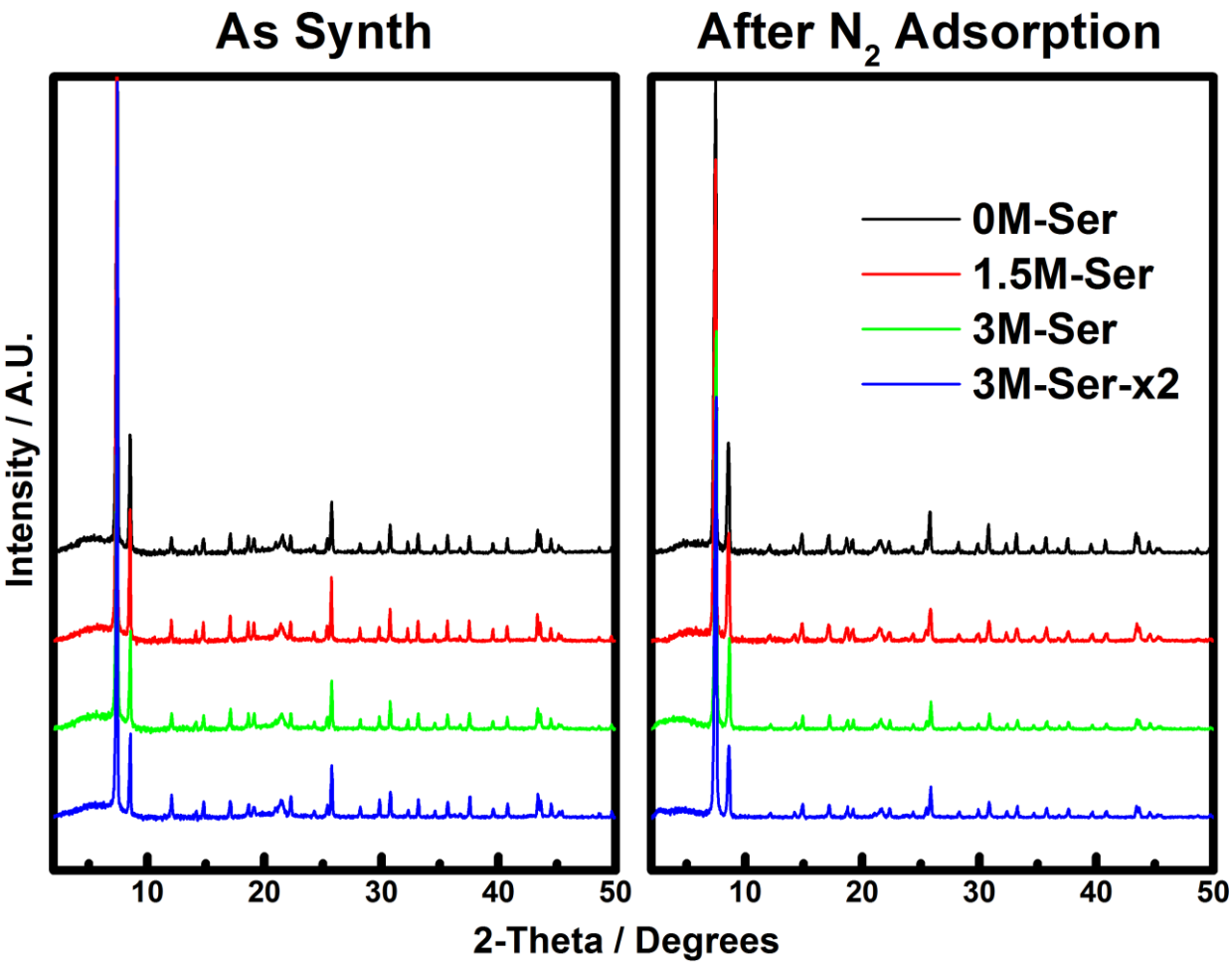

Figure S40. PXRD patterns obtained on the large scale PSE samples before (left plot) and after (right plot) nitrogen sorption measurements. This figure demonstrates that all 4 samples were completely intact after nitrogen sorption. See **Table S1** for details of the pretreatment methods used before the measurements.

5.2. Dissolution / ^{1}H NMR Before and After Nitrogen Sorption Measurements

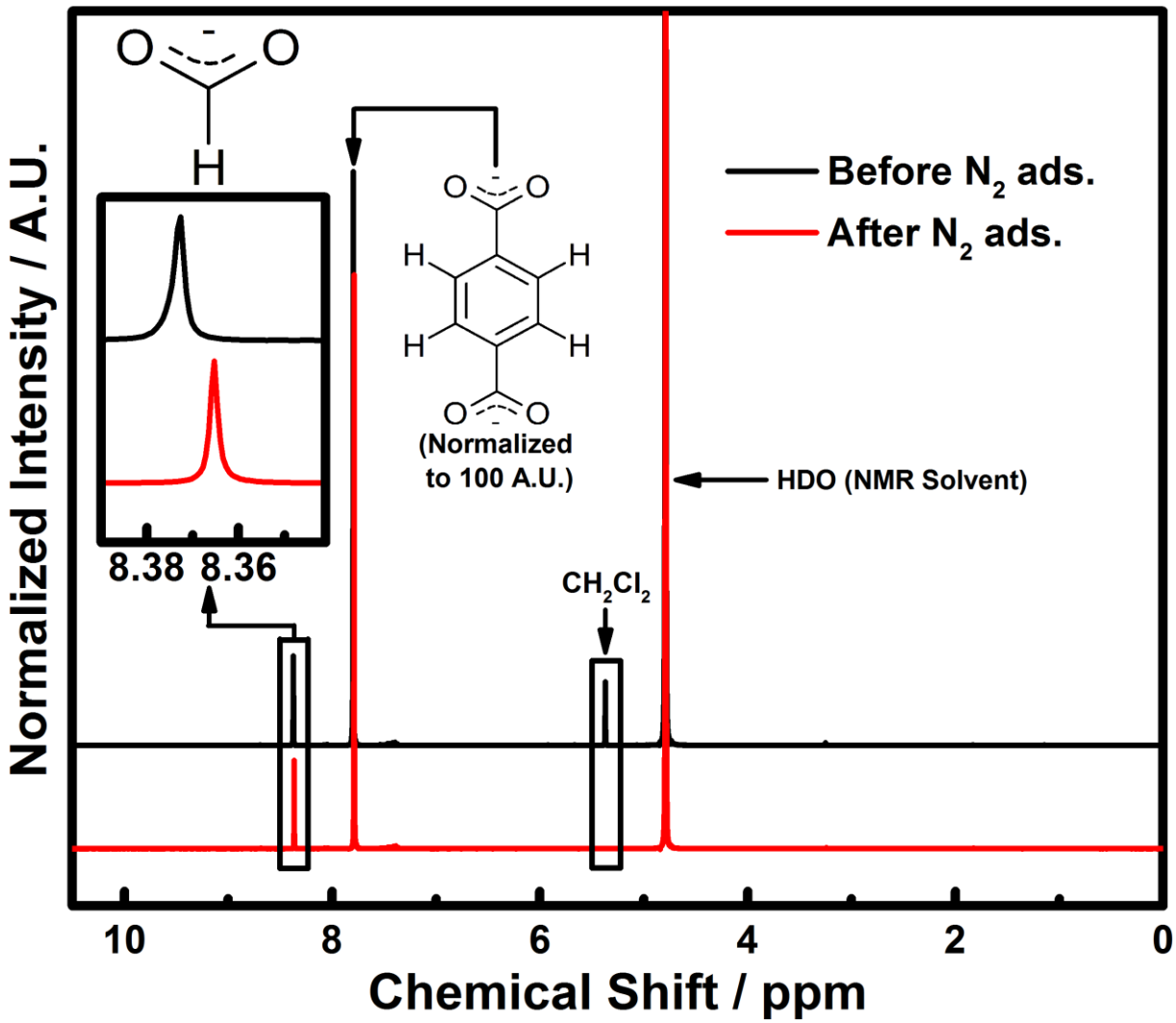

Figure S41. Dissolution/^{1}H NMR spectra obtained on 0M-Ser before and after nitrogen sorption measurements. This figure demonstrates that dichloromethane (CH_2Cl_2) was completely removed by the pretreatment (see **Table S1**) and that the formate content was unaffected.

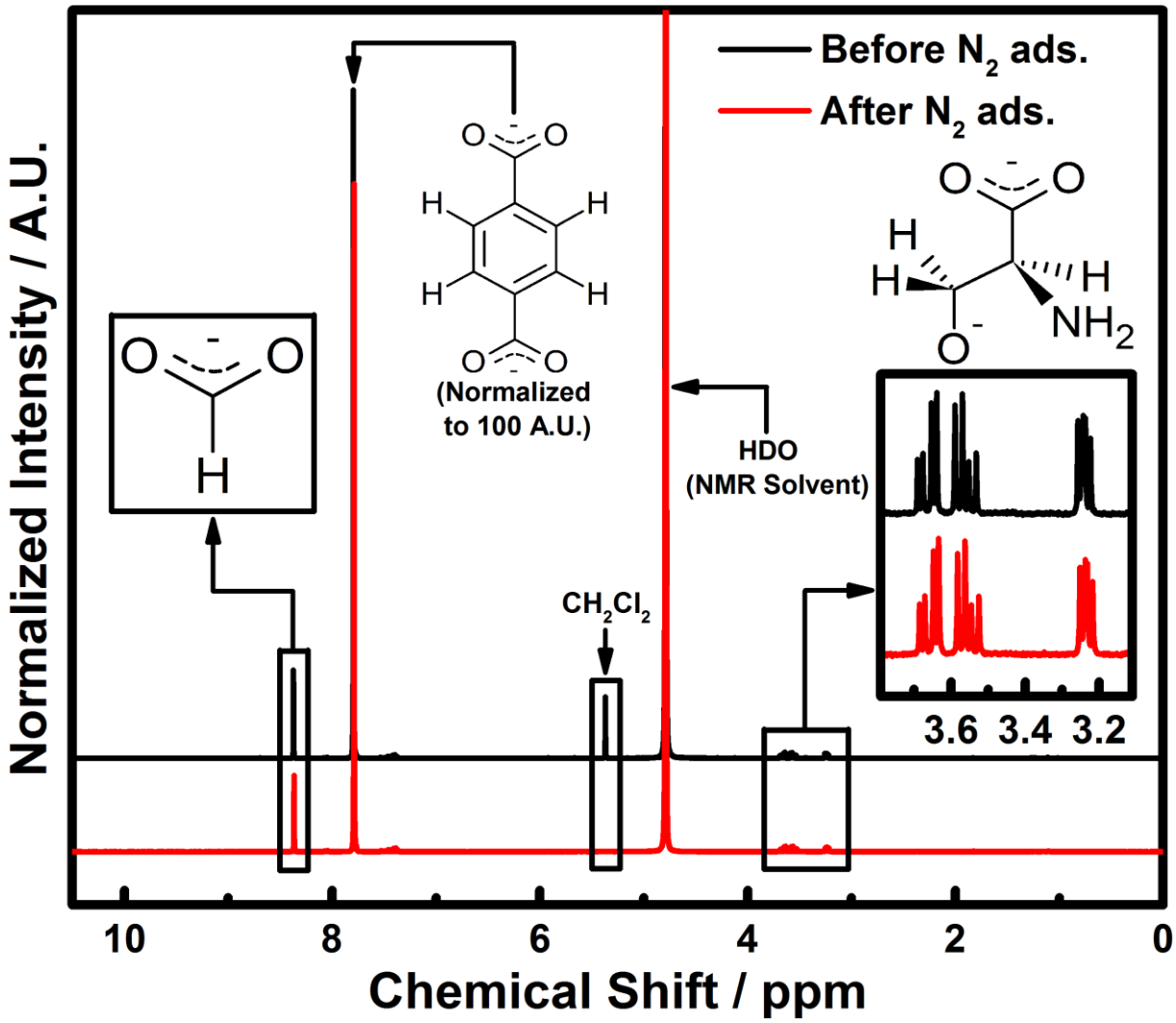

Figure S42. Dissolution/^{1}H NMR spectra obtained on 1.5M-Ser before and after nitrogen sorption measurements. This figure demonstrates that dichloromethane (CH_2Cl_2) was completely removed by the pretreatment (see **Table S1**) while the formate and L-Serine content was unaffected.

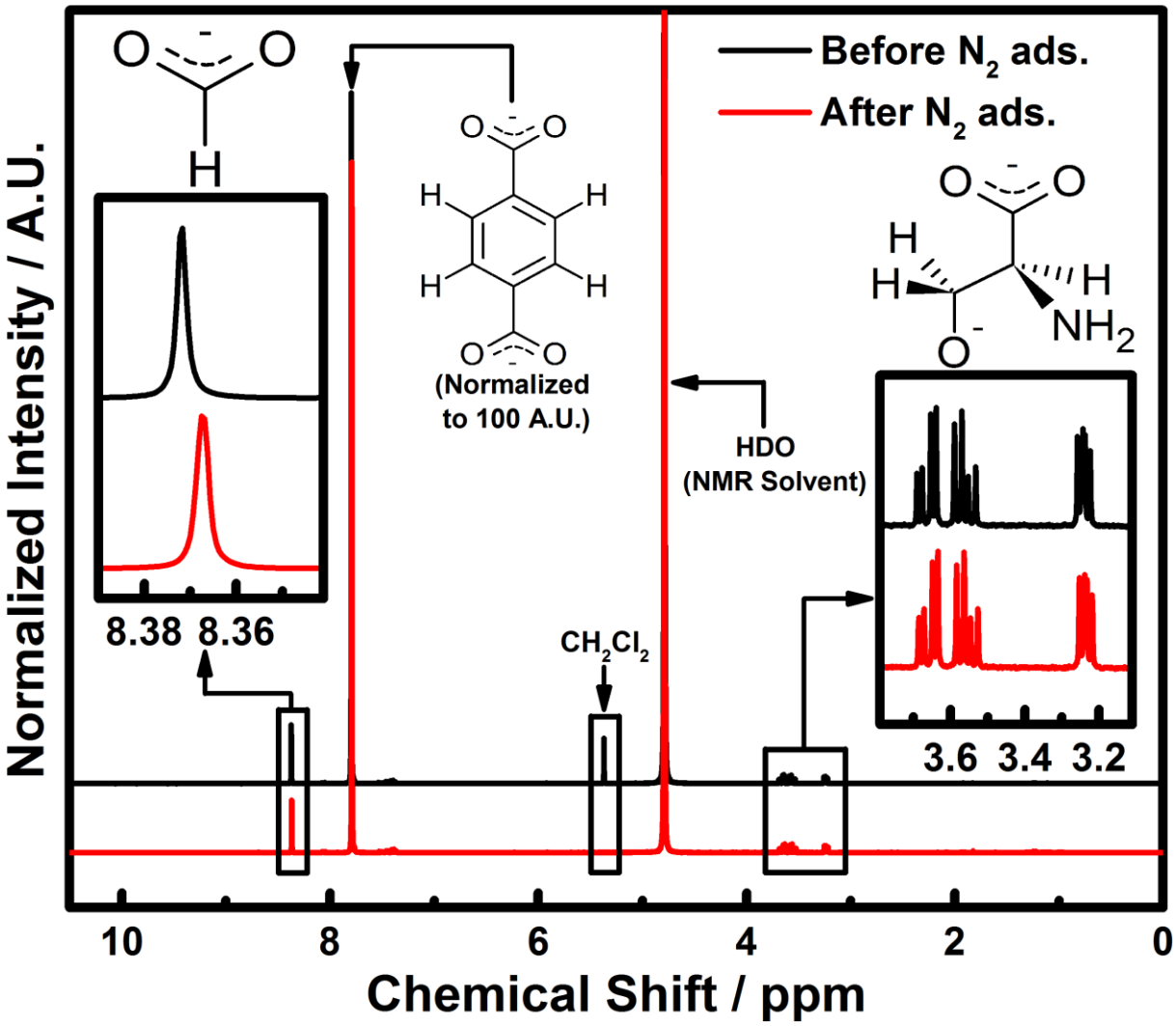

Figure S43. Dissolution/^{1}H NMR spectra obtained on 3M-Ser before and after nitrogen sorption measurements. This figure demonstrates that dichloromethane (CH_2Cl_2) was completely removed by the pretreatment (see **Table S1**) while the formate and L-Serine content was unaffected.

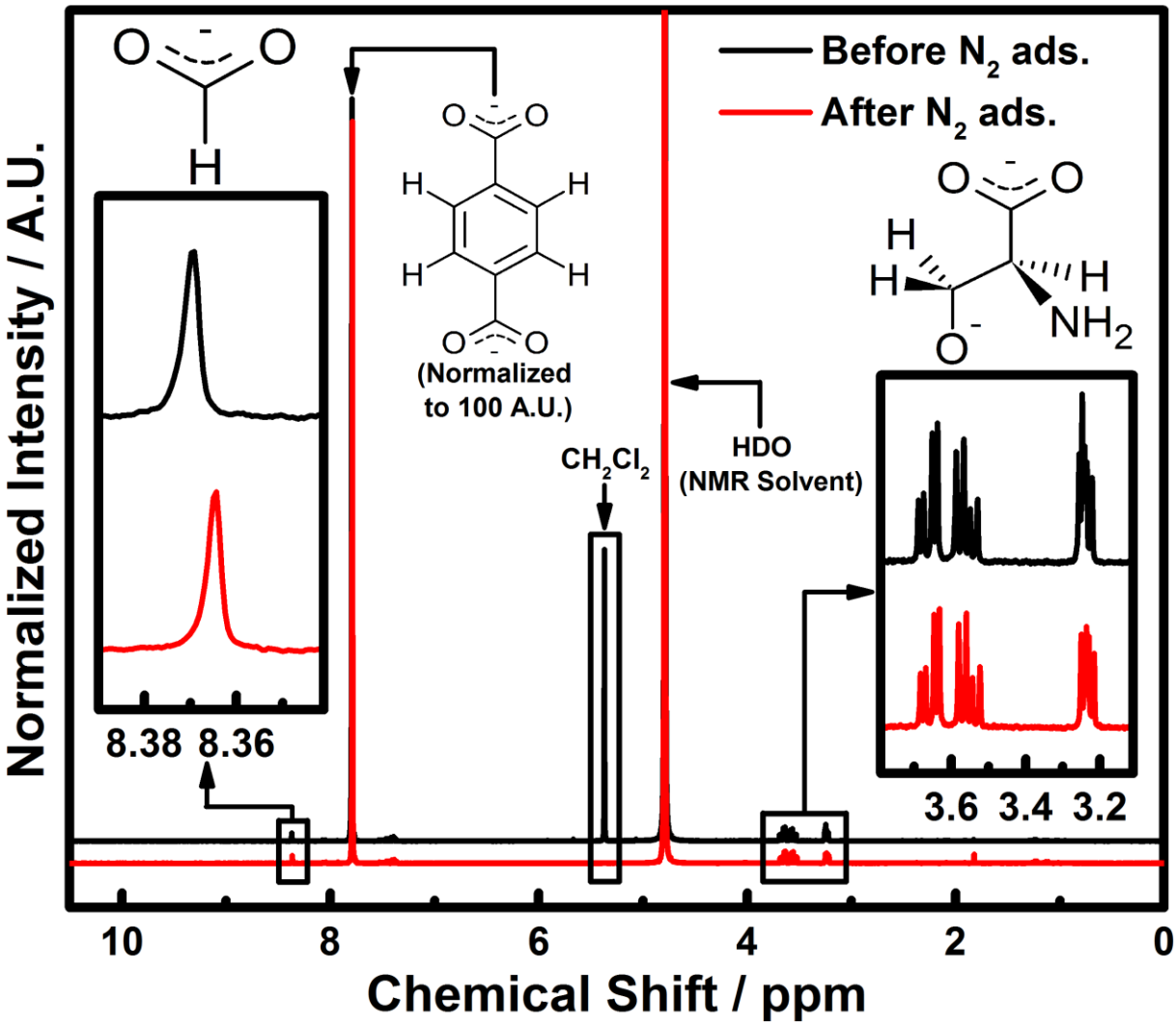

Figure S44. Dissolution/^{1}H NMR spectra obtained on 3M-Ser-x2 before and after nitrogen sorption measurements. This figure demonstrates that dichloromethane (CH_2Cl_2) was completely removed by the pretreatment (see **Table S1**) while the formate and L-Serine content was unaffected.

6. References

(1) Pullen, S.; Fei, H.; Orthaber, A.; Cohen, S. M.; Ott, S., Enhanced Photochemical Hydrogen Production by a Molecular Diiron Catalyst Incorporated into a Metal-Organic Framework. *J. Am. Chem. Soc.* **2013,** 135, 16997-17003.

(2) Mondloch, J. E.; Bury, W.; Fairen-Jimenez, D.; Kwon, S.; DeMarco, E. J.; Weston, M. H.; Sarjeant, A. A.; Nguyen, S. T.; Stair, P. C.; Snurr, R. Q.; Farha, O. K.; Hupp, J. T., Vapor-Phase Metalation by Atomic Layer Deposition in a Metal-Organic Framework. *J. Am. Chem. Soc.* **2013,** 135, 10294-10297.

(3) Shearer, G. C.; Chavan, S.; Bordiga, S.; Svelle, S.; Olsbye, U.; Lillerud, K. P., Defect Engineering: Tuning the Porosity and Composition of the Metal–Organic Framework UiO-66 via Modulated Synthesis. *Chem. Mater.* **2016,** 28, 3749-3761.

(4) Barcia, P. S.; Guimaraes, D.; Mendes, P. A. P.; Silva, J. A. C.; Guillerm, V.; Chevreau, H.; Serre, C.; Rodrigues, A. E., Reverse shape selectivity in the adsorption of hexane and xylene isomers in MOF UiO-66. *Micropor. Mesopor. Mat.* **2011,** 139, 67-73.

(5) Shearer, G. C.; Chavan, S.; Ethiraj, J.; Vitillo, J. G.; Svelle, S.; Olsbye, U.; Lamberti, C.; Bordiga, S.; Lillerud, K. P., Tuned to Perfection: Ironing Out the Defects in Metal-Organic Framework UiO-66. *Chemistry of Materials* **2014,** 26, 4068-4071.

(6) Mondloch, J. E.; Katz, M. J.; Planas, N.; Semrouni, D.; Gagliardi, L.; Hupp, J. T.; Farha, O. K., Are Zr-6-based MOFs water stable? Linker hydrolysis vs. capillary-force-driven channel collapse. *Chem. Commun.* **2014,** 50, 8944-8946.

(7) Rouquerol, J.; Llewellyn, P.; Rouquerol, F., Is the BET equation applicable to microporous adsorbents? *Stud. Surf. Sci. Catal.* **2006,** 160, 49-56.

(8) Dueren, T.; Millange, F.; Ferey, G.; Walton, K. S.; Snurr, R. Q., Calculating geometric surface areas as a characterization tool for metal-organic frameworks. *J. Phy. Chem. C.* **2007,** 111, 15350-15356.

(9) Senkovska, I.; Kaskel, S., Ultrahigh porosity in mesoporous MOFs: promises and limitations. *Chem. Commun.* **2014,** 50, 7089-7098.

(10) Wang, T. C.; Bury, W.; Gomez-Gualdron, D. A.; Vermeulen, N. A.; Mondloch, J. E.; Deria, P.; Zhang, K.; Moghadam, P. Z.; Sarjeant, A. A.; Snurr, R. Q.; Stoddart, J. F.; Hupp, J. T.; Farha, O. K., Ultrahigh Surface Area Zirconium MOFs and Insights into the Applicability of the BET Theory. *J. Am. Chem. Soc.* **2015,** 137, 3585-3591.

(11) Valenzano, L.; Civalleri, B.; Chavan, S.; Bordiga, S.; Nilsen, M. H.; Jakobsen, S.; Lillerud, K. P.; Lamberti, C., Disclosing the Complex Structure of UiO-66 Metal Organic Framework: A Synergic Combination of Experiment and Theory. *Chem. Mater.* **2011,** 23, 1700-1718.

(12) Wiersum, A. D.; Soubeyrand-Lenoir, E.; Yang, Q. Y.; Moulin, B.; Guillerm, V.; Ben Yahia, M.; Bourrelly, S.; Vimont, A.; Miller, S.; Vagner, C.; Daturi, M.; Clet, G.; Serre, C.; Maurin, G.; Llewellyn, P. L., An Evaluation of UiO-66 for Gas-Based Applications. *Chem.-Asian J.* **2011,** 6, 3270-3280.

(13) Shearer, G. C.; Forselv, S.; Chavan, S.; Bordiga, S.; Mathisen, K.; Bjorgen, M.; Svelle, S.; Lillerud, K. P., In Situ Infrared Spectroscopic and Gravimetric Characterisation of the Solvent Removal and Dehydroxylation of the Metal Organic Frameworks UiO-66 and UiO-67. *Top. Catal.* **2013,** 56, 770-782.

(14) Cliffe, M.; Hill, J.; Murray, C.; Coudert, F.; Goodwin, A., Defect-dependent colossal negative thermal expansion in UiO-66(Hf) metal-organic framework. *Phys. Chem. Chem. Phys.* **2015,** 17, 11586-11592.

(15) Vermoortele, F.; Bueken, B.; Le Bars, G.; Van de Voorde, B.; Vandichel, M.; Houthoofd, K.; Vimont, A.; Daturi, M.; Waroquier, M.; Van Speybroeck, V.; Kirschhock, C.; De Vos, D., Synthesis Modulation as a Tool To Increase the Catalytic Activity of Metal-Organic Frameworks: The Unique Case of UiO-66(Zr). *J. Am. Chem. Soc.* **2013,** 135, 11465-11468.

(16) Cavka, J.; Jakobsen, S.; Olsbye, U.; Guillou, N.; Lamberti, C.; Bordiga, S.; Lillerud, K., A new zirconium inorganic building brick forming metal organic frameworks with exceptional stability. *J. Am. Chem. Soc.* **2008,** 130, 13850-13851.

(17) Han, Y.; Liu, M.; Li, K.; Zuo, Y.; Wei, Y.; Xu, S.; Zhang, G.; Song, C.; Zhang, Z.; Guo, X., Facile synthesis of morphology and size-controlled zirconium metal-organic framework UiO-66: the role of hydrofluoric acid in crystallization. *Crystengcomm* **2015,** 17, 6434-6440.

(18) Myers, A.; Prausnitz, J., Thermodynamics of Mixed-Gas Adsorption. *Aiche J.* **1965,** 11, 121-+.

(19) Simon, C. M.; Smit, B.; Haranczyk, M., pyIAST: Ideal adsorbed solution theory (IAST) Python package. *Comput. Phys. Commun.* **2016,** 200, 364-380.

(20) Sumida, K.; Rogow, D. L.; Mason, J. A.; McDonald, T. M.; Bloch, E. D.; Herm, Z. R.; Bae, T.-H.; Long, J. R., Carbon Dioxide Capture in Metal–Organic Frameworks. *Chem. Rev.* **2012,** 112, 724-781.

(21) Wang, K.; Li, C.; Liang, Y.; Han, T.; Huang, H.; Yang, Q.; Liu, D.; Zhong, C., Rational construction of defects in a metal-organic framework for highly efficient adsorption and separation of dyes. *Chem. Eng. J.* **2016,** 289, 486-493.

(22) Ethiraj, J.; Albanese, E.; Civalleri, B.; Vitillo, J.; Bonino, F.; Chavan, S.; Shearer, G.; Lillerud, K.; Bordiga, S., Carbon Dioxide Adsorption in Amine-Functionalized Mixed-Ligand Metal-Organic Frameworks of UiO-66 Topology. *Chemsuschem* **2014,** 7, 3382-3388.